Effect of Micro-gravity on the Microstructural Evolution during Liquid Phase Sintering

A Dissertation
Presented to
The Academic Faculty

by

Asim Tewari

In Partial Fulfillment
of the Requirements for the Degree
Doctor of Philosophy

School of Materials Science and Engineering
Georgia Institute of Technology
February, 1999

Effect of Microgravity on the Microstructural Evolution during Liquid Phase Sintering

Approved:

Dr. Arun M. Gokhale, Chairman

Dr. Joe K. Cochran

Dr. Robert T. DeHoff

Dr. Meilin Liu

Dr. Michael D. Sacks

02/19/99
Date approved by Chairman

ACKNOWLEDGEMENTS

I would like to express my gratitude to my thesis advisor, Dr. Arun Gokhale, for his constant guidance and assistance in the completion of my doctoral work.

The funding for this research was provided by the Microgravity Science Applications Division of NASA (grant no. NAG-1245). This funding and the project monitor, Dr. Marcus Vlasse are gratefully acknowledged. I am also grateful to Dr. German of Pennsylvania State University for providing the LPS alloy specimen for my experimental work. I would also like to thank my thesis committee members, Dr. J. Cochran, Dr. R. DeHoff, Dr. M. Liu and Dr. M. Sacks. Their time and effort in the reading of my thesis and their suggestions on its improvement are appreciated.

I also want to thank my colleagues in Materials Sc. & Engg. Tom, Manish & Yang for help during my stay. I am also grateful to my parents and sister, Minaxi and brother, Anurag for their encouragement. I would like to express my gratitude to Deepa for her support and help in writing the thesis.

CONTENT

LIST OF TABLES

LIST OF FIGURES

SUMMARY

The effect of gravity on the evolution of microstructure during liquid phase sintering was studied using Ni-Fe tungsten heavy alloy, for varying sintering times, compositions, and gravity conditions (microgravity and normal gravity). A serial sectioning of the samples was carried out and the three dimensional microstructure was reconstructed. The microstructure was quantified using volume-probe techniques developed in the course of this research. Computer codes were written to extract descriptors of spatial arrangement of grains from the image data.

It was seen that the microstructure in gravity evolves as just a scale factor change with sintering time whereas it is not so in microgravity. The scale factor change in gravity was seen in the evolution of grain size distribution function, radial distribution function and 1^{st}, 2^{nd} and 3^{rd} nearest neighbor distribution functions. In specimens processed in both gravity and microgravity environment there are practically no isolated grains suspended in the matrix. This was expected in gravity where the grains have to contact each other to provide normal force to balance gravity, but it wassurprising to see this in microgravity. At a given sintering time, the coordination number in microgravity was significantly lower than that in gravity. In microgravity, the coordination number remains constant whereas in gravity, it increases with time. This increase is attributed to grain shape accommodation. A strong

correlation was found between the coordination number and the mean surface area of grains forming that coordination which was expressed by a linear equation. Inspite of significant differences between the volume fractions of gravity and microgravity samples, the 1st and 2nd 3D nearest neighbor distances are only a scale change, with the scale factor being the mean grain size.

In the initial stages of sintering, the kinetics of grain growth is slower in microgravity than in gravity environment resulting in a significant difference in the grain sizes. However, the difference in grain size after 120 minutes of sintering becomes insignificant. The observed difference in rates of grain growth at lower times (upto 1 minute) is attributed to the effect of coalescence. It was observed that there is no densification with time in microgravity though this effect is seen in gravity.

CHAPTER I

INTRODUCTION

Sintering is a phenomenon by virtue of which packed powders bond together when heated to temperatures in excess of approximately half the absolute melting temperature. Liquid phase sintering (LPS) is a subclass of the sintering processes involving particulate solid along with a coexisting liquid during some part of the thermal cycle. Presence of liquid during sintering gives this process an advantage over other sintering processes. The presence of liquid phase leads to rapid consolidation and sintering[1-3]. The capillary attraction due to wetting liquid gives rapid compact densification without the need of an external force. As the starting material is in a powder form, a near net shape fabrication is possible, and complete melting is not necessary. All these features make LPS a very attractive fabrication process for commercial production. Liquid phase sintering is a widely used fabrication process for high performance metallic and ceramic (glass-ceramic) materials. It is particularly useful for high melting point materials for which fabrication by melting is not feasible.

During liquid phase sintering there are at least three phases coexisting; vapor, liquid and solid; and these are associated with their specific interfaces and energies. Presence of three phases coupled with solubility, viscosity and diffusivity factors make the analytical treatment of the process very difficult. An important parameter in the LPS process is gravity. Gravity induces separation of the solid and liquid phases due to the density differences

between the two[4-7]. Consequently, the microstructure evolves differently in gravity than the way it would in its absence. This difference in microstructure affects the sintering kinetics. Therefore, to better understand the process of LPS it is of interest to quantify and understand the effect of gravity on microstructural evolution during LPS. For this purpose, it is necessary to perform LPS experiments in absence of gravity (i.e. micro-gravity environment as of a space station) and compare the results to those of experiments done under normal gravity. Such experiments were recently conducted by Professor R.M. German's group at Pennsylvania State University[8], under a NASA supported research program (some micro-gravity experiments were also done by other researchers in the past[9-13]). The focus of the present research is to uncouple the effect of gravity during LPS so as to better understand the process of LPS.

The main objective of this research is to understand the effect of gravity on the fundamental process of LPS. This is of both fundamental and practical interest in Materials Engineering. The biggest hurdle in these type of studies is the inability to quantify the true 3D microstructure. The reason for this is the fact that the observations under a microscope are 2D sections of the real 3D microstructure. Thus to achieve our main objective it is necessary to quantify the true 3D microstructure (this can be done using stereology and 3D microstructure reconstruction through serial sectioning). Hence true 3D microstructure quantification becomes another objective of this research.

The next chapter outlines the fundamentals of LPS and microstructural evolution during the process. This is followed by a description of the Digital Image Analysis

procedures and computer calculations to extract quantitative information about the microstructure. The experimental work is then presented in the subsequent chapter, followed by the chapter on results and discussions. Finally the conclusions drawn from this research are presented in chapter five.

CHAPTER II

BACKGROUND

The objective of the research was to study the effect of gravity on fundamental processes of LPS. In order to accomplish this, knowledge of the principles of LPS, microstructure and stereology and digital image analysis is required. A brief background on these topics is presented in this chapter.

2.1 Background on LPS

Sintering is a phenomenon in which powder, when subjected to high temperatures (of approx. half the absolute melting point), agglomerates . The phenomenon of sintering occurs due to formation of inter-particle bonds by atomic diffusion at the sintering temperature. If there is a coexisting liquid present along with solid particles during some part of the sintering, then the phenomenon is known as liquid phase sintering (LPS). Presence of liquid during sintering usually enhances the sintering kinetics which is advantageous. Liquid aids rearrangement of grains by reducing inter-particle friction, helps compact densification by capillary attraction, and increases mass transport due to faster diffusion through liquid.

A typical powder compact for an LPS system has two constituents. The major constituent is a powder of a high melting point material which remains solid throughout the sintering, while the minor constituent is a powder of a low melting point material which forms liquid during sintering. The steps involved in the process of LPS are as follows:

1. Mixing of elemental (or pre-alloyed) powders in appropriate amounts.
2. Blending of the powder mixture.
3. Tapping of the powder in a mold.
4. Cold compaction of the mold.
5. Pre-sintering of the green compact.
6. Machining of the pre-sintered compact to proper specifications.
7. Liquid phase sintering of the final compact at desired temperature for a specified amount of time.

The resulting microstructure is described in detail in the following sub-section.

2.2 Characteristics of LPS Microstructure

A typical LPS microstructure consists of matrix, grains and porosity as in Figure 2.1 (some times the amount of porosity is negligible). Grains are of the high melting point material and they are in solid state during sintering, whereas the matrix is of the low melting point material which is present in the form of liquid during LPS. The main features seen in LPS microstructure are grains, their inter-particle contacts and liquid rich regions known as liquid pockets (Figure 2.5). A brief description of the geometry of inter-particle contacts and

liquid pockets is given below.

2.2.1 Inter-particle contacts

At high volume fraction of solid, most of the grains are connected to one another by inter-particle contacts (see Figure 2.1). Each inter-particle contact contains a triple line of contact between the two associated grains and liquid. Three characteristic dihedral angles exist at this triple line, which are governed by the interfacial energies. The triple line (or neck) is seen as a triple point in a 2D metallographic section. Dihedral is the angle between outward normals of any two surfaces where they meet to form an edge. Therefore, three dihedral angles exist at a triple line representing junction of three interfaces. The values of equilibrium dihedral angles are related to the interfacial energies of the three associated interfaces as follows.

$$\frac{\gamma_{12}}{\sin\phi_3} = \frac{\gamma_{23}}{\sin\phi_1} = \frac{\gamma_{13}}{\sin\phi_2} \qquad 2.1$$

where, γs are interfacial energies and ϕs are angles as shown in the Figure 2.3a. If the solid liquid interfacial energy is not a function of crystallographic orientation (resulting in two of the interfacial energies used in equation 2.1 being the same), then dihedral angle between two abutting grains can be expressed as follows (see Figure 2.3b),

$$\phi = 2 \arccos\left(\frac{\gamma_{SS}}{2\gamma_{SL}}\right) \qquad 2.2$$

If the equilibrium dihedral angles are maintained at the neck, then the geometry of the neck is locally constrained, resulting in a curved intergranular grain boundary, if the two abutting grains have different sizes (see Figure 2.4). The radius of curvature of the neck can be expressed as follows:

$$r = 2 \cos\left(\frac{\phi}{2}\right) \frac{R_1 R_2}{R_1 - R_2} \qquad 2.3$$

The dihedral angle controls the shape of the liquid at the triple line, and the shape of the grains. It also affects the coordination number (number of contacts formed by a grain with its neighbors), size of stable pores and the rate and mechanism of LPS (as will be discussed later in this chapter).

2.2.2 Liquid pockets and porosity

It is common to see large regions of liquid with no grains (Figure 2.5) known as liquid pockets. These are initially voids formed at the regions where low melting constituent powder particles are present in the initial powder mass. These voids get filled with liquid during the pore-filling stage of the LPS process. The mechanism of liquid pocket formation is discussed later in this chapter. If these voids do not get filled with liquid during LPS, it results in porosity. The process of pore formation is described in greater detail in a later section.

2.3 Different Stages of LPS

The main event, prior to liquid formation, is solid state sintering[3]. The processes after liquid formation can be broken into three overlapping stages. The first stage is characterized by melt formation and rearrangement of solid particles due to the capillary force of the liquid. In the intermediate stage solution-reprecipitation and shape accommodation takes place. The final stage is characterized by grain growth and coarsening. A brief account of processes taking place in each stage is given below.

2.3.1 Initial Stage Processes

The initial stage corresponds to processes which take place right after heating and upto several minutes (depending on the system) after liquid formation. This stage involves three processes, namely: melt formation, particle rearrangement, and pore and contact formation.

Melt formation

On melt formation, liquid flows between the particles, penetrates the grain boundaries, dissolves particle irregularities, and eventually helps form new grain contacts. It takes some time for the liquid to attain chemical equilibrium with the solid particles. The dimensional changes during this time are affected by the diffusivity ratio of the high melting point constituent (in low melting point constituent) and the low melting point constituent (in high melting point constituent). An unequal diffusivity ratio leads to swelling[14]. After sufficient time, equilibrium effects dominate and the effect of ratio of diffusivity is taken over by the ratio of solubility of the high melting point constituent (in low melting point

constituent) and low melting point constituent (in high melting point constituent). A high solubility of high melting point constituent in the low melting point constituent provides better densification due to surface smoothing, sliding and better lubrication[15], whereas low melting point constituents with high solubility in the high melting point constituent will dissolve during heating, leaving a pore at the prior low melting point constituent site[16]. This is shown schematically in Figure 2.6 and some examples are presented in Table 2.1.

The wetting characteristic of the solid by the liquid is the most important property which affects the initial stage after melt formation. The capillary forces exerted by the wetting liquid cause particle rearrangement, to which the compact responds as a viscous solid. The melt flows in the pores due to capillary force, this is known as penetration. In cases where the solid particles are polycrystalline this penetration continues at the grain boundaries and causes fragmentation of the grains[17]. The driving force responsible for liquid penetration at the grain boundaries (fragmentation) originate from the unbalanced surface forces at the solid-solid-liquid interface. For dihedral angles over 60 deg, fragmentation is extremely unlikely[18], whereas penetration can fully disintegrate the solid grains if the dihedral angle is 0 deg.

Rearrangement

Rearrangement of particles is a two stage process, primary and secondary. During the primary rearrangement, the solid particles around the melting low melting point constituent get rearranged. This can some times result in clustering of these particles around low melting point constituent rich regions. Secondary rearrangement is the term given to the processes

which deal with the rearrangement of clusters formed in the primary rearrangement or of fragmented grains.

The rearrangement occurs due to the contact force caused by the wetting liquid. The contact force depends on the contact angle (which is equal to (π - dihedral angle)), particle size, and amount of liquid, and it can produce a pressure as high as 100 atmospheres. For spherical particles, the contact force decreases with increasing amount of liquid. On the contrary, an inverse relation holds for irregularly shaped particles[19]. In general for any particle shape intermediate amount of liquid is good for rearrangement, and small particle size and low contact angle are always beneficial.

Another factor which influences rearrangement is green density. As the green density increases, there is greater mechanical locking, higher interparticle friction and less vapor phase. All of these result in reduced rearrangement of the particles. In general, increase in green density reduces rearrangement rates[3]. However, there are some cases in which increased green density has resulted in higher final density due to low initial porosity[3].

Pore and contact formation

If the liquid wets the solid then on melt formation it flows and forms a liquid film around the neighboring solid particles, leaving behind a pore at the prior additive site[16] (Figure 2.6). These pores can be distinctly seen if the particle size of additive was large. At times pore formation is also seen as a result of rearrangement. This happens due to unbalanced torque produced during rearrangement between neighboring particles [19].

Another consequence of rearrangement is contact formation. As the compact shrinks due to rearrangement, new contacts are formed between particles. These contacts bond the particles together to give rigidity to the compact. Once a rigid skeleton is formed, the process of rearrangement ceases for all practical purposes. This marks the end of initial stage processes and the beginning of intermediate stage liquid phase sintering.

2.3.2 Intermediate stage processes

During this second stage of LPS, movement and rearrangement of particles stops and solution-reprecipitation starts. One of the basic requirements for solution-reprecipitation is solid solubility in liquid. Solution-reprecipitation results in densification and coarsening of the microstructure. This process is driven by reduction of interfacial area which results in deviation of particles from a spherical shape (grain shape accommodation), contact flattening, dissolution of fine grains, inter-particle neck growth, coalescence and pore filling. These effects are discussed in detail below.

Grain shape accommodation

The driving force for densification comes from surface energy associated with pores. If there is not sufficient amount of liquid to fill the pores, the grains deviate from a spherical shape to provide more efficient packing to release liquid to fill the pores. In spite of their deviation from spherical shape there is a net decrease in the energy of the system due to elimination of pores[20]. This phenomenon of shape change of the grains is known as Grain Shape Accommodation. Neck growth takes place along with grain shape accommodation.

There are three transport mechanisms responsible for grain shape accommodation.

The first one is known as contact flattening. In this the stress due to wetting liquid causes preferential dissolution of solid at grain contacts with reprecipitation at regions away from the contact [21] (Figure 2.7 a). The second mechanism involves growth of large grains by dissolution of small surrounding grains[22] (Figure 2.7b). The large grain so grows that it undergoes shape accommodation. In the third mechanism the interparticle neck grows by solid diffusion along the solid-solid grain-boundary (Figure 2.7c). This third mechanism is very slow except for systems with no solid solubility in liquid (e.g. W-Cu). The major differences between the three mechanisms are shown in Table 2.2.

Contact Flattening

The rate of contact flattening can depend on either of two steps; dissolution or diffusion. A measure for contact flattening is the center-to center approach distance, which can be related to the shrinkage $\Delta L/L_0$. The diffusion controlled shrinkage for two equal sized spheres, in presence of a thin layer of intergranular liquid[21], can be expressed as follows:

$$(\Delta L/L_0)^n = \frac{12\delta\Omega\gamma DCt}{R^4 kT} \qquad 2.4$$

where, δ is the thickness of intergranular liquid, Ω is the atomic volume, γ is the liquid-vapor surface energy, D is the diffusivity of the solid in the liquid, C is the solid concentration in the liquid, t is the isothermal time, k is Boltzmann's constant, T is the absolute temperature and n is an exponent equal to 3. The assumption of presence of intergranular liquid basically assumes zero dihedral angle, which is not always true. Thus the above solution was corrected

for the dihedral contribution[23,24]. The corrected equation was numerically solved and was found to be of the same type as the above equation except for the value of exponent n, which in this case varied from 3.00 to 3.15.

For reaction controlled contact flattening the rate of shrinkage can be predicted as follows:

$$(\Delta L/L_0)^2 = \frac{4k_r \Omega \gamma C t}{R^2 kT} \qquad 2.5$$

where k_r is reaction constant.

Dissolution of fine grains

The mechanism of dissolution of fine grains does not necessarily involve center-to-center approach. The rate of shrinkage in this case can be defined as a ratio r/(R+r) for a three grain model as shown in Figure 2.7b. An approximate equation for shrinkage[25] for the three grain geometry can be expressed as follows

$$(\Delta L/L_0)^3 = \frac{6\Omega \gamma D C t}{R^3 kT} \qquad 2.6$$

The third mechanism of shape accommodation is neck growth by solid-state diffusion. The process is similar to contact flattening for non zero dihedral angle[21] except for diffusion in solid. The equation 2.4 also gives the shrinkage for this case where exponent n is from 3.00 to 3.15 and D represents the diffusivity of the solid in solid.

Interparticle neck growth

In the intermediate stage the neck formed in the initial stage grows to reach a final stable neck size dictated by the dihedral angle and grain size. If there is no grain shape accommodation, the final neck size can be related to grain radius and dihedral angle as follows:

$$X = R \sin (\phi / 2) \qquad 2.7$$

where X is the equilibrium neck size, R is the grain radius and ϕ is the dihedral angle.

Once this stable neck size ratio is reached the further neck growth is dependent on grain growth[26]. The independent neck growth, to attain this stable neck size, takes place by several mechanisms involving solution reprecipitation, solid-state diffusion and coalescence. A general solution to the problem of neck growth [23,24] yield the following type of relation:

$$(X/R)^n = k\, t \qquad 2.8$$

where, t is time and k is a term of the type $D/(K\, T\, R^m)$. The value of n is from 5 to 7 and that of m is 3 or 4. These analyses show that the volume fraction of liquid and contact angle have very little effect on the neck growth kinetics.

Coalescence

Coalescence is a process in which two contacting grains of dissimilar size merge into one by directional grain growth of one. The process results in increase in grain size and decrease in number density. The driving force for the process is a finite radius of curvature of the solid-solid grain boundary as given by equation 2.3 and shown in Figure 2.4. The curved grain boundary is unstable and diffusion across it results in a more stable structure. Thus coalescence is favored by high dihedral angle and large grain size difference. In general coalescence is always favored by higher solid volume fraction.

The process of coalescence can take place by the following three possible mechanisms: Grain boundary migration, liquid film migration or solution reprecipitation. The mechanism of grain boundary migration requires that the contacting grains have a low angle grain boundary. The probability of having a low angle grain boundary is less than 0.01[26], thus grain boundary migration does not contribute much to the process of coalescence. The mechanism of liquid film migration refers to the grain boundary migration by diffusion through a thin liquid film. This mechanism has been only seen in WHAs.

Pore Filling

In general the pores can be classified into three types based on their origin. The first one is due to initial porosity in the green compact, the second type of pores are formed due to particle rearrangement in the initial stage and the last one are formed at prior additive sites on melt formation. The first two type of pores are small and get filled by grain shape accommodation, whereas the third type of pores are often big and thus remain for a

considerable amount of time. They eventually get filled by liquid penetration. This happens when the radius of liquid meniscus increases to a value that the capillary force causes the liquid to penetrate the pore[27]. The radius of liquid meniscus is given by the following equation:

$$r_m = R\,(1-\cos\alpha) / \cos\alpha \qquad 2.9$$

where R is the grain radius. Thus the size of stable pore radius is inversely proportional to the grain radius.

2.3.3 Third Stage

The main event in the last stage of sintering is coarsening. By then all the solid particles are a part of one solid rigid skeleton. The process of densification is still on and takes place by grain shape accommodation (which also contributes to coarsening). It is common to see 99% dense compacts in systems with insoluble gases (although density usually decreases with time after reaching a maximum). The driving force for events in this stage is reduction of liquid-solid interfacial energy.

In systems sintered under vacuum the porosity becomes almost zero,and thus the only change seen is in the grain size. Thus processes in this stage are often referred to as scale change although there may be more than just scale change.

Grain growth

The thermodynamic driving force for coarsening is reduction of interfacial energy by

decrease in both the amount and curvature of solid-liquid interface. This leads to Ostwald ripening, in which bigger grains grow at the expense of smaller grains. There is another mechanism by which grain size increases and that is by coalescence. The driving force for this is the curvature of the interparticle neck.

The kinetics of grain growth leads to a functionality of $(\text{time})^{1/n}$ for the mean grain size. The value of n in the exponent varies from 2 to 4 for most of the materials[28]. The two main ways in which grain growth is possible is via transport through liquid or by coalescence. For the case of transport through liquid, analytical grain growth models are available only for very low volume fraction of solid. A classical solution to diffusion controlled grain growth in an infinitely dilute solid fraction is as,

$$\overline{R^3} = \overline{R_0^3} + 4kt/9 \qquad 2.10$$

where R_o is the initial grain size, k is rate constant and t is time. To account for finite volume fraction of solids, computer simulations have been performed for multiparticle systems with varying volume fraction and size distribution[29,30,31], and surprisingly the grain growth exponent has been found to be very close to 3 in all cases(although it has been shown that some of the data fit equally well with exponents of 2 and 4 [50]). The only effect of volume fraction is seen in the rate constant k, which increases with volume fraction because the diffusional distances decreases.

In some multicomponent LPS systems it is possible that the interfacial reaction is the

slowest and thus the rate controlling step in the process of grain growth. For coarsening in such systems the predicted grain size versus time relation is as follows:

$$\overline{R^2} = \overline{R_0^2} + 64\ \gamma\ C\ \Omega\ k_r\ t/(81KT) \qquad 2.11$$

where k_r is reaction rate constant and the rest of the symbols have their usual meaning. Rate controlling step for coarsening for some common systems is given in Table 2.3.

If coalescence is an active mechanism in grain growth then it will increase the rate constant and will broaden the grain size distribution. But the overall effect of coalescence is not enough to change the grain growth exponent from 3. The contribution of coalescence is expected to increase with increasing volume fraction of solid.

Based on the three mechanisms for grain growth namely, diffusion controlled, reaction controlled and coalescence; it is possible to predict the grain size distribution at steady state as shown in Figure 2.8.

2.4 Theories of Liquid Phase Sintering

The process of LPS is a three stage process with rapid rearrangement in the first stage followed by solution re-precipitation in the second stage and coarsening in the third. The first stage is completed rapidly; the observed evolution of microstructure reflects the second and third stages. Both of these steps involve diffusion, caused by the well known curvature dependence of the chemical potential given by [32]:

$$\mu = \mu_o + V_m \gamma H \qquad 2.12$$

where μ is the chemical potential of an atom at solid-liquid interface, H is the local mean curvature of the interface, V_m is the molar volume, γ is the surface energy, and μ_o is the chemical potential of an atom with flat interface. It is evident from this equation that there will be a flow of atoms from regions of high curvature (i.e. higher chemical potential) to the regions of low curvature, resulting in an increase of the scale of the structure. This transport process is known as Ostwald ripening and was originally discovered in 1901 by W. Ostwald [33]. In spite of this qualitative explanation of the phenomenon, it was only in 1956 that Greenwood[34] attempted to construct a qualitative theory for the process. This was followed by an analysis by Kingery[21,35] of densification during liquid phase sintering. Since these theories had unrealistic solutions to the diffusion field, they did not meet with success, but still time dependence of a linear microstructure scale was predicted as a power of 1/3 (which happens to be true in the theories to follow).

The biggest milestone in the theory of Ostwald ripening was made by a paper in 1959 by Lifshitz and Slyozov (LS) [36] and another independent paper by Wagner [37](LSW) in 1961. The main advancement made in the theory by LSW was that they were able to treat an ensemble of coarsening particles (with a size distribution) and were able to predict long-time behaviour with analytical solutions of the relevant equations. Since then the theory of coarsening has advanced a lot with introduction of numerical solutions and

simulations, but still the paper of LSW is the seminal paper to which all subsequent work has been compared.

2.4.1 LSW theory for Ostwald ripening

Before we compare and analyze the different modern theories of ripening, a brief review of the LSW theory[36,37] is presented. The system analyzed by LSW was a two phase system, with the coarsening phase consisting of spherical particles fixed in space and the second phase being a continuous matrix. The basic equations of LSW theory are as follows.

Let the dimensionless length be $l = l^*/l_c$ where l_c is characteristic length give by $l_c = (R_g T)/(2\gamma V_m)$, and l^* is dimensional length R_g is gas constant and T is temperature. Dimensionless concentration θ in the matrix is defined by, $\theta = (c-c_\infty)/c_\infty$, where c is the solute concentrate in the matrix and c_∞ is the solute concentrate in the matrix at a flat interface. Dimensionless time is defined as $t = t^* (D c_\infty V_m / l_c^2)$ where t^* is dimensional time and D is diffusion coefficient of solute in the matrix.

Continuity equation

The coarsening particles are described by particle radius distribution function, $f(R,t)$, where $f(R,t)\,dR$ are the number of particles in the size range R to $R+dR$ at time t. The radius of particles is changing thus the flux of particles passing through a size value is $f \cdot \dot{R}$, where $\dot{R} \equiv dR/dt$. Therefor the accumulation of particles in a size range R to R+dR is given by:

$$\partial f / \partial t = J - \partial (f . \dot{R}) / \partial R \qquad 2.13$$

where J is the production in the size range. This production term can be due to nucleation or coalescence and was considered zero in the LSW theory, thus this theory does not account for coalescence.

Diffusion equation

The rate of change of radius of a size class of particles depends on the thermodynamics and kinetics of the system. LSW assumed that the spherical particles are growing or dissolving in a supersaturated matrix (with super-saturation equal to θ_m). In this case the thermodynamics is dictated by the curvature dependence of chemical potential and kinetics is dictated by the mechanism of diffusion transport. A small degree of supersaturation of the matrix was assumed and the dimensions of the particles were assumed to be small compared to the inter-particle distances. This leads to the justification of quasi-stationary approximation for the diffusion field, hence the governing equation is Laplace's equation , i.e.

$$\nabla^2 \theta = 0 \qquad 2.14$$

The boundary conditions of the Laplace's equation are

$$\theta(R) = 1/R, \text{ and} \qquad 2.15$$

$$\lim_{r\to\infty} \theta(r) = \theta_m \qquad 2.16$$

On applying these boundary conditions to the Laplace's equation and conserving the flux at the interface one can show that:

$$\dot{R} = (\theta_m - 1/R)/(R) \qquad 2.17$$

It can be seen from the above equation that the growth or dissolution of a particle in this analysis would depend on the mean field concentration set at infinity. Note that for $R = 1/\theta_m$, $\dot{R} = 0$, i.e those particles show zero growth, particles above this size grow and particles below this size dissolve. This radius is known as critical radius and is denoted by R_C.

Mass conservation equation

The third and the final equation in the LSW theory comes from the conservation of solute. The total solute in the system is divided between the matrix with concentration θ_m and particles of pure solute, this is expressed by

$$\theta_o = \theta_m + 4\pi f_3/(3V_m c_\infty), \qquad 2.18$$

where $f_n = \int_0^\infty R^n f(R,t)\, dR$.

Asymptotic solution as time goes to infinity

Equations 2.13, 2.14 and 2.18 can be rewritten in the form of nonlinear integro-differential equations. LSW found that these equations have an analytical asymptotic solution as $t \to \infty$, although transient solutions are analytically intractable. They showed that as $t \to \infty$, the following is true: $K(t) = 3R_c^2 \dot{R}_c \to$ constant, $R_c \to R$, and $4\pi f_3 \to \theta_0 3V_m c_\infty / (4\pi)$, where $R = f_1 / f_0$. Thus the solution to the continuity equation is of the type $g(R/R).\ h(t)$ which can be solved to get the particle size distribution $g(R/R)$. The mean particle radius follows the $t^{1/3}$ power law, i.e. $R(t) = (R(0)^3 + 4t/9)^{1/3}$. The particle size distribution from LSW is given in Figure 2.8.

2.4.2 Modern theories

Two major limitations of the LSW theory are, (i) it is a mean field approach, and (ii). it is applicable only as the volume fractions tends to zero. Numerous subsequent coarsening have attempted to remove these limitations. Ardell[39,40] was the first to propose a modified coarsening theory applicable at non-zero particle volume fractions. This was followed by more recent models proposed by Brailsford and Wynblatt (BW)[41]; Davies, Nash and Stevens (DNS)[42]; Jayant and Nash (JN) [43,44]; Voorhees and Glicksman (VG)[30,31], Marqusee and Ross (MR)[45], and Tokuyama and Kawasaki (TK)[46]. All of these approaches tried to incorporate statistically averaged diffusional interactions of a particle of a given size class by its surrounding, by incorporating a volume fraction term. Figure 2.9 shows some of the size distributions predicted by these models. All of these theories, in general, agree on the following:

1 Volume fraction does not change the $t^{1/3}$ power law, though it affects the amplitude.

2 The normalized size distribution reaches an asymptotic distribution as $t \to \infty$.

3 The time invariant size distribution broadens as the volume fraction increases and becomes more symmetric than the original prediction of LSW.

4 The variation in the rate constant is more at low volume fractions of solute and slows down as volume fraction increases.

The general disagreements in the predictions come in the functionality of rate constant on volume fraction and the range of applicability of different assumptions. Another difference comes in the assumptions which formulate the problems (e.g. at what volume fraction spatial correlations are significant). These theories, although being by far the most realistic models, are only able to qualitatively predict the process of coarsening: experimental data do not completely agree with any one theory.

Recently, a different approach has been taken by DeHoff[47] to the problem of coarsening. He has introduced a new concept known as communicating neighbors which accounts for the neighboring grain interaction. By introduction of the concept of communicating neighbors he formulated a geometrically general model for liquid phase sintering. Using the principle of self-similarity of particle size distribution[48], DeHoff derived an expression for normalized particle size distribution. The scale of the microstructure still follows the $t^{1/3}$ power law, but the predictions of size distribution by his theory come out to be exactly the same as of the reaction controlled model by Wagner. Dehoff[49] has suggested that all the theories of coarsening can be put to a stringent test if

individual particle growth/shrinkage rates are calculated via growth path analysis.

2.5 LPS Research in Microgravity

The effect of microgravity on the process of LPS has been a point of curiosity for researchers for a very long time. LPS experiments in microgravity date back to the late 1980s (Ekbom[9-12]). These experiments were done on W-Ni-Fe system with very low volume fraction of tungsten(0.1 and 0.2). These experiments showed a reduction in grain agglomeration in microgravity. It also showed a larger mean grain size in microgravity than in gravity for small duration of sintering time; and a smaller mean grain size in microgravity at larger sintering times. These experiments did give some insight into the LPS process in microgravity, but raised many more questions than answers. The microgravity environment was produced on parabolic trajectory rockets thus the time for sintering was limited to 1 to 5 minutes.

An intensive study of LPS in microgravity was performed for the first time by German in association with NASA. This study was performed on WHA with variation in sintering times (upto120 minutes), weight content of tungsten and pre-sintering conditions. Preliminary results of these studies[8,50-53] suggested a small grain size difference in gravity and microgravity samples, processed for 120 minute. According to classical LSW theory the sintering rate should be decrease in microgravity due to lower solid volume fraction, which will increase diffusional distances. On the other hand it also predicts that the grain growth kinetics will be slower in gravity because of increase in solid grain contact

resulting in decrease of solid-liquid interface over which diffusion occurs. These are only qualitative descriptions and there are no comprehensive theories for LPS in microgravity. To explain the differences in the grain size seen in microgravity and gravity German et al.[50]proposed a model for LPS in microgravity. This model assumes that the differences in gravity and microgravity are due to combined affect of volume fraction difference and gravitational stresses. The driving force for coarsening is the differences in curvatures of solid particles which results in differences in solubility causing diffusional mass transport. The differences in solubility can also be caused by the stress state of the particles. This increase in solubility is very small but it was predicted that this will result in large grain size difference at long sintering times. The effect of stress can be expressed as a multiplicative factor to the rate constant K of equation 2.10 as follows:

$$K = K_0(1 + \frac{4D\rho gHD}{\gamma Vv}) \qquad 2.19$$

where K_0 is the rate constant in absence of stress, $\Delta\rho$ is the density difference in the solid and liquid during LPS, g is the gravitational acceleration, H is the height of solid above the location under consideration, D is the size of the particles, γ is the solid-liquid interface energy and Vv is the volume fraction of the solid. It was assumed that the increased volume fraction in gravity affects the rate constant K_0 in equation 2.19 but does not affect the value

of the exponent n in equation 2.10. The empirical relation between the volume fraction and the rate constant was expressed as follows:

$$K_0 = K_1 + K_L / (1-Vv)^{2/3} \qquad 2.20$$

where K_1 and K_L are constants determined by fitting the experimental data, and Vv is the solid volume fraction. Based on this model, one can predict the mean size as a function of time ,for both normal gravity and microgravity enviornments.

Microgravity experiments on Fe-Cu and Co-Cu have been investigated by Smith et al.[54-57]. During sintering, gas was intentionally introduced as a third phase. This resulted in extensive pore formation and metamorphosis. They have studied the densification behavior and have explained the observations based on minimum energy configurations, and metamorphosis.

2.6 Quantitative Analysis of Microstructure and Stereology

Microstructure can in general be defined as a collection of linear (e.g. dislocations), planar (e.g interfaces), and volumetric (e.g. particles) features present in 3-D in a background phase (matrix). These features are grouped by their properties and a microstructure may have many groups of features present simultaneously(e.g. particles, fibers, voids, etc.). The presence of background phase is not necessary as is in the case of space filling features (e.g. single phase space filling grains).

The microstructural quantities of a material can be roughly divided into three types. The first type are *field specific quantities*. These quantities describe the collective properties of all features belonging to a specific group present in a field of the microstructure. Volume fraction, surface area per unit volume, length per unit area, etc. of a specific group of features are *field specific quantities*. The second type are *feature specific quantities*. These represent average or distributive properties of features of a group. Examples of *feature specific quantities* are average size, average shape, size distribution, etc. of the group. These do not give the relative amounts of the features w.r.t. the field, as given by *field specific quantities*. The third and the last type of quantities known as *space descriptive* have the property of both the *field specific* and the *feature specific quantities*. They are field specific because they describe the proportion of a group of features w.r.t. the field. And they are feature specific because in order to measure them, each feature needs to be measured separately. *Space descriptive* type of quantities range from single valued to very complex functions. The single valued quantities of this type are number density (number of features per unit area), mean nearest neighbor distance, etc. All the spatial decriptor functions belong to this group (See Table 2.4).

The amount of information contained in each quantity varies depending on its type, and so does the amount of effort needed to measure it. For example, to accurately measure volume fraction, point counting on parallel metallographic planes can be performed, but for surface area per unit volume, measurements on planes of different orientations need to be taken. The *space descriptive* type of parameters contain the maximum amount of information

and thus the maximum effort is required to estimate them. The rest of the chapter deals with some basic microstructural quantities of interest and some frequently used spatial descriptors.

2.6.1 Basic microstructural attributes

One of the simplest property which describes a microstructure is volume fraction (V_V) of individual phases. This can be estimated by point counting, i.e. the fraction of points which fall on the phase of interest w.r.t. to the total number of randomly placed test points on the microstructure. Central limit theorem can be used to calculate the 98% confidence interval on this estimate to judge the accuracy of the measurements.

Another useful microstructural property which is relatively easy to estimate is the interfacial surface area of grains w.r.t. the total volume of the sample (S_V). These interfacial surfaces present in 3-D are seen as lines on 2-D metallographic planes. The number of intersections of these surface lines with the test lines per unit test line length gives an estimate of S_V by the following equation:

$$S_V = 2\overline{P_L} \qquad 2.21$$

where

$\overline{P_L}$ is the mean number of intersections of the interface with the test lines per unit test line length.

Both V_V (volume fraction) and S_V (surface area per unit volume) are field specific

properties.

2.6.2 Grain size shape orientation

There are many ways of defining size of discrete 3-D features (eg. grains, particles, pores,etc) present in the microstructure. Some of the most common ones are[58] ASTM grain size descriptor, mean grain intercept length, Jeffrie's grain size descriptor, etc. None of these descriptors report the true average grain size (i.e. average mean calliper diameter). Knowledge of distribution of mean calliper diameter is a very useful property because it can be used to estimate mean surface area per feature, mean volume per feature and a number of other mean properties along with number of features per unit volume. In this research the grain size was calculated by transforming 2D grain size into 3D using Schwartz-Saltykov[59] method. This method to transform the sizes from 2D to 3D is only applicable to spheres. The use of this method for our case is thus an approximation. (The 2D grain size was taken as diameter of equivalent circle with same area as the grain, as illustrated in Figure 2.10)

A more detailed description of transforming 2D grain size into 3D is given in section 2.10.

2.6.3 Neck size, shape and orientation

The interparticle necks are like circular disks with a slight curvature as shown in the Figure 2.4. If we approximate them with flat circular disks then they can be fully described by specifying the size and orientation of these disks. These necks will appear like lines of different sizes and orientation on the metallographic section. Two angles are required to describe an orientation, but in cases where microstructure has rotational symmetry about an

axis (eg., gravitational axis), one only needs one angle α (Figure 2.11) to describe the orientations[60]. This results in a bivariate size and orientation distribution. This bivariate size-orientation distribution is transformed from 2D to 3D to get the neck size and orientation distribution[60,61].

2.6.4 Derived properties

From the knowledge of some of the above properties it is possible to derive some other useful microstructural properties, one of which is mean grain separation λ. This is the mean value of the distance travelled in the matrix before any grain is reached. This gives a rough idea of the diffusional length scale, and is expressed as [3]:

$$\lambda = (V_V)_L / N_L \qquad 2.22$$

Another such property is contiguity[3]. It is defined as the ratio of solid-solid surface area to the total surface area.

$$C_{SS} = S_{SS} /(S_{SS} + S_{SL}) \qquad 2.23$$

This gives a measure of the solid solid contact and the rigidity of the skeleton. Another measure for the solid-solid contact is connectivity, defined as the number of contacts per solid grain. This can be estimated by taking the ratio of number of grains per unit volume to number of necks per unit volume. A connectivity value of more than 2 means a connected

structure.

2.6.5 Volume weighted mean volume

Particle size distribution can be represented in many different ways apart from the usual number distribution. The number distribution of particle sizes represents the fraction of the total number of particles which have a size within a certain size range. Another possible distribution is volume-weighted distribution of particle sizes. This distribution of particle size represents the fraction of the total volume of the particles which is contributed by particles within a certain size range. A typical number-distribution and volume-weighted distribution is given in Figure 2.12. Mean particle volume calculated from number-distribution of particle sizes gives the arithmetic mean particle volume ($\bar{v}_N$) of the particles, whereas mean particle volume calculated from volume-weighted distribution of particle sizes gives the volume-weighted mean particle volume($\bar{v}_V$) of the particles. The volume-weighted mean particle volume($\bar{v}_V$) can be comprehended as the arithmetic mean of particle volume weighted by their own volumes. Thus, mean volume of particles sampled with a probability proportional to their volume will give volume-weighted mean particle volume($\bar{v}_V$). An estimation for $\bar{v}_V$ can be obtained if particles are sampled with a probability proportional to their volume and mean volume of all these particles can be estimated by point intercept method [62,63]. The probability of a uniform random point to hit a particle in 3D is proportional to the volume of the particle, therefore can be used to sample particles with proper weight. In practice a uniform array of 2D points can be laid over the metallographic section and only the particles in which the points fall be sampled. The volume of the sampled

points can be estimated by point sampled intercept with a multiplicity equal to the number of uniform random test points in the particle. Suppose n test points hit the particles resulting in n point sampled intercepts, then

$$\overline{v_v} = \frac{\pi}{3}\frac{1}{n}\sum_{i=1}^{n} l_{0i}^3 \qquad 2.24$$

where l^3_{0i} is the i^{th} , (i=1,2,..n), point sampled intercept. From the definition of $\overline{v}_N$ and $\overline{v}_V$ (see the equations below) one can calculate the standard deviation and thus coefficient of variation of the individual particle volume

$$\overline{v_N} = \frac{\int_0^\infty v\, dN}{\int_0^\infty dN}; \qquad \overline{v_V} = \frac{\int_0^\infty v\, dv}{\int_0^\infty dv} = \frac{\int_0^\infty v^2\, dN}{\int_0^\infty v dN}, \qquad 2.25$$

Thus,

$$\overline{v_V} = \frac{\int_0^\infty v^2\, dN}{\overline{v_N}} \qquad 2.26$$

and so the coefficient of variation is given as

$$CV_N(v) = (\bar{v}_V/\bar{v}_N\text{-}1)^{1/2} \qquad 2.27$$

The value of $\bar{v}_N$ can be estimated by disector or its derivatives (see section 2.11)

2.7 Spatial Descriptors

Spatial descriptors are functions derived from the relative locations of features (particles in our case), which describe spatial patterns like randomness, clustering, repulsion, correlations and short and long range interactions. It is assumed that a map of spatial patterns is known[1] and we wish to extract information from this in the form of spatial descriptors. For simplicity each feature on the map is treated as a set of attributes which defines the feature and its relation to the whole field(map). Some of the common attributes used to define a feature are its position (centroid coordinates), size, shape, perimeters, orientation, minimum and maximum diameters, etc. Although this does not fully define the feature, it is good enough for practical purposes. If the features are equiaxed then the knowledge of orientation, and minimum and maximum diameters is unnecessary. For such features the spatial description reduces to description of point (with an added attribute of size) in 2 or 3-D. The science of spatial point processes broadly classify the point patterns in the following six classes[64]: Regular, Regular cluster, Random cluster, Regular-random, Hard-core and, Poisson pattern. These point patterns are shown in the Figure 2.13. The Hard-core and the

Poisson pattern are random point patterns with some constraints. One of the objectives of the spatial descriptors is to be able to distinguish between these point patterns and to be able to classify the given map into one of these.

In this section all the spatial descriptors are for a system Ω of spheres ω_j (j=1, 2,..) in a R^3 space (i.e. in 3-D), unless specified. In the R^3 space a Cartesian coordinate system (X_1, X_2, X_3) is defined, relative to which centroids of the sphere are given as x_{1j}, x_{2j}, x_{3j}. The sphere diameters D = D(ω_j) are distributed (but not necessarily independent) random variables with the distribution function F(D). In general the position and the diameters of the spheres are not independent; rather they are correlated. These correlations come from some nonrandom constraints imposed on the system, for example non-overlapping condition is one such constraint. If the position of spheres and their diameters are mutually independent then overlapping of spheres is possible.

2.7.1 K & G Function:

K-Function[65-69], K(r) is defined as the average number of particle (in our case spheres) centroids in a test sphere of radius r drawn around an arbitrary particle center and averaged over all centers. For a random distribution of particle centroids, or for random arrangement of point spheres (i.e. particles of zero size) the K-Function is equal to 4/3 π $r^3.N_V$ (N_V denotes the average number of spheres per unit volume in the given collection Ω of spheres). A value higher than this implies clustering and a value lower than this indicates repulsion of the particles.

The Radial Distribution Function (RDF)[65-67], G(r) is derived from the K-function,

and is defined as follows:

$$G(r) = \frac{1}{2\pi r N_A} \frac{dK(r)}{dr} \qquad 2.28$$

G(r) is a normalized number distribution function. $G(r).2\pi.r.N_A.dr$ (= dK(r)) gives the number of particle centers within this circular ring about an arbitrary particle (G(r)dr gives the ratio of number of particles with in a circular ring of radii r and r+dr about an arbitrary particle w.r.t. that in a randomly distributed particle system). Thus G(r) is so normalized that for a random point particle microstructure, its value becomes unity (independent of r). For a non-random point particle microstructure a value of G(r) greater than unity signifies clustering and a value less than unity signifies repulsion. Note that the case of non-point particle will be slightly different. In a typical K-Function and RDF for randomly distributed non-point particles, it can be seen (Figure 2.14) that the value of K-Function is zero to some distance r and that the RDF starts from zero (which in case of randomly distributed point particle is always unity from the start).

This is because the particles are of finite size (non point particles) and so there can be no particle centroid till the boundary of the particle. Both these distributions are useful mainly for short distance spatial distribution descriptions because as $r \to \infty$, $K(r) \to \pi r^2 N_A$ and $G(r) \to 1$.

If the spatial arrangement of particles is correlated w.r.t. sizes of the particles or if the

evolution of the microstructure depends upon the spatial arrangement of the particles of some specific size w.r.t. particles of another size then the K-Function and RDF are not of any use because they do not contain any information about the sizes of the particles. Hence another descriptor known as pair correlation function (PCRF) is defined as[67-69]

$$C(\Gamma_1,\Gamma_2,r)=\frac{1}{2\pi r\, n_v(\Gamma_2)}\frac{d^2Q(\Gamma_1,\Gamma_2,r)}{d\Gamma_2\, dr} \qquad 2.29$$

$C(\Gamma_1,\Gamma_2,r)$ is a normalized number distribution function such that 2π r n_V $C(\Gamma_1,\Gamma_2,r)$ $d\Gamma_2$ dr gives the number of particle centers of sizes between Γ_2 and $\Gamma_2+d\Gamma_2$ in a circular ring of radii r and r+dr about a particle of size Γ_1. This PCF is analogous to RDF. Here n_V (Γ_2) is particle size distribution function and $Q(\Gamma_1,\Gamma_2,r)$ (analogous to K-Function) gives the average number of particle centroids belonging only to the particles of size smaller than Γ_2 in a circle of radius r centered on a particle of size Γ_1.

2.7.2 Nearest Neighbor Distribution Function

Another way of describing spatial arrangements is through the nearest neighbor distribution function (NNDF)[70-72]. It is a probability distribution function P(r) which gives the probability of finding a nearest neighbor at a distance r per unit increase in r. More precisely P(r) is the probability such that P(r) dr is equal to the probability that there is no other particle centroid in a circle of radius r around another particle and there is at least one particle centroid in the circular ring of radius r and r+dr. This NNDF has a drawback w.r.t.

K-Function and RDF because it only gives information of nearest neighbor and no information of particles after that. Due to this shortcoming the concept of nearest neighbor has been extended to define 2nd, 3rd, etc. NNDF but it is not so convenient to use so many distribution functions. One major advantage of NNDF is that we can come up with one single valued parameter to roughly describe the microstructure i.e. average nearest neighbor distance which is the expectation value of the NNDF i.e.

$$\bar{r} = \int_0^\infty r\, P(r)\, dr \qquad 2.30$$

But still the NNDF do not give any information about the size correlated spatial arrangements. This can be included by defining the PNNDF. $P_p(\Gamma_1,\Gamma_2,r)$ such that $P_p(\Gamma_1,\Gamma_2,r)$ $d\Gamma_1\, d\Gamma_2\, dr$ gives the probability of finding a nearest neighbor of size between Γ_2 and $\Gamma_2+d\Gamma_2$ in a circular ring of radii r and r+dr about a particle of size between Γ_1 and $\Gamma_1+d\Gamma_1$. It should be noted that the extension of NNDF to PNNDF is different from the extension of RDF to PCRF because in the latter case it is possible to reconstruct RDF from PCRF but it is not possible to construct NNDF from PNNDF.

For ease of analysis the PCRF and PNNDF have been calculated by assuming only three discrete particle sizes. Let there be a particle size distribution with average particle size as $\bar{d}$ and standard deviation as $\sigma(d)$ then particles of sizes below $\bar{d} - \sigma(d)/2$ are regarded as small (s or size = 1), particles of sizes above $\bar{d} + \sigma(d)/2$ are regarded as large (l or size = 3)

and particles of sizes in between the two as medium (m or size = 2). The PCRF and PNNDF are then written in shorthand notation with reference to these size numbers. C_{ij} (r) is the PCRF for size i to j such that $[C_{ij}(r)]\ 2\pi r\ N_{Aj}\ dr$ gives the number of particles of size j in a circular ring of radii r and r+dr about particles of size i (i,j = 1,2,3). N_{Aj} is the number of particles of size j per unit area in the plane of observation. Similarly P_{pij} (r) is PNNDF for size i to j such that P_{pij} (r) dr gives the probability of finding a nearest neighbor of size j in a circular ring of radii r and r+dr about a particle of size i. (i,j = 1,2,3).

By this definition of PCRF it can be seen that $C_{ij} = C_{ji}$,but same is not true for PNNDF i.e. $P_{pij} \neq P_{pji}$.

2.7.3 Frequency function of inter-particle contacts

In microstructures having high solid volume fraction, another important descriptor of short range spatial arrangement of grains is the frequency distribution of number of inter-particle contacts per grain. Average number of inter-particle contacts per grain (known as coordination number) appear as an important input parameter in the theories and models for sintering, particle packing, percolation, etc. However, to the best of our knowledge, there have been no direct experimental measurements of the frequency distribution of inter-particle contacts in three-dimensional material microstructures due to lack of suitable experimental techniques. There have been attempts of correlating measurements of inter-particle contacts in 2D to that in 3D by simulating 3D microstructure[73] but there is no general relation relating the two. A relationship for the above has been derived in Chapter IV under the restricted assumption of monosized spherical particles. The number of inter-

particle contacts observed in 2D are always expected to be less than that present in 3D, thus as expected a large variation in mean number of inter-particle contacts in 3D results in a small variation of mean number of inter-particle contacts in 2D (Table 2.5), thus prediction of 3D mean number of inter-particle contacts from 2D measurements is poor. Moreover these correlations are very subjective and depend on the parameters of simulation.

2.7.4 Relative Variance

In a microstructure features may seem to have a homogeneous arrangement, but on decreasing the sampling volume, the inhomogeneity in the arrangements becomes apparent. Relative variance is a single valued parameter[74] which describes the extent of inhomogeneity in the system.

Each sphere in the system has a value x of a parameter X. In three dimensions it may be the volume of the sphere. For the spheres , X is a random variable with the distribution F(x), the expected value E[X] and the variance $\sigma^2[X]$. A test volume (a test field T) of size M is considered in the 3-dimensional space of the system (this may be a test cube in the microstructure). Particle density N_M is defined as the number of sphere centers present inside the test field per unit volume. If the test field is placed randomly, the number of spheres with centroids within the test field N = N||T and the parameters X||T of the particles within the test field are random variables (the notation || means within, e.g. N||T means N within the test field T). The probability distribution for N=N||T is

$$Pr(N=n) = p(n) \qquad n=0,1,2,.. \qquad 2.31$$

It has an expected value E[N] and the variance $\sigma^2[N]$. A value Y is defined based on the parameter X of the particle i (Xi = Xi||T) as

$$Y = \sum_{i=1}^{N} X_i \qquad 2.32$$

The values Xi (i=1,2,..N) within one test field are in general not independent variables (they are correlated with a correlation coefficient $\rho(Xi,Xj)$, $i \neq j$), but all have the same distribution function F(x). Y is the sum of N random variables Xi (i=1,2,..N), thus Y is also a random variable with distribution function F(y), an expected value E[Y], and variance σ^2 [Y]. Then the relative variance is defined as:

$$H[Y] = \frac{\sigma^2[Y]}{E^2[Y]} \qquad 2.33$$

After some manipulations it can be shown that:

$$H[Y] = (M.N_M)^{-1} \frac{\sigma^2[X]}{E^2[X]} + \frac{\sigma^2[N]}{E^2[N]} + (M.N_M)^{-2} \frac{\sigma^2[X]}{E^2[X]} C \qquad 2.34$$

where

$$C=\sum_{n=2}^{\infty} p(n) \sum_{i,j=1,j\neq i}^{n} \rho(X_i, X_j) \qquad 2.35$$

N_M is the particle density, and M is the test field size. It can be seen that the greater the size of the test field the smaller the value of H. That means, as the size of the field increases, the value of H is less influenced by the correlations between the values Xi. This is as what one would expect on increasing the size of the test field.

2.7.5 Covariance

Covariance C(r) is defined as the probability that two random test points, with distance r apart,lie within the particles (spheres)[75]. In the sphere system Ω in R^3, let there be two test points a distance r apart. Then [$\mathbf{x} \in \Omega$, $\mathbf{x+r} \in \Omega$] denotes the random event that both the points **x** and **x+r** lie in Ω. By definition covariance C(**x**, **x+r**) is the probability of the event [$\mathbf{x} \in \Omega$, $\mathbf{x+r} \in \Omega$]. For homogeneous and isotropic system Ω, the covariance depends only on the distance r and is independent of the position of the test point in R^3. Thus

$$C(r) = P[o \in \Omega \text{ and } r \in \Omega] \qquad 2.36$$

where o is the origin of the coordinate system and r a point at a distance r from the origin. C(r) is a continuous function of r with the following general properties.

$$C(0) = V_V \qquad 2.37$$

$$C(\infty) = V_V^2 \text{ , and} \qquad 2.38$$

$$C'(0) = S_V/4 \qquad 2.39$$

where V_V is volume fraction of the spheres and S_V is surface area of spheres per unit volume. The analytical expression for the covariance is known for a system Ω in which the position and the diameters of the spheres are mutually independent (i.e. overlapping is allowed). It is given by:

$$C(r) = 2V_V - 1 + (1-V_V)^2 \exp[\gamma(r)], \qquad 2.40$$

where

$$V_V = 1 - \exp[-\{\pi N_V/6)\langle D^3\rangle] \qquad 2.41$$

$$\gamma(r) = \frac{\pi}{12} N \qquad 2.42$$

and N_V is the number density of the spheres.

For a random system of non-overlapping spheres, the event [o ϵ Ω and r ϵ Ω] can be broken into a union of two events [o ϵ Ω and r ϵ Ω]$_1$ which denote that both the test points o and **r** lie in the same sphere, and [o ϵ Ω and r ϵ Ω]$_2$ the complementary one that the points lie in different spheres. The probability of the two sub events is denoted by $p_1(r)$ and $p_2(r)$. Then the covariance can be written as

$$C(r) = p_1(r) + p_2(r) \qquad 2.43$$

The probability $p_1(r)$ is given by $\gamma(r)$. From the functionality of $\gamma(r)$ it can be seen that the value of $p_1(r) = 0$ for $r > D_m$, where D_m is the maximum diameter of the sphere in the system. This implies that for small values of r (i.e. $r < D_m$) the value of C(r) are determined by the properties of a single sphere, while at large values of r the properties describe the spatial arrangements of the spheres.

2.7.6 Dirichlet Tessellations

Dirichlet Tessellation[64] is a construction in which a zone of influence is defined around each center (of sphere) consisting of that part of space which is closest to the selected sphere-center than to any other center. This uniquely defines neighbors of each center and divides the space into contiguous convex polyhedrons. These polyhedrons can be visualized by assuming a uniform growth about the sphere-centers in the space. These centers grow until mutual contacts prevent further growth (which appear as plane surfaces between the polyhedrons). This results in space filling non-overlapping polyhedrons. The surfaces of the polyhedrons can by obtained by connecting the perpendicular bisectors of the line segments joining the enclosed center with the neighboring center. This construction can very easily detect the type of spatial patterns, but is not good for quantitatively describing the spatial patterns.

2.7.7 Image analysis versus manual measurements

As seen in this section, the measurement of the spatial descriptors requires centroid

coordinates of all the particles which cannot be done on individual discrete fields. This is due to two problems inherently associated with discrete random individual fields. The first is the classical edge effect problem. This is the problem in accounting for the particles which are not totally in the field but cut the edge of the field (see Figure 2.15).

The second problem, which is more specific to the measurement of spatial descriptors. This is in trying to measure the position of particles present in one field w.r.t. particles in some other far away field (Figure 2.16). Thus long range spatial information cannot be extracted from observations on individual fields of view (FOV). Also to estimate any attribute of a microstructure from a 2-D metallographic section in a statistically significant manner, it is necessary to measure the attribute at various sampling locations. This work is much more efficient when it is automated using digital image analysis. Furthermore, the section should be of a sufficiently high resolution so that the scale of each feature is much larger than the scale of the least count (and error involved) of the image analyzer. Since the least count of the image analyzer is 1 pixel, each feature should be at least of the order of 20 pixels, so that the measurement error is less than 5%. At magnifications to provide a resolution as outlined above, a typical microstructure shows only 30-40 features in an image. To resolve the dual problem of acquiring enough features to provide a statistically significant sampling and having a good resolution, it is required that a tiling or montage of images with contiguous borders and high (equal) resolution be created. This results in an image of high resolution large area (HRLA) of the microstructure.

The creation of HRLA also reduces the problem of edge effect by reducing the edge

length with respect to the area of the field (i.e. by reducing length to area ratio). That is by reducing the number of particles contained on the edge of the field with respect to the total number of particles present in the field. Because a montage is a big image covering a large microstructural area, it also contains large range spatial information. In the continuous montage (*composite field*) all the particles present in different fields can be referred w.r.t. the same origin, and distance between any two particles present in different fields can be measured.

2.8 Image Analysis

A problem very common to image analysis is of feature separation. The image analysis system identifies features on a binary image which are made by thresholding grey image. The system identifies two features as separate if the features are not connected on the binary image. Due to finite size of pixel, limited grey levels and microstructural characteristics, many times different adjacent features get connected by some pixels on the binary image. Thus the image analysis system perceives them as one particle. Thus it is required that the image analysis system should be able to separate them. This can be achieved by different image processing algorithms. One algorithm to separate adjoining features is known as *Grain Algorithm* (the name grain comes from the fact that it grows each particle from their center as grain grows from its nucleus, and lets them impinge each other). In this algorithm the binary image is eroded pixel by pixel. By doing so the particles grow small in size, and so do the connecting bridges between the touching particles. Because the

connecting bridges are very small as compared to the particles and hence after a few erosions all the particles get separated on the binary image. This separates adjoining particles but results in particles of size smaller than original. Thus they are dilated (regrown) by equal number of steps to achieve the original size, keeping their separate identifications.

This process does achieve separation but it produces two errors. Particles which are very small (smaller than the size of joining bridges) get removed during erosion. Once a particle is totally lost during erosion it cannot be generated during dilation. Secondly the process of regeneration (dilation) cannot achieve the exact shape for the features (particles) as initial. Due to these limitations the grain process is used with a modification.

In this modification the initial binary image is stored in a buffer. The grain process is then applied to the image (without changing the buffer). The dilation is carried out beyond the point where the same size is achieved. This results in particles of size bigger than their original size, but the identity of separate particles is still kept. This separate identity is used to draw one pixel thick lines between different particles. The resulting image contains particles of a bit bigger size than the original, separated with one pixel thick lines. This image is then combined with the initial image stored in the buffer using Boolean AND to get the final image. This final image thus has particles of the same size and shape as original along with one pixel thick line of separation between them. This is shown in Figure 2.17. The Figure 2.17a is the initial grey image which when converted to binary image is shown in Figure 2.17b. The adjacent particles with the same color are perceived as one particle by the image analysis system. Some of the particles which are shown with the same color may

seem to be separated but are not and are connected by some pixels (which is less readily distinguishable on the photograph). Figure 2.17c shows the same image after carrying out the process of separation.

Once a continuous montage of FOV is stored and the particles are separated the final step is to extract data out of it. The main problem is posed by the image analysis systems which can measure only one screen at a time. Thus to get away with the edge effect problem the first field of view is initially displayed on the screen (*analysis screen*). The measurements are done on a frame of size one fourth of the analysis screen (known as *measurement frame*) (see Figure 2.18).

The particles which have their centroids inside this *measurement frame* are measured and the rest are not (they will be measured in subsequent *measurement frames*). The next analysis screen is displayed by taking half of the first FOV and half of the second FOV.

The measurement is again done on a measurement frame (centered on the screen) of size one fourth of that of the analysis screen (see Figure 2.19). Similarly all other FOV are analyzed using this procedure. By doing this all the particles present in the montage are measured and the same particle is never measured twice.

The output of the image analysis program gives the coordinates of the centroids of every particle w.r.t. a common origin. It also gives other attributes like size, shape, aspect ratio, etc. of each particle. This data contains all the information present on the montage (composite field). Thus once this data is extracted from the montage all the measurements and calculations can be done through this data without going back to the montage. This data

is used to get the required spatial distribution functions.

2.9 Three Dimensional Volume Reconstruction

Volume image data has been extensively used for the purpose of understanding and visualization of structures and processes. Sources of volume data differ in modalities and are found in different fields of science. In biology X-ray computer tomography(X-ray CT), single photon emission computer tomography (SPECT), positron emission tomography (PET), magnetic resonance imaging (MIR) and ultrasound imaging are some of the most common modalities. In civil engineering ocean bed sonography and atmospheric imaging is common; in materials science optical microscopy, scanning electron microscopy, transmission electron microscopy and X-ray CT are common modalities.

The volume data generated in this research is by stacking slices of serial sections of a tungsten heavy alloy by optical microscope, the details of which are given in the chapter on experimental work. The steps required to visualize this data are: Data generation (which we already have in the form of serial sections), Pre-processing (image alignment and correction, grid regularization, image enhancement and interpolation), Data classification, and finally Rendering. The volume visualization can be done by either surface rendering or volume rendering (explained below).

The smallest element of a volume data are voxels (3D analog of pixels) or cells. Each voxel contains one data sample whereas each cell contains 8 data samples (see Figure 2.20a), the only difference in the two is in the way of representation. The same volume data can be

represented by voxels or cells, depending upon whether surface rendering or volume rendering is required. The volume data can be organized in cartesian, regular, rectilinear, structured, block structured or unstructured grids (see Figure 2.20b). The type of data organization depends on the type of imaging modality. If it is different from cartesian or regular then data organization needs to be regularized into a cartesian or regular grid by linear (or higher order) interpolation. The 2D images of the serial sections used in this research were acquired by CCD and were organized in cartesian grid, but the spacing between the sections was not equal, thus the volume data was organized in rectilinear grid. The variation in the section spacing was measured and was found to be insignificant, thus the grid was considered as regular without the need of grid regularization.

2.9.1 Surface and Volume Rendering of Three-Dimensional Images

Surface rendering is defined as rendering of iso-surface of the region of interest (ROI) from the volume data, on the other hand volume rendering is defined as the rendering of all the volume data by defining color and opacity of each voxel. The advantage of surface rendering is that it results in reduction of data (only surface data is retained) and is easy to understand, but has disadvantages in that a lot of volume data is discarded and thus one needs to extract iso-surface data every time one changes ROI. Volume rendering on the other hand has the advantage of retaining all the volume information, but is disadvantageous also because it has to handle all the volume data set which results in slow processing.

In the process of volume rendering all voxels are visualized by specifying a mapping between rendered image intensity and voxel intensity. The volume rendering done in this

research is by Ray-Casting algorithm [76]. The basic idea of this algorithm is to cast a ray from the eye through the image plane and collect color and opacity at intersected voxels (see Figure 2.21a). Because the data traversal in this is from the image plane to the volume, it is known as image order algorithm.. Along each ray cast from the eye, the field is expressed as a function of the ray parameter. The algorithm computes properties of the field along the ray such as the attenuated intensity, the peak density, and the center of gravity, etc.(these are affected by the type of connectivity of the voxels as shown in Figure 2.21b) These are mapped into HSV color space to produce an image for visualization. Images produced in this manner are perceived as a varying density 'cloud' where intensity highlights the computed attributes.

The data classification step for surface rendering requires fitting of a surface in the volume data. The basic idea in data classification is to look for one surface to visualize, identify the intensity corresponding to that surface and threshold the selection. One of the oldest surface rendering algorithm is contour connecting algorithm [77]. In this algorithm iso-contours are thresholded and extracted in each slice (serial section), then contours between adjacent slices are connected and then rendered. The main deficiency of this algorithm is the problem in connecting contours between adjacent sections as shown in Figure 2.22a. The algorithms used in this research to extract iso-surfaces is known as marching cubes[78]. In this algorithm cell representation of the volume data is taken. Each data sample in the cell (i.e. each vertices of the cell) is considered either inside the surface of interest or outside depending on whether it is above or below the threshold value. For a

cubic cell there are 256 (because there are 8 cube vertices => 2^8=256)possible above/below threshold combinations, but only 15 unique (canonical) cases are possible. For each of these case one can interpolate the surface intersection along the edge as shown in Figure 2.22b, and generate surfaces and surface normals. These iso-surfaces can then be used for surface rendering.

2.10 Measurement of Number Density

Number density (i.e. number of particles or features per unit volume) is a property which often interests scientists. One reason for this is that it leads to calculation of average aggregate properties per particle (e.g. mean volume of a particle, mean surface area of a particle, etc.). At times number density is an important property by itself. For example in creep cavitation the change in number density of cavities, or in sintering the number density of voids and of powder particles, in nucleation studies the number density of grains, etc. are places where number density is an important variable. Apart from Materials Science, number density is an important parameter in many other natural sciences like Biology (cells, organelles), Petrography (mineral particles, or voids), Geography, Ecology, etc.

2.10.1 Estimation of number density (Nv) from observations on 2D metallographic section

There is a class of techniques for estimation of number density (Nv) from observations on 2D metallographic section. All these techniques can be viewed as a special case of a more general problem of unfolding of three dimensional particle size distribution from 2D observations. In an aggregate of particles; size, shape and orientation are the three

basic variables which dictate the structure seen on a metallographic plane. If we are able to unfold this multivariate distribution from observations made on plane section then it is trivial to estimate N_V from the knowledge of mean 3D calliper diameter from the following equation:

$$N_V = \frac{N_A}{\overline{D}} \qquad 2.44$$

The general steps in the methodology to calculate number density from measurements done on 2D plane sections are as follows:

i Assumptions: Assume a shape of the particles. The only shapes for which solutions exist are simple shapes of revolution. Variation in shape about a single type of shape (e.g. ellipsoid) has also been attempted. Next step is to sample the microstructure by planes of random angular orientation to get a bivariate shape-size probability distribution (pdf) in 2D.

ii Relation between 2D and 3D: Derive a equation relating the pdf of section sizes and shapes to the pdf of 3D sizes and shapes. This is done using conditional probability calculus and the geometry of particles. This usually results in an Abelian type of integral equation (or double Abelian integral equation).

iii Inversion of the integral equation: This requires complex numerical calculations to invert the Abel integral equation. This results in a 3D size distribution (or size-shape distribution) of the particles.

iv Calculation of Nv: Nv can be calculated by either using the above equation or by summing up all the number densities of all the 3D size classes. This is in general related to the harmonic mean of section sizes.

It is far too complex to study every variation of shape, thus studies have been centered about ellipsoidal shaped particles. Ellipsodal shape can be used to model a variety of shapes just by changing the eccentricity of the ellipsoid. Unfortunately the general problem of triaxial ellipsoid (with one size and two eccentricity) is indetermined (merely not solvable)[79]. Thus the attempts have been to solve biaxial-ellipsoidal problem. Wicksell (1926)[80] was the first to consider this problem. Since then many researchers (DeHoff[81], Tallis,82], Moran,[83], Luis[84,85]) have solved some special cases of either the general problem of triaxial ellipsoid or biaxial ellipsoid. A complete solution of the biaxial-ellipsoid problem (with all the particles being either prolate or oblate) has been solved by L.M. Cruz Orive(1976)[79].

Advantages of section measurements

i The biggest advantage of these methods is that measurements are only required to be made on 2D sections, which is relatively easy and less time consuming.

ii Another big advantage is that the Nv value for each size class is known. Thus the whole size distribution is known, which can be used to calculate distribution of any property of the particles (provided the shape assumption of the particle holds true).

iii Better sampling can be done and error bars can be estimated because the measurements are done on plane sections.

vi The smallest particle which can be measured is equal to the size of the image pixel which can be changed by changing magnification (this is a serious limitation of techniques which use 3D probes as will be discussed later).

Limitations and problems associated with these estimates of Nv:

i The very first limitation is the assumption of a constant shape. No material microstructure has all the particles of a same shape or of a type of shape. Moreover the real shapes of particles are much more complex than simple ellipsoids.

ii The second limitation is more of a practical limitation in the estimation of Nv. This is because sampling is required on planes with random angular orientation unless the microstructure is itself random (which is very unlikely if the particles are anisotropic). It is very tough to produce randomly oriented metallographic planes and is also very inefficient to do sampling on these planes. This need for sampling on randomly oriented planes can be removed by sampling on vertical sections and incorporating orientations of each particle in the size-shape distribution. This was first done by Gokhale[60,61] in which he took size and orientation into account, thus eliminating the need for randomly oriented planes. This was further improved by Benes et al.[86] to account for shape, thus making it a trivariate distribution of shape, size and orientation.

iii There is a lot of error propagation in the inversion of the Abel integral equation. There is maximum error in the smallest size class, which contributes the maximum to the Nv (Nv is related to the harmonic mean of the size classes), thus contributing

to the maximum error.

In principle the solution of the problem of estimation of N_V from sample space of lower dimension is not possible. This is because to estimate N_V it is required that sampling procedure should give equal weight to all the particles (irrespective of their size, surface area, shape or orientation), whereas particles will appear with a chance proportional to their calliper diameter, or projected area or individual volume on test planes or test lines or test points respectively(i.e., on sampling space of lower dimensions). In general a probe of dimension k is a direct estimator of a d-dimensional characteristic only if $d = n - k$, where n is the dimension of the space embedding the object[87,88]. In our case we want to measure the number of particles (cardinality), which is a zero dimensional geometric characteristic (i.e. $d = 0$) in a 3-dimensional space (i.e. $n = 3$), thus we need a $k = 3$ ($= n - d$) dimensional probe to measure it. Hence to sample the particles without any bias of size, area, etc. we need a volume probe (i.e., 3D sampling space). Such 3D probes are possible through serial sectioning.

One of the first three dimensional probes was used by Dehoff[89] in 1968, by using sweeping plane technique through the 3D. Miles and Davy (1978)[90] also used a technique to probe 3D by using the information provided by a wedge section of a structure near the edge. The main difficulties associated with these were of a practical nature. Cruz Orive[91] proposed a method by examination of parallel serial sections without the need of reconstruction. This method requires exhaustive serial sectioning of the specimen and thus

is not very useful. For only measuring Nv one need not take many serial sections and one need not do volume reconstruction. In fact only two serial sections are needed to measure Nv, this technique is called disector.

2.11 Integral Test System, the Disector

In order to make the use of three dimensional probe more practical, a three dimensional integral test system, known as disector was described by D.C. Sterio[92] in 1984. Since then the idea of disector has given birth to many other estimators of size, like the selector, the nucleator, the rotator, etc.

2.11.1 Principle of Disector

Aggregate of particles in an opaque media can be regarded as grains with a fixed point associated with each grain (i.e. particle) according to a fixed but arbitrary rule (e.g. the grain centroid, or the grain 'top point', etc.)[93]. Now the estimation of N_V boils down to the task of being able to identify these fixed points in an unbiased manner in a sample volume. This is done by disector using two parallel, 2-dimensional planes which have been cut from the 3 dimensional specimen. This is known as integral test system (ITS). These planes are so cut that the known spacing between these planes, h, is less than the smallest possible particle size in the direction perpendicular to the planes. This is to ensure that no particle is left undetected in between these two planes. On one of the planes of this ITS the traces of the particles are counted within a known area *a* using an unbiased counting rule[94]. All the particles sampled in this way are looked for in the second section of ITS (also known as

'lookup plane'), and those not sectioned by this second plane are counted as Q^-. This is the number of particles (particle ends) in the volume of disector ($v_{dis} = ah$), and thus $N_V = Q^- / v_{dis}$.

2.11.2 Application of disector for other measurements

The greatest advantage of the advent of disector was not as a means for measuring number density but as a tool to sample features with equal probability, not biased by their size, surface area or volume. This property of disector lead to invention of a number of other estimators like selector[93], fractionator[95], and nucleator[96]. Apart from this disector sampling was used in this research for the first time to measure distribution of true 3D calliper diameters of the particles and frequency function of number of interparticle contacts in 3D (see section 2.7.3). The details of the measurements are given in section 3.2.7.

CHAPTER III

EXPERIMENTAL WORK

The central objective of this research is to quantitatively characterize the effect of gravity on evolution of three-dimensional microstructure during liquid phase sintering of tungsten heavy alloys. The investigation has been carried out on a set of liquid phase sintered specimens processed in normal gravity, and the corresponding set processed in the microgravity environment of NASA's space shuttle Columbia (MSL-1 flight, 1994, and IML-2 flight, 1997). The liquid phase sintering experiments were designed and conducted by Prof. R.M. German and his research group at Pennsylvania State University[8], in association with NASA-Lewis Research Center. A brief description of these liquid phase sintering experiments is given in the first section of this chapter. The focus of the present work is on the development and applications of serial sectioning, two-dimensional and three-dimensional digital image processing, three-dimensional microstructural reconstruction, and unbiased stereological sampling techniques for quantitative characterization of the liquid phase sintered microstructures. These experimental procedures are described in the subsequent sections of this chapter. The three-dimensional microstructural data obtained from this study are analyzed in the next chapter to quantify the gravitational effects on the microstructural evolution.

3.1 Liquid Phase Sintering Experiments

As mentioned earlier, microgravity and normal gravity liquid phase sintering experiments were performed by Professor R.M. German and his group at Pennsylvania State University, in collaboration with NASA scientists. The basic steps involved in these experiments are mixing of constituent powders, cold isostatic pressing to produce a green compact, pre-sintering in solid state, and liquid phase sintering in either normal gravity or microgravity. The experimental procedures associated with these steps are briefly described below.

Tungsten heavy alloys (WHA) can be classified into two groups, the one in which tungsten is insoluble in matrix in both solid and liquid state (e.g. W-Cu), and the other in which tungsten is partially soluble (e.g. W-Ni, W-Fe). The alloy with matrix of the latter type was chosen (7Ni:3Fe) for liquid phase sintering experiments. This was done because the solubility of tungsten increases the densification process by solution-reprecipitation[3,6,16], and lot of auxiliary data are available on this system. The phase diagram of the three binary systems and the ternary system are given in Figure 3.1. Weight fractions of W chosen were 78% (60% volume fraction) and 83% (67% volume fraction), and 93wt% (85% volume fraction). These compositions yielded sufficiently large volume fractions of liquid to investigate the gravitational effects on microstructural evolution, and at the same time, large enough fraction of tungsten grains to form a stable rigid skeleton that resists further settling in normal gravity. The serial sectioning, three-dimensional microstructural reconstruction, and direct three-dimensional microstructural measurements

were performed only on the specimens of 83wt%W composition, and the two-dimensional metallographic observations and measurement were performed on the specimens of all three compositions.

Elemental powders of W (Vendor: GTE, Purity: 99.95%, Mean particle size: 8.0 μm), Ni (Vendor: Inco, Purity: 99.99%, Mean particle size: 10.4 μm) and Fe (Vendor: GAF, Purity: 99.5%, Mean particle size: 6.3 μm) were blended in appropriate amounts, and then cold isostatically pressed into cylinders. The green compacts were pre-sintered at 1400 deg C in hydrogen atmosphere for three hours, to provide strength to the samples. The pre-sintering temperature was well below the liquid formation temperature of the Fe-Ni alloy. The pre-sintered specimens were machined to obtain cylinders of 10 μm diameter and 10 μm height. These specimens were then packed in alumina crucibles and vacuum sealed in tantalum containers with boron nitride lining. The vacuum sealed samples were liquid phase sintered at 1507 deg C for hold times of 1 and 120 minutes under both normal gravity on earth and in the microgravity environment of space shuttle Columbia (MSL-1 flight, 1994, and IML-2 flight, 1997). The experimental setup for the furnace is given in Figure 3.2. The final hold temperature of 1507 deg C showed a drift of approximately ±3 deg C. The average acceleration in microgravity was measured to be 4.4×10^{-5} m/s^2 with a maximum value of 9.1×10^{-5} m/s^2. The thermal cycles for the LPS of the samples are given in Figure 3.3. Details on liquid phase sintering experiments are given elsewhere[8].

3.2 Metallography

In the present liquid phase sintered microstructures, the axis of the cylindrical specimens (which is the direction of gravity during pre-sintering) is expected to be a symmetry axis, in the sense that, all metallographic planes containing this axis are expected to reveal statistically similar two-dimensional microstructural sections. Further, microstructural gradients in radial and longitudinal directions can be detected and studied via observations on any one such plane. Therefore, in the present investigation, all two-dimensional metallographic observations were performed on a central metallographic vertical plane containing the gravity direction during pre-sintering. The liquid phase sintered specimens (particularly those processed in normal gravity) contain microstructural gradient along the length direction (gravity direction). Therefore, to compare microstructural attributes of different specimens, it is absolutely essential to perform microstructural measurements at the same relative location in all specimens. In the present study, serial sectioning and three-dimensional microstructural reconstruction, and direct three-dimensional microstructural measurements were carried out in the region 1 mm from the "bottom" in all specimens of 83 wt%W composition. Further, in these specimens and in the specimens of 78wt%W and 93wt%W compositions, the two-dimensional metallographic observations and measurements were performed on the region 1 mm from the "bottom", as well on the region 1 mm from the liquid dome at the "top" of the specimens[1]. The

[1]Note that these is no "top" and "bottom" in the microgravity. In the present context, the "top" and the "bottom" refers to the corresponding locations during pre-sintering and other pre-liquid phase sintering steps carried out in normal gravity environment

specimens were mounted and polished with diamond polishing medium using standard techniques. For digital image analysis, it was necessary to develop a microstructure with good contrast between W grains and the matrix. This was achieved by using interface layering technique developed by Mr. T. Leonhardt at NASA Lewis Research Center. In this technique, the sample is coated with a thin film of platinum oxide (PtO) by sputtering platinum on the sample kept in oxygen atmosphere. For the present specimens, the following combination of sputtering process parameters resulted in optimum contrast between tungsten grains and matrix.

i. Distance between specimen and the platinum target: 1.8 cm

ii. Current: 40 milliamperes

iii. Sputtering time: 120 seconds

iv. Total pressure in the sputtering chamber: 0.1 mbar

v. Input (in to the sputtering chamber) pressure of oxygen : 10 psi

This technique should not be confused with phase contrast illumination or Nomarski interference technique, both of which require specialized light microscopes. Figure 3.4a and Figure 3.4b illustrate a typical microstructure revealed in this manner. Observe that the interface layering procedure leads to development of nice contrast between the tungsten grains and matrix, that is essential for digital image processing. However, the boundaries between the touching/contacting tungsten grains are NOT revealed. Therefore, to measure the sizes and some other attributes of the tungsten grain sections, it is necessary to develop an image analysis algorithm to segment these images and to "cut" the tungsten grains, so that

feature specific measurements can be performed on the tungsten grains. The image segmentation procedure developed in the course of this research is described in the next section.

3.3 Digital Image Segmentation

An important segmentation algorithm available in KS-400 image analysis system (and also in numerous other image analysis systems) to separate touching adjoining features is known as *Grain Algorithm.* As mentioned in Chapter II, in this algorithm, the binary image is eroded pixel by pixel. By doing so, the particles/grains shrink to smaller sizes, and so do the connecting bridges between the touching particles/grains. Because the connecting bridges are small as compared to the particles/grains, after a few erosions all the particles/grains get separated in the binary image. This procedure separates the adjoining/contacting particles, but results in particles/grains of sizes smaller than those in the original image. Therefore, to being the grains back to their original size, they are dilated (regrown) by exactly the number of steps to restore them to their original sizes, keeping their separate identifications. This process does achieve separation but it leads to two errors: (i) particles that are very small (smaller than the size of joining bridges) get removed during erosion. and such particles cannot be regenerated during dilation, and (ii) the process of dilation cannot achieve the exact shape for the features (particles) as in the initial image. In this study, the grain process algorithm has been improved to remove these two limitations.

In the modified grain process, the initial binary image is stored in a buffer. The grain

process is then applied to the image (without changing the buffer). The dilation is carried out beyond the point where the same size is achieved. This results in particles of size bigger than their original size, but the identity of separate particles is still kept. This separate identity is used to draw one pixel thick lines between different particles. The resulting image contains particles of a bit bigger size than the original, separated with one pixel thick lines. This image is then combined with the initial image stored in the buffer using Boolean AND to get the final image. This final image thus has particles of the same size and shape as original along with one pixel thick line of separation between them. This procedure is illustrated in Figure 2.17. The Figure 2.17a is the initial grey image which when converted to binary image is shown in Figure 2.17b. The adjacent particles with the same color are perceived as one particle by the image analysis system. Some of the particles which are shown with the same color may seem to be separated but are not and are connected by some pixels (which is less readily distinguishable on the photograph). Figure 2.17c shows the same image after carrying out the process of separation.

3.4 Quantitative Microstructure Characterization

Figure-3.4 shows a typical microstructure of a liquid phase sinterd tungsten alloy, observed in a metallographic plane. Note that, in this two-dimensional microstructural view, the majority of tungsten grains sections are connected to one another, but some isolated grain sections are also observed. Further, the apparent coordination number seems to be quite low (~1). It will be shown in the subsequent sections that such two-dimensional

microstructural observations are very deceptive. In the three-dimensional microstructure, the tungsten grains are almost completely inter-connected, and the three-dimensional coordination number is expected to be significantly higher than one. Therefore, quantitative characterization of three-dimensional microstructures (either via stereological relationships, or through direct three-dimensional measurements) is essential to understand the effect of gravity on microstructural evolution in the liquid phase sintered specimens. The three-dimensional liquid phase sintered microstructures contain geometric features such as three-dimensional volumes (tungsten grains), two-dimensional interfaces (interfaces between tungsten grains and matrix), and one-dimensional lines (necks). Important microstructural attributes associated with these features are as follows.

1. Metric properties of grains, interfaces, and necks
2. Number density of grains
3. Descriptos of spatial arrangements of grains
4. Grain size distribution
5. Bivariate neck size and orientation distribution

In the present investigation, microstructural attributes belonging to all the above groups have been experimentally measured. The estimation procedures for estimation of some of the attributes are well known, whereas others have been developed during the course of this work. The experimental methodology for quantitative characterization of microstructures and the resulting data are presented in the following sub-sections.

3.4.1. Estimation of Metric Properties

The following three-dimensional metric properties can be estimated from the measurements performed on representative two-dimensional metallographic sections through general unbiased stereological relationships.

i. Volume fraction of tungsten grains and matrix phases

ii. Total surface area of tungsten grains per unit volume

iii. Total surface area of tungsten-matrix interfaces per unit volume

iv. Total length of necks between tungsten grains and matrix per unit volume

v. Volume weighted average volume of grains

Volume fraction (of any phase) can be estimated from areal analysis[59], total surface area per unit volume can be estimated from line intersection counting[59], and total length per unit volume can be estimated from triple point counts in a metallographic plane[59]. In the present case, volume fraction was estimated using automatic digital image analysis, whereas the surface area and length density were estimated by using straight forward manual measurements. For estimation of volume fraction, the measurements were performed on about five hundred microstructural fields in each specimen; manual surface area and length density measurements involved observations on about fifty microstructural fields in each specimen. These stereological procedures are well known for long time, and therefore, not discussed here in detail. Table-4.5 gives the measured average values of volume fraction of tungsten grains, surface area per unit volume, and length density of necks for the microstructures under investigation.

Volume weighted average volume, v_V is an important three-dimensional attribute of population of grains that can be estimated from measurements performed on metallographic planes by using general and unbiased stereological realtioship given by Gundersen and Jensen[62], as discussed in Chapter II, section 2.6.5. Estimation of volume fraction of tungsten grains, their number density, and volume weighted average volume can be utilized to calculate the average grain volume, and the variance and covariance of the distribution of grain volumes in three-dimensions, without measuring volume of a single grain ! Traditionally, volume weighted average volume measurements have been performed manually. This involves measurements of large number of point sampled intercept lengths, which is time consuming and tedious. In this research, an image analysis procedure is developed to automatically measure point sampled intercepts for estimation of volume weighted average volume. This new procedure is described below.

Development of Digital Image Analysis Procedure for Estimation of Volume Weighted Average Volume

Segmented binary image having "cut" tungsten grains is the input for volume weighted average volume estimation. This image is stored in the memory of the image analyzer. Let us call this image-1 (see Figure 3.5a). Another synthetic image is created consisting of twenty-five equi-spaced horizontal lines and thirty equi-spaced vertical lines forming a grid that covers the whole field of view. The 750 points of intersections of horizontal and vertical lines are the test points needed for point sampled intercepts. In this synthetic image, the lines are "white" in the black background. Let us call this image-2 (see

Figure 3.5b). In the next step, a boolean 'AND' operation is performed on the images 1 and 2. The resulting image(image-3) is a collection of horizontal and vertical line segments resulting where both Image 1 and Image 2 had a gray scale value = 'white'. (See Figure 3.5c). Some of the line segments in the image-3 contain the grid points (i.e. test points) of Image 2, and therefore, these are the point sampled intercepts. All the other line segments (the ones that do not contain test point) are deleted from the image to form a new image, called image-4 (Figure 3.5d). The criterion used to differentiate (and thereby delete) these line segments is the aspect ratio of the features formed by these line segments. One of the ferret x or ferret y diameter of the features in this case is equal to one pixel. The ferret x and ferret y diameters of the features in image- 4 are then measured automatically; these are the point sampled intercept lengths required for estimation of the volume weighted mean volume (see equation 2.24) The volume weighted average volume data obtained in this manner are reported in Table 4.4.

3.4.2 Estimation of Number Density of Grains

It is well known that, in general, number of grains (or any type of features) per unit volume in three-dimensional microstructure can not be estimated from any measurements performed on two-dimensional metallographic sections. Direct sampling of three-dimensional microstructure is necessary for this purpose. In 1984, Sterio[92] presented an efficient three-dimensional stereological sampling probe, disector, for unbiased estimation of number density of arbitrary features in three-dimensional microstructure. Disector consists of two parallel sectioning planes separated by a known distance. The stereological

procedure involves use of an unbiased counting frame to count the number of features that are present in the second disector plane, but not present in the first plane (Q^-), and/or to count number of features that are not present in the first plane, but they are present in the second plane (Q^+). The quantity $[Q^{+or-}]/[A.t]$ is an unbiased estimator of number density of features N_V in three-dimensional microstructure, where A is the area of the unbiased counting frame and t is the distance between the two disector planes. Although this technique was developed more than fifteen years back, it has not been frequently used for estimation of number density of features in opaque material microstructures of metals or ceramics. In opaque material microstructures, application of disector requires storing of an image (or a micrograph) of an arbitrary field of view (FOV) in the first disector plane, physical removal of small known thickness of material by polishing followed by suitable etching to reveal microstructure, and grabbing of microstructural image (or micrograph) of a microstructural field of view (FOV) in the second disector plane that is exactly below the one observed in the first plane. The appearance and disappearance of microstructural features of interest are then counted on these two images by using an unbiased counting frame to estimate the number density N_V. In this process, the least amount of effort (at the most few minutes) goes into actual stereological counting, and large amount of effort (more than few hours in some cases) goes for physical sectioning, polishing, etching of disector planes, identification of the same microstructural region in the two sectioning planes, and alignment of the images in the two planes, and measurement of thickness (i.e., distance between disector planes) of the material removed. After all the tedious metallographic work, the microstructural volume on

which the measurements are performed consists of *at the most* one field of view (FOV) in cross-section (whose area is, typically, on the order of 250 μm X 250 μm) and few microns in depth. A typical disector counting on such a sample yields Q^+ (or Q^-) in the range of zero to two, i.e., statistical sample is equivalent to counting zero to two particle centers! Therefore, to obtain a reasonably precise estimate of number density and to decrease the sampling error, it may be necessary to repeat the procedure on (typically) fifty different disectors, which requires physical sectioning and generation of large number of metallographic planes, and therefore, it may involve months of metallographic work. It follows that, although conventional disector is an efficient stereological sampling probe, the efforts involved in other steps of the process (i.e., physical sectioning, metallography, etching, alignment, etc.) make this powerful technique extremely inefficient and impractical for precise estimation of number density in opaque material microstructures. The root cause of this inefficiency is the large effort required to collect a small number of disector counts due to small volume of the disector. In this research, a digital image analysis based solution has been developed to solve this problem through creation of a "mega-disector", where the disector planes have a very large area and high resolution, and the disector thickness is on the order of a micron or so. The disector planes of the mega-disector consist of a "montage" of very large number of contiguous microstructural fields of view (say twenty-five to hundred) grabbed at high magnification (and high resolution), precisely "pasted" together through an interactive image analysis procedure. Therefore, for about the same metallographic effort, mega-disector yields twenty-five to hundred times larger disector

volume (and therefore, counts) as compared to conventional single field of view disector, which makes it very efficient for estimation of number density in opaque material microstructures. The following sub-section describes this new technique for estimation of number density of grains in three-dimensions.

Development of Mega-Disector For Efficient Estimation of Number Density in Opaque Microstructures

Development of mega-disector involves creation of large-area high-resolution seamless montage of a large number of microstructural fields which forms first plane of the mega-disector, physical removal of small (known) thickness of material to generate second mega-disector plane, creation of large-area high-resolution montage on the second plane in the region exactly below the first one, measurement of distance between two mega-disector planes, alignment of the mega-disector planes, and unbiased counting of "top" and "bottoms" of grains in the two mega-disector planes. These steps are described below.

Creation of large-area high-resolution montage

In the present work, image analysis was done on KS-400 image analysis system from Kontron, Inc. However, several other commercial image analysis systems also have the required capabilities. The computer codes for creating the montage were written in a language similar to C in a platform provided by the image analysis software (KS-400). To create the montage, a first field of view (FOV) was arbitrarily chosen in the region of interest in the metallographic plane, and the image of this field of view was then stored in the memory of image analysis computer as an image file. The right border (of about 60 pixel

width) of this image was recalled on the left edge of a blank image. This semi blank image was then displayed along with the live image. This resulted in a superimposed image on the left border of the screen (of the previous right border and live image) with rest of the screen having the live image (see Figure 3.6). The computer controlled microscope stage was then automatically moved so that the right border of the live image moved to the left border and gives a reasonable match with the superimposed image. The physical movement of the automatic-stage has a large least count and thus cannot achieve perfect match with the previous image, thus small movements (to a least count of one pixel) of the live image were made manually using image analyzer to achieve a perfect match. This resulted in a match of the first and the second image with an accuracy of one pixel. The second image was then stored in the computer memory as another image file. All successive images are grabbed by using the same procedure and finally a continuous montage of fields was made. The details of montage creation are described elsewhere [97]. Figure 3.7a shows a montage of twenty-five fields of view, which has been compressed for display. Each region of this montage has a high resolution of the image shown in Figure 3.7b. Therefore, montage is a microstructural image of a large area (twenty-five fields of view at 500X) having high resolution. The present montages contain about 1200 to 1500 W grain sections.

Montage serials sectioning

Four diamond micro-hardness indents were made on the selected region (one at each corner) of the first mega-disector plane and a montage of twenty-five fields of view was created as described in the last previous sub-section. The micro-hardness indents were made

to measure the thickness of material removed (explained later) and to provide reference points to get back to the same location on the microstructure. A fixture was molded on the microscope stage which had a hole at the center to hold the sample. The fixture was so molded that it could hold the sample in only one orientation, keeping it aligned within an angle of ± 5 degrees . After making the indents a montage of the region was digitally grabbed (as described in the previous section) and labeled as section 1 and saved in the hard drive of a computer. The sample was then automatically polished with 3 μm alumina powder at 50 Newton force for 8 minutes. This results in removal of a thin layer (about 1 to 2 μm) of the sample. The sample was then cleaned, dried and coated with PtO (using sputter coater in O_2 atmosphere with Pt target) to develop contrast between the tungsten grains and Ni-Fe-W matrix by interface layering. The sample was then again taken to micro-hardness tester and new indents were made beside the old indents (which had grown small in size because of sectioning). After making the new indents the sample was placed in the fixture on the microscope stage and the stage was moved till the first corner of the rectangular region was seen in the microscope. The image of this FOV was superimposed on the image of the same region taken before sectioning (from image of section 1 stored in the hard drive). The micro-hardness indents were seen on the superimposed images and the microscope stage was moved till the indents on the two image were matched. This ensured that the location being viewed in the microscope was the same as in the previous serial section. After alignment, second montage of 5 x 5 FOV was grabbed, and stored in the hard-drive as an image labeled section 2. In this manner, a mega-disector was created.

Measurement of Distance Between Mega-Disector Planes

To be able to perform any quantitative measurements on the volume of mega-disector, one needs to know the exact amount of material removed by each sectioning so that the depth dimension of the volume generated is known. This thickness was calculated by measuring the decrease in the size of the micro-hardness indents. The indents were made by a square pyramidal shaped diamond with opposite faces at an angle of 136 degrees. This means that the ratio of the diagonal of the square formed on the section to the depth of the indent is $2\sqrt{2}\tan(136°)$ which is equal to 7.00. Thus for a unit change in diagonal length there was 1/7 change in the depth. The change in the diagonal was measured using digital image analysis for each section at each corner and mean value was taken and was used to calculate the change in indent depth and thus the thickness of each serial section. Figure 3.8 shows two images with micro-hardness indents. It can be seen that as the material is removed the indents become smaller in size

Alignment of Disector Planes

A typical problem in serial sectioning is that the consecutive sections are usually not perfectly aligned, they have some transnational and rotational displacement with respect to each other. In spite of adjusting the microscope stage, the serial sections grabbed were not perfectly aligned but were displaced by ±10 pixels and ±5 degrees, and thus needed to be perfectly aligned. Alignment can in principle be done by locating two common points in two consecutive serial sections and translating one image till the first common point is aligned in the two images. Then the image is rotated about this point till the second common point

is also aligned. This was done by using three-dimensional image analysis software Voxblast 3.10 in which the images of the disector planes were digitally translated and rotated till they were exactly aligned to the previous section. A stack of five aligned montage serial sections is shown in Figure 3.9.

Efficient Estimation of Number Density From Mega-Disector

Mega-disector was used to measure the number density of the tungsten grains in the 83 wt%W alloy. The disector was applied by superimposing montages of the two mega-disector planes in false color in the KS-400 image analyzer as shown in Figure 3.10. The first mega-disector plane was put as the red plane of the image and the second was put as green and blue plane. This results in a false colored image with particle tops (i.e. new particle sections which appear in the second slice but are not present in the first) appearing as red particles as shown in the Figure 3.10. The number of these tops were counted in the mega-disector (made by montage serial sections). This counting was performed on thirty such disectors at different depths for all the four 83 wt%W samples. This resulted counting of about 4000 W grains in 1 minute samples and 2000 grains in 120 minute samples. The number of grains per unit volume value were calculated for each disector (by dividing the number of tops by the area of the montage and the thickness of the disector) and mean values were calculated. These data are reported in Table 3.2

3.4.3 Descriptors of Spatial Arrangement of Grains in Three-Dimensional Structure

Important aspects of spatial arrangement of features/grains in three dimensional

microstructure can be quantified by using numerous different statistical functions, some of which are as follows.

1. Average coordination number
2. Bivariate frequency distribution of coordination number of grains
3. First nearest neighbor distribution of grain centers
4. Second, third, and higher order nearest neighbor distributions of grain centers
5. Radial distribution function of the grain centers

None of the descriptors of spatial arrangement of features/grains in three-dimensional microstructure can be estimated from any measurements performed on two-dimensional metallographic planes. Further, disector by itself (i.e., a pair of planes) is also not useful for estimation of spatial arrangement descriptors. To quantify spatial arrangement of features in opaque three-dimensional microstructures, it is necessary to recreate a sufficiently large segment of high resolution three-dimensional microstructural volume from a stack of large number of serial sections, and this is not practically feasible to do via conventional serial sectioning. To the best of author's knowledge, **there are no experimental data on descriptors of spatial arrangement of grains/features in opaque material microstructures reported in the literature**. This is due to lack of suitable experimental techniques for performing microstructural measurements in the three-dimensional space. Therefore, there is a need to develop efficient and unbiased practical techniques for quantitative characterization of spatial arrangement of microstructural features in three-dimensional space. A major part of this research effort has gone into development and

applications of such techniques for quantitative characterization of spatial arrangement of tungsten grains in liquid phase sintered microstructures. The present data on bivariate distributions of coordination numbers and first, second, and third nearest neighbor distributions are the first set of experimental data on these microstructural attributes.

Consider characterization of spatial arrangement of features in three-dimensional microstructure, which obviously involves measurement of inter-feature distances in three-dimensional space. For opaque materials, a segment of three-dimensional microstructural volume can be reconstructed from a stack of conventional serial sections. In the conventional serial sectioning [24, 25], one microstructural field of view on a metallographic plane is recorded (digitally or in a photo micrograph), the specimen is polished to remove a small thickness of material, and then microstructural field in the second metallographic plane in exactly the same region is recorded again. This polish-record image of field of view-polish procedure is repeated to generate a large number of serial sections (typically 50 to 100). The three-dimensional microstructural volume segment can be then reconstructed from such a stack of well aligned serial sections. The conventional serial sectioning technique is very inefficient, because it involves a lot of effort to generate only a small high resolution segment of three-dimensional microstructure. Such a schematic volume element is shown in Figure-3.11. The cross-sectional area of this microstructural volume segment is equal to the area of one microstructural field observed in a metallographic plane. Such small microstructural volume segment leads to serious errors due to "edge effects" in the estimation of spatial arrangement descriptors. For example,

measuring distance between two features present in Figure 3.11 as a nearest neighbor distance would be completely wrong, because nearest neighbors of these features are in the adjoining volume segments (Figure 3.12) which have not been reconstructed. This edge effect is far more serious in three-dimensions (as compared to that in two-dimensions) because there is one more degree of freedom. Note that, this bias is higher and higher for second, third, and higher order nearest neighbor distances. Further, from such small volume segment, it is obviously not possible to get any information about spatial arrangement of features at distances larger than about one third of the size of the volume element. Therefore, it may be concluded that the conventional serial sectioning is time consuming and inefficient, and it generates a small segment of three-dimensional microstructure which is not useful for quantitative characterization of spatial arrangement of features in three-dimensions.

To generate a large volume of three-dimensional microstructure at high resolution, one may first reconstruct many contiguous small volumes surrounding the one shown in Figure-3.11, and then perfectly match their boundaries and paste them together to generate a large volume of three-dimensional microstructure, as shown in Figure 3.12. If the volume of the recreated microstructure is sufficiently large then it can eliminate the "edge effects" for all practical purposes. Using such a high-resolution large microstructural volume, one can then precisely measure distances between two features located any where in such a three-dimensional "montage". In this research, a technique equivalent to such a reconstruction is developed and applied to liquid phase sintered microstructures of interest. First a "montage"

of twenty-five contiguous microstructural fields observed at 500X (high resolution) is created by using the large area high resolution montage procedure described in the section 3.4.2.1.1. This is followed by removal of small thickness of material (about 1 μm) by polishing and then a second montage is created at the region exactly below that in the first metallographic plane. In the present study, this polish-montage-polish procedure was repeated to obtain stacks of ninety montage serial sections for each specimen of 83wt%W composition. Micro-hardness indents were used to locate the exact region of interest in successive serial sections, and to measure the distance between consecutive serial sections (see chapter section 3.4.2.3). The ninety montage serial sections were then precisely aligned in the Z-direction by using the procedure described in the chapter section 3.4.2.4. Each montage serial section was stored in the computer memory as a separate image file. The effort involved in this process of creating a stack of montage serial sections is comparable that for the conventional serial sectioning, but the montage microstructural volume is twenty-five times larger than that generated by conventional serial sectioning. Therefore, such a high resolution large volume segment can be used to quantitatively characterize spatial arrangement of features in three-dimensions with high precision. Further, the use of montage leads to a very efficient serial sectioning technique as it can yields twenty-five times larger sample of three-dimensional microstructure then that obtained by conventional serial sectioning with the same effort. Estimation of various descriptos of spatial arrangement of grains in three-dimensional structure from the stack of ninety aligned serial sections is described in the next few sub-sections.

Estimation of Distribution of Coordination Number of Grains in Three-Dimensional Microstructure

Two approaches can be taken for the estimation of frequency function of number of inter-particle contacts. First approach is to carefully observe the inter-particle contacts of each grain through observations on successive serial sections, which is extremely laborious. The second more efficient approach is to sample the W grains from the population of grains contained in the stack of montage serial sections, and to estimate the distribution function from the observations on the statistical sample. The second approach was used in the present study. It involves (i) unbiased statistical sampling of tungsten grains from the stack of montage serial sections, (ii) counting of number of inter-particle contacts of each sampled W grain in three-dimensional structure *by systematically observing all serial sections in which the grain of interest is present*, (iii) repeating steps (i) and (ii) for a sufficiently large number of grains, and (iv) computing the frequency distribution of inter-particle contacts from the data obtained in steps (i) to (iv). It is important to point out that there is a strong correlation between size of W grains and number of inter-particle contacts. Therefore, for a reliable estimation of the frequency distribution of the number of inter-particle contacts, the sampling must be completely unbiased, i.e., all W grains must have the same chance of being included in the sample irrespective of their size. The only unbiased procedure for sampling particles/grains in three-dimensions, irrespective of their size or shapes, is through the use of disector [34]. The disector sampling consists of selecting only those W grains that are not present in the first serial section, but they are present in the second serial section

of the disector probe (grains tagged by arrows in the Figure 3.10). Therefore, disector detects the "tops" of the grains, and as each grain has exactly one "top", all grains have exactly the same probability of being sampled irrespective of their sizes and shapes, when disector location is chosen at random. In the present study, the area of the disector planes is equal to the area of the montage serial section, and disector thickness is equal to the distance between the serial sections. The number of inter-particle contacts of each W grain sampled by disector (i.e., whose top was detected) was measured by carefully observing all serial sections in which that particular grain was present, and then the caliper diameter (size) of that grain was measured from the (X,Y,Z) coordinates of the "top" and the "bottom" of the grain (this will be explained in detail in the chapter section 3.4.4). The process was repeated for all other grains sampled by disector. This procedure was repeated on numerous other pairs of montage serial sections (i.e., disectors) in the serial section stack, chosen at random. In this manner, the number of inter-particle contacts and sizes of about three hundred grains were measured in each specimen of 83wt%W composition.

Estimation of the First, Second, and Third Nearest Neighbor Distance Distribution of Tungsten Grains in Three-Dimensional Microstructure

First, second, third and higher order three-dimensional nearest neighbor distances can be calculated in a straightforward manner from the coordinates of the centroids of the grains contained in the stack of montage serial sections. The centroid coordinates of a grain are given by the mean of the coordinates of its top and bottom in the three-dimensional microstructure. The (X,Y,Z) coordinates of the "top" of a grain were measured by

observing the disector consisting of consecutive montage serial sections. This is done by superimposing montages of two consecutive serial sections, and marking new sections which appear in the second montage but are not present in the first montage. These new sections represent the top of the grains. Once all the tops in a montage were identified, each top coordinate was measured and then the grain belonging to that top was followed in the third dimension by looking at successive serial sections till the bottom of the grain was observed. The coordinates of the bottom were then measured. In this manner, the top and the bottom coordinates were recorded for each grain. The x and y coordinates were directly obtained from the corresponding pixel coordinates in the montage serial section, whereas the z coordinated was measured from the known distances between montage serial sections. The mean of the coordinates of the top and bottom points of a grain gave the coordinates of its centroid.

The objective was to measure all the particle centroids which were present in a volume formed by central 30 sections in a stack of 90 serial sections. There can be four types of particles which have their centroids in the central 30 sections, these are i) which are fully inside the 30 sections ii) which have their tops inside these 30 sections but bottom outside iii) which have their bottoms inside these 30 sections but tops outside, and iv) which have their both tops and bottom outside the 30 sections (see Figure 3.13).

On measuring particle centroids using disector for tops (looking for appearance of new sections) we were able to account for all the particles of type i and ii, which have their tops in the 30 sections. To account for remaining particles we need to measure centroids of

all the particles which appear in the first section of those 30 central sections. By doing this we were able to measure all the particles of type iii and iv (i.e. those which have their tops outside the 30 sections).

In this manner, the centroid coordinates of about four thousand W grains in the stack of montage serial sections were estimated, and the first, second, and higher order nearest neighbor distances were computed from these data by using a simple computer code. The three-dimensional first, second, and third nearest neighbor distance distributions were estimated from these data.

3.4.4 Measurement of Three-Dimensional Grain Size Distribution

Disector was also used to measure the calliper diameter of the particles. From the stack of ninety serial sections, the grains were sampled by disector so that they are sampled without any bias of size, etc. The calliper diameters of sampled grains were measured by displaying a false colored image of a disector (as described above) and measuring the X, Y and Z coordinates of the top of all the particles which appeared on the disector. Then each of these particles were followed in the third dimension by displaying the consecutive serial sections till the bottom of the particle was encountered. The X,Y, Z coordinates of the bottom of the particle were also measured and recorded along with the top coordinates. The calliper diameter was the difference in the Z coordinates of the top and bottom. As the tungsten grain orientations are not anisotropic, the measured caliper diameter distribution in one orientation is statistically representative of the overall caliper diameter distribution in three-dimensional microstructure. The three-dimensional grain size distributions were

measured for all specimens of 83wt%W composition.

3.4.5 Measurement of Bivariate Size-Orientation Distribution of Necks

In the present context, a neck is a triple line of contact between two abutting grains and the matrix. Orientation of a neck can be conveniently defined as the acute angle (θ) between the normal to the plane of the neck and the gravitational direction. It is not possible to accurately measure the orientation of necks by observing serial sections. In a metallographic plane, intersection between the neck and the sectioning plane can be identified by observing the two points (triple points) of intersection. The distance between a pair of triple points is the length of the chord (say r) generated by intersection of the neck with the metallographic plane. The orientation of this chord is the acute angle (α) that it forms with the gravity direction in the vertical metallographic plane. Therefore, bivariate distribution of chord lengths (r) and their orientation (α) in a vertical metallographic plane, $n_A(r,\alpha)$ can be experimentally measured. These measurements were performed in the present study. The apparent bivariate distribution $n_A(r,\alpha)$ is related to true bivariate size(X) and orientation (θ) distribution $n_V(X, \theta)$ by the following double Abelian integral equation derived by Gokhale[60], under an assumption that necks can be modeled as circles.

$$n_A(r,\alpha) = \frac{4r}{\pi \sin^2\alpha} \int_{r}^{r_m} \int_{(\pi/2)-\alpha}^{\pi/2} \frac{\cos^2\theta . \sin\theta . n_V(R,\theta) d\theta dR}{[R^2-r^2]^{1/2} [\sin^2\alpha - \cos^2\theta]^{1/2}} \qquad 3.1$$

Benes et al. [61] have developed a numerical procedure to solve this integral equation, which was used in the present study to calculate the true bivariate size-orientation

distribution of the necks from the experimental measurements performed on metallographic planes. From these distributions, the average size and number density of necks were calculated in straight forward manner.

3.5. Visualization of Three-dimensional Microstructural Volume

The volume image data presented in this research are stack of montage serial sections. The steps required to visualize these data are: data generation (stack of serial sections), pre-processing (image alignment and correction, grid regularization, image enhancement and interpolation), data classification, and finally rendering. Volume image data have been used for visualization of numerous structures and visualization can be done by either surface rendering or volume rendering. Surface rendering is defined as rendering of iso-surface of the region of interest (ROI) from the volume data, whereas volume rendering is the rendering of all the volume data by specifying color and opacity of each voxel (which is analogous to pixel in two dimensional digital image). The advantage of surface rendering is that it results in reduction of data (only surface data is retained) and is easy the understand, but has a disadvantage that lot of volume data are discarded and thus one needs to extract iso-surface data every time one changes ROI.

The data classification step for surface rendering requires fitting of a surface in the volume data. The basic idea in data classification is to look for one surface to visualize, identify the intensity corresponding to that surface and threshold the selection. One of the oldest surface rendering algorithm is contour connecting algorithm [32]. In this algorithm

Pages missing from original report.

coordination number are the fundamental data required to understand the process such as powder compaction and liquid phase sintering.

In liquid phase sintered microstructures, a correlation between size of a grain and its coordination number is likely to exist. Therefore, a bivariate frequency distribution of coordination numbers, that expresses fraction of grains having a given coordination number and having size in a certain range is of interest. To the best of author's knowledge, there have been no earlier experimental measurements (or computer simulations) of such a bivariate coordination number distribution in any microstructure. In the present work, from a stack of serial sections, grains were sampled in an unbiased manner using disector technique, and size (caliper diameter) and coordination number of each sampled tungsten grain were measured, as explained in the previous chapter. The bivariate frequency-coordination number-size frequency functions calculated from these data are shown in Figures 4.13 to 4.16 for 83 wt% W-Ni-Fe specimens liquid phase sintered for 1 min and 120 min in normal gravity and microgravity. Interestingly, there is a significant difference in the bivariate frequency functions of the specimens processed in microgravity and those processed in normal gravity for the same time. Further, in all the plots, for a given coordination number there is always one size class with highest probability of forming those many grain contacts. As the coordination number increases, the size class with highest probability also increases. Therefore, there is a strong correlation between the grain size and coordination number. To quantify this correlation, from the bivariate frequency functions, one can compute average size of the grains D_{Nc} having a specific fixed number of contacts, Nc. For the specimens

under present investigation, Figure 4.17 shows plots of D_{Nc} Vs. Nc for the four data sets. Observe that, (ii) the average size D_{Nc} having Nc number of contacts increases **monotonically** with the number of contacts, and (ii) there are significant differences in the plots for 1 minute and 120 minute specimens, but for a given LPS time, the plots for normal gravity and micro-gravity specimens are close to one another. To extract simple expression for the quantitative correlation between D_{Nc} and Nc, both the variables are normalize: D_{Nc} is divided by the experimentally measured three-dimensional global average grain size $\bar{D}$, and Nc is divided by the mean coordination number $\overline{N_c}$. The normalized plot of $[\overline{D_{Nc}^2} / \overline{D^2}]$ vs. $[N_c / \overline{N_c}]$ for all the four data sets is shown in Figure 4.18. It is observed that, (i) the plot is linear, indicating that $[\overline{D_{Nc}^2} / \overline{D^2}]$ varies linearly with $[N_c / \overline{N_c}]$, and (ii) the data points for all the specimens fall on a single straight line, whose slope is one and intercept is zero. Note that these four data sets represent specimens whose global average grain size differs by a more than a factor of two (1 min. and 120 min specimens), volume fraction of tungsten grains varies from 0.59 to 0.74, mean coordination number varies from 2.9 to 4.3, and they represent specimens processed in normal gravity and microgravity. Despite of these differences in the processing parameters, average size, amount of W grains, and mean coordination number, a single relationship describes the correlation between grain size and coordination number. This correlation can be expressed as follows.

$$\frac{\overline{D_{Nc}^2}}{\overline{D^2}} = \frac{Nc}{\overline{Nc}} \qquad 4.1$$

The surface area of the grains is directly proportional to the square of their size. Therefore, equation 4.1 implies that in a microstructure, although individual grains of different sizes may have the same coordination number, on the average, grains with larger surface area are likely to have a higher coordination number, and average surface area of the grains having a given coordination number increases linearly with the coordination number. At present there are no theories or computer simulations whose predictions can be compared with equations extracted from the experimental data.

The experimental bivariate frequency functions of coordination number and size can be converted to corresponding univariate frequency functions of coordination numbers alone, simply by integrating the bivariate functions over grain size for each coordination number. The corresponding cumulative frequency distributions of coordination numbers are reported in Figure 4.19. Observe that, (i) in the normal gravity, this distribution function varies with sintering time, and (ii) there are significant differences between the coordination number distributions in normal gravity and microgravity for a given sintering time. To determine if these differences in the cumulative frequency distribution of coordination numbers arise due to differences in the mean coordination number $\overline{N_c}$, a normalized plot of cumulative frequency of the coordination number versus the ratio $[N_c / \overline{N_c}]$ is shown in Figure 4.20. Interestingly enough, the cumulative frequency distributions of all the four specimens can be reasonably well represented by a single curve in this normalized plot. Therefore, it can be said that the effect of gravity on the univariate cumulative distribution of coordination

numbers of tungsten grains in this alloy mainly resides in its effect on the mean coordination number. The distribution itself becomes independent of sintering time and gravitational environment, once it is normalized by the mean coordination number. Thus, the gravitational effect on the cumulative frequency can be predicted simply by knowing the mean coordination number in normal gravity and microgravity.

Monte-Carlo type computer simulations have been performed[99] to compute the univariate frequency distribution of coordination numbers for an ensemble of spherical particles packed in normal gravity, under the assumptions that, (i) all the particles/grains are of the same size, (ii) the inter-particle contacts are strictly point contacts, and (iii) particles/grains have a hard-core random distribution. Figure 4.21 compares the cumulative coordination number distribution obtained from the computer simulations[99] with the present experimental data for the specimens processed in the normal gravity. There are significant differences in the computer simulated and experimental distributions. The minimum number of contacts in the simulation is three, where as the minimum number of contacts in gravity distribution is one, whereas the mean of the simulation is 5.8, where as the means of the experimental distribution are 3.7 and 4.3. Therefore, it can be concluded that these computer simulations do not represent the process of inter-particle contact formation and evolution of the contacts in the actual microstructures of tungsten grains in W-Ni-Fe alloys. The differences may be due to finite size of grain contacts (i.e., necks), and the presence of size distribution of grains in the actual microstructure.

4.3.2 Mean Coordination Number of Grains in Three-Dimensional Microstructures

The mean coordination number of grains can be computed from the experimentally measured coordination number distributions in a straightforward manner. Table 4.1 gives the mean coordination numbers of tungsten grains in the specimens of liquid phase sintered 83wt%W-Ni-Fe alloy under investigation. Note that, (i) the mean coordination number in the microgravity environment is significantly lower than that for the specimens preceded in normal gravity, at both low and high sintering times, (ii) the mean coordination of the tungsten grains for the specimens processed in microgravity appears to be insensitive to the sintering time. The higher mean coordination number for gravity specimens may be partly due to gravitational settling leading to more dense packing of the grains. There have been many observations which show that if the density difference between the solid grains and the liquid is high, the resulting coordination number is also high[98].This difference in the coordination number can be attributed to the pressure exerted by the solid grains on each other. For the specimens processed in normal gravity, this phenomena also results in a systematic increase in the coordination number along the gravity direction (because the grains at the bottom of the specimen experience higher pressure then those at the top). The variation in coordination number with the distance from the top of the specimen has been modeled by Liu et al.[98] assuming that the three dimensional packing coordination number Nc is proportional to the gravitational pressure. Liu et al.[98] have given the following relationship.

$$Nc(H) = Nc_0 + C_0\, g\, (\rho_s-\rho_l)L\, A(H) \qquad 4.2$$

where Nc(H) is the 3D coordination number at non-dimensional distance H from the top (H is non -dimensionalized by the total height of the specimen L), g is the gravitational acceleration ρ_s and ρ_l are the density of solid and liquid, L is the total height of the specimen and A(H) is the ratio of the solid volume which is above this location to the total volume of the specimen. The Nc_0 is the lower limit of packing coordination at the top of the solid settled region, and C_0 is the constant of proportionality. In the present study, the mean coordination number was not measured at different depths for the specimens processed in normal gravity, and therefore, it is not possible to verify equation 4.2 derived by Liu et al [98]. However, the present data are sufficient to calculate the two parameters N_{c0} and C_0. For microgravity environment, g is zero (for all practical purposes). Substituting g=0 in equation 4.2 yields that N_{c0} is also equal to the coordination number of grains in the microgravity. Therefore, N_{c0} is equal to 2.9. In the normal gravity, the coordination number was measured in the region almost at the bottom of the specimens, for which in equation 4.2 , H=1. At this location, A(H) is exactly equal to overall solid volume fraction in the specimen. Therefore, using the experimental mean coordination number data for normal gravity specimens, one can compute the constant C_0 in equation 4. The calculated values of C_0 for the two gravity specimens (83 wt% 1 minute and 83 wt% 120 minute) along with the value computed by Liu et al. is given in Table 4.2. The value computed by Liu et al. is for W-Ni system (and not for W-Ni-Fe) system, and it differs from the C_0 values computed from the present experimental data. Therefore, it may be said that the parameter C_0 is sensitive to the alloy composition.

A number of theories and simulations reported in the literature[99,100] attempt to predict the mean coordination number of grains in sintered microstructures. In the past, these predictions could not be validated due to lack of experimental data on mean coordination number of grains in three-dimensional sintered microstructures. Therefore, it is of interest to compare the present experimental data with the theoretical predictions.

4.3.3 Estimation of Three-Dimensional Mean Coordination Number From Measurements Performed on Two-Dimensional Metallographic Planes

The size of a stable neck is governed by the size of the contacting grains and the dihedral angle ϕ for that interface. Assuming spherical grains, a derivation for relating mean 2D coordination number to mean 3D coordination number can be made as follows. Spherical grains will result in formation of circular necks. The number density of the grains per unit volume is related to number density in a cross-sectional area according to the following stereological relationship[59]:

$$(Nv)_G = (N_A)_G / \bar{D} \qquad 4.3$$

where $\bar{D}$ is the mean calliper diameter of the grains. The number density of necks in a cross-sectional area is equal to one-fourth the length of the neck perimeter per unit volume L_v^{exp} [59] as given below:

$$(N_A)_N = L_v^{exp} / 4 \qquad 4.4$$

and $L_v^{exp} = \pi X (Nv)_N$, 4.5

where X is the mean diameter of the necks. Substituting the value of L_v^{exp} from equation 4.5 in equation 4.4 and taking the ratio of equation 4.3 and equation 4.4 we get:

$$\frac{(N_A)_G}{(N_A)_N} = \frac{\pi}{4}\frac{(N_V)_G}{(N_V)_N}\frac{\overline{X}}{\overline{D}} \qquad 4.6$$

Substituting Cg and Nc from equation 4.1 and 4.2 we get:

$$Cg = Nc\frac{\pi}{4}\frac{\overline{X}}{\overline{D}} \qquad 4.7$$

For a mono-sized distribution of grains the ratio of mean neck size to mean grain size (X/D) is equal to $\sin(\phi/2)$ (see section 2.3.2). This leads to the following relation:

$$Cg = 0.785\ Nc \sin(\phi/2) \qquad 4.8a$$

This relation is an exact relation for an ensemble of mono-sized spherical grains. However, this result is not well known in LPS community. In a similar attempt German[73] performed

computer simulations to relate mean 2D coordination number to mean 3D coordination number and fitted the following empirical relation:

$$Cg = 0.8\ Nc \sin(\phi/2) \qquad 4.8b$$

Therefore, there is an excellent agreement between the results of computer simulations and the analytical equation, as both are based on the same model assumptions.

In liquid phase sintered microstructures, a range of grain sizes usually exists. This complicates the relationship between the size of neck X formed by grains of diameters D_1 and D_2. This relationship is as follows:

$$X = \frac{D_1 D_2 \sin(\phi)}{\sqrt{(2D_1 D_2 \cos(\phi) + D_1^{\,2} + D_2^{\,2}}} \qquad 4.9$$

Let the ratio D_2/D_1 be f, then a value of $f = 1$ would correspond to the assumption of mono-sized spheres, resulting in $X/D = \sin(\phi/2)$. For any other value of f the value of X/D will be different than $\sin(\phi/2)$. Therefore to express X/D for a poly dispersed system considerable additional information is needed. It is necessary to know the three-dimensional size distribution of grains, the correlation between the sizes of the grains and the coordination number, and the pair correlation of the sizes of the two contacting grains. It is very possible

that the pair correlation of the sizes of the two contacting grains is such that large grains are always surrounded by small grains. Therefore, for a poly-dispersed ensemble of spherical grains it is not possible to derive a general relationship between two-dimensional and three-dimensional mean coordination numbers.

The mean coordination number of grains is equal to two times the ratio of the number density of necks in three-dimensions to the number density of grains. If it is assumed that the grains have a spherical shape, then the three-dimensional distribution of the grain sizes can be estimated from the corresponding two-dimensional distribution measured in a metallographic plane by using the well-known Saltykov's unfolding procedure[59], and then the number of grains per unit volume, $(N_V)_G$ can be calculated in a straightforward manner. Similarly, if it assumed that the necks have a circular shape, then the three-dimensional bivariate distribution of neck size and orientation can be estimated from experimentally measured apparent bivariate distribution of neck trace size and orientations in the vertical metallographic plane by using the stereological unfolding procedure developed by Gokhale [60,61]. The number density of necks $(Nv)_N$ can be then computed from the three-dimensional size and orientation distribution of necks. The coordination number Nc can then be calculated from the ratio of the number density of necks to the number density of grains using equation. The problem with this technique is that it requires two shape assumptions and involves complex numerical solutions. This leads to error propagation in the calculated values of the number densities. Thus the ratio of number densities (and hence, the mean coordination number) obtained in this manner is expected to have a significant random error

and bias, which is not acceptable for detecting small variations in the mean coordination number. It must be concluded that sampling of **three-dimensional** microstructure is essential to reliably estimate the mean coordination number. If the mean coordination number is the only parameter of interest (rather than distribution of coordination number), then it can be efficiently estimated by measuring number density of grains and number density of necks in three-dimensional microstructure by using montage disector sampling; are large number of serial sections or reconstruction of large volume of three-dimensional microstructure is not necessary for this purpose.

4.3.3 Evolution of First, Second, and Third Nearest Neighbor Distribution of Grains

Another way, apart from coordination umber, of describing short range spatial arrangement is through nearest neighbor distribution functions. The n^{th} nearest-neighbor distribution function $P_n(r)$ is such that $P_n(r).dr$ is the probability of finding the centroid of n^{th} nearest neighbor in a spherical shell of radius r to r+dr from another particle centroid. Unlike coordination number (cardinality) which

is a zero dimensional geometric characteristic, the nearest-neighbor distribution function are one dimensional geometric characteristic which also gives the scale of the microstructure. The information on grain centroids of about 3000 particles was extracted in 3D and used to calculate the 1^{st} 2^{nd} and 3^{rd} nearest-neighbor distribution functions in 3D. The 1^{st} ,2^{nd} and 3^{rd} nearest neighbor distribution function in 3D for all the four specimens of 83 wt% are plotted in Figures 4.22 to 4.25. The higher order nearest neighbor distribution function (2^{nd} , 3^{rd} and higher) are expected to be less accurate because of limited sampling and the edge effect of

finite volume.

The 1st nearest neighbor distribution of all the specimens was normalized by their corresponding mean 3D grain size and are plotted in Figure 4.26. It can be seen that all the 1st nearest neighbor distance distributions superimpose each other on the normalized plot. This should not be a surprise, because it was observed in the previous section on coordination number, that all the particles both in gravity and microgravity are touching at least one other particle. Hence, the first nearest-neighbor functions are only a mean diameter away. Similar normalized curves were plotted for the 2nd and 3rd nearest neighbor distribution functions. The normalized 2nd nearest neighbor distribution functions also superimpose suggesting that even the second nearest neighbor functions are just a scale factor change. This is expected because the data on coordination number show that about 90% of the particles have two or more grain contacts. The normalized 3rd nearest neighbor distribution function shows a good match between the 1 minute microgravity and gravity cases and the 120 minute gravity case. However, the 120 minute microgravity case plot does not match the other three curves. This may be attributed to the value of mean number of contacts per grain in this case (2.9), which is slightly lesser than 3, however it may be due to inadequate sampling.

4.3.4 Evolution of Radial Distribution Function of Tungsten Grains

Radial distribution function describes the short range, intermediate range, and long range spatial arrangement of grain centers in three-dimensional space. Therefore, it gives an overall view of the spatial arrangement of grains in one distribution function. In general, the

radial distribution function cannot be estimated from any measurements performed on the two-dimensional metallographic planes. In the present investigation, to quantify the spatial arrangement of grains in the three-dimensional microstructure, the grain centroids for about 3000 grains have been measured in three-dimensions from volume of the microstructure reconstructed from ninety montage serial sections. These data on the grain centroids are sufficient for the estimation of the three-dimensional nearest neighbor distributions. However, these data are not sufficient for reliable estimation of the radial distribution function in three-dimensional microstructure. To estimate the radial distribution function, at each value of the radial distance r, it is necessary to count (and average over) the number of grain centroids and average it over about one thousand reference grains. For reliable estimation of the radial distribution function for the radial distances up to eight grain diameters, to minimize the edge effects, a twenty diameter thick stack of serial sections is necessary, which translates to about six-hundred montage serial sections for the specimens liquid phase sintered for 120 minutes. Therefore, it is not practically feasible to estimate the three-dimensional radial distribution function of tungsten grains in the present alloy system from serial sections. However, the radial distribution function of the grain sections observed in two-dimensional metallographic planes can be reliably estimated, and these data are discussed below.

Metallographic sections of the 83wt%W-Ni-Fe alloy specimens were analyzed and radial distribution functions were generated. Figure 4.27 represents the radial distribution function for the specimens processed in the normal gravity for 1 minute and 120 minutes. In

this plot, the radial distance has been normalized by the corresponding two-dimensional mean grain section sizes. These two normalized radial distribution functions almost superimpose on each other. This indicates that the normalized radial distribution function is time invariant. Therefore, the spatial arrangement of grains at higher sintering time is similar to that at the lower time, except for the scale change. A similar normalized radial distribution plot for the corresponding specimens liquid phase sintered in microgravity is shown in Figure 4.28. Note that, in this plot, the curves for one minute and 120 minute specimens do not superimpose. Therefore, the normalized spatial arrangement of the tungsten grain sections in a metallographic plane does not appear to have reached a time invariant form. The radial distribution function observed in a metallographic plane depends on both the radial distribution function of grains in three-dimensional space and the grain size distribution. Therefore, it is likely that in these specimens, the normalized three-dimensional radial distribution function and/or normalized three-dimensional grain size distributions have not reached time invariant forms. It will be shown in the next section that in the specimens liquid phase sintered in microgravity, the normalized three-dimensional grain size distribution is not time invariant.

4.4 Evolution of Three-dimensional Grain Size Distribution

During liquid phase sintering, the grain size distribution evolves with time. Theories of LPS predict the temporal evolution of the grain size distribution function. All the theories predict that the grains size distribution reaches a specific time-invariant functional form,

when normalized with an appropriate measure of the length scale of the microstructure (for example, average grain size). However, different theories predict different functional forms for the normalized time invariant grain size frequency function. Therefore, liquid phase sintering theories can be verified by comparing the experimental three-dimensional grain size distributions with the corresponding theoretical predictions. In most of the earlier investigations, such comparisons have been made by using experimentally measured two-dimensional grain size distributions, or three-dimensional grain size distributions estimated from corresponding two-dimensional grain size distributions by using stereological unfolding procedures that are based on specific shape assumptions. The stereological unfolding procedures for estimation of size distributions involve complex numerical calculations. These calculations invariably result in the significant amplification of the errors present in the raw data, i.e., the errors in the computed three-dimensional distribution are significantly higher than those in the raw data, and in most of the cases, they are unknown. In addition, the unfolding procedures may also introduce bias (of unknown extent) in the estimated three-dimensional distributions, if the shape assumptions are not valid. In the earlier studies, the comparison between experimental and theoretically predicted size distributions were not based on any rigorous statistical tests of hypothesis: in almost all the cases, the conclusions were drawn by "just looking at the two size distributions". In the present study, three-dimensional grain size distributions have been directly measured from the stacks of montage serial sections, without involving restrictive shape assumptions or any complex data processing that can amplify the statistical errors. Therefore, it is of interest to compare the

experimentally measured three-dimensional grain size distributions with the theoretical predictions by using rigorous statistical tests. Figures 4.29 and 4.30 show the experimentally measured three-dimensional grain size distributions of the 83wt%W-Ni-Fe alloy liquid phase sintered in normal gravity and microgravity. The three-dimensional sizes of about 1500 to 2000 grains were measured in the montage serial section stacks of each specimen to obtain these size distributions. Figures 4.31 and 4.32 show the corresponding normalized frequency distributions, obtained by dividing each grain size by the global average grain size. Statistical χ^2 test was performed on the normalized grain size distributions to answer the following questions:

1. Do the normalized grain size distributions match with those predicted by any of the theoretical models?

2. Are normalized grain size distributions of specimens processed in normal gravity for 1 minute and 120 minutes statistically similar?, i.e., has the size distribution achieved pseudo-static state?

3. Are the normalized grain size distributions of the specimens processed in microgravity for 1 minute and 120 minutes statistically similar?

4. For 83wt% W-Ni-Fe alloy specimens liquid phase sintered in normal gravity and microgravity for the same time, are there any systematic differences in the normalized grain size distributions?

The χ^2 test was used to compare normalized experimental grain size distributions with the size distribution predicted by classical LSW [36,37] theory, BW [41] model, BWEM

[43,44] model, and communicating neighbors model by DeHoff[47]. The experimental size distributions were first cast into a histogram format representing normalized grain size distribution function. The predicted number of grains in each size class was computed for each model. Those size classes which had less than 5 grains were combined with the adjacent class. The chi-squared value was computed for each comparison. The χ^2 test clearly showed that **size distributions predicted by ALL the models are statistically different from the experimental size distributions**. This may be due to the fact that models assume discrete individual particles, whereas sintered microstructure contains connected network of grains, or because of very high volume fraction of grains in liquid phase sintered microstructures under present investigation.

The χ^2 test performed on the grain size distributions of the specimens processed in normal gravity for 1 minute and 120 minutes revealed that the normalized grain size distribution of these specimens are statistically similar. It may be concluded that these grain size distributions have reached a time invariant asymptotic state, but its functional form is different from those predicted by the theoretical models. However, the χ^2 test performed on the specimens processed in microgravity for 1 minute and 120 minutes revealed that the normalized grain size distribution of these specimens are statistically different. It may be concluded that, in these specimens processed in microgravity, the normalized grain size distribution has not achieved a time invariant pseudo-static state. Therefore, in microgravity, the path of evolution of the grains size distribution is different from that in the normal gravity.

The χ^2 test performed on the grain size distributions of the specimens liquid phase sintered normal gravity and microgravity for one minute revealed that the grain size distribution of these specimens are statistically different. The χ^2 test on the corresponding pair of specimens liquid phase sintered for 120 minutes also revealed the same thing. Therefore, the reduced gravity (or microgravity) does affect the grain size distribution, as well as the path of evolution of the grain size distribution in the liquid phase sintered microstructures of W-Ni-Fe alloy under investigation.

The evolution of grain size distribution function, radial distribution function and NND function in the samples sintered in gravity environment show only a scale factor change. This is not seen in the evolution of these functions in the samples sintered in microgravity environment. This is one **major difference** in the evolution of microstructure during LPS in gravity and microgravity.

4.5 Effect of Gravity on the Kinetics of Liquid Phase Sintering

The kinetics of LPS are usually described in terms of changes in the average grain size. However, other measures of the scale of the structure can be also used to monitor the kinetics. In this research, three-dimensional average grain size, arithmetic average grain volume, and volume weighted average grain volume, and number density of grains have been experimentally measured in the liquid phase sintered 83wt%W-Ni-Fe specimens by using unbiased and assumption-free procedures involving combinations of stereological techniques, montage serial sectioning, three-dimensional microstructural reconstruction, and

large area high resolution disector. Note that all the specimens have exactly the same shape and size, and all measurements were performed in the region at a distance of 1.5 mm from the bottom of the specimen. Table 4.3 lists the measured microstructural parameters. For the two specimens liquid phase sintered for one minute in gravity and microgravity, **ALL** the process parameters were identical, except the gravitational environment. Inspection of Table-I shows that for the specimen liquid phase sintered in the normal gravity for one minute, the arithmetic average grain volume is **100% larger**, volume weighted average grain volume is **92% larger**, and average three-dimensional grain size is **30% larger** than the identical specimen processed in the microgravity environment for exactly the same time. The only difference in these two specimens is their gravitational environment. Comparison of the same microstructural parameters for the specimens liquid phase sintered for 120 minutes shows that arithmetic average grain volume, volume weighted average grain volume, and three-dimensional average grain size for the specimen processed in normal gravity are marginally higher than that for the specimen processed in normal gravity. Therefore, it can be concluded that the absence of gravity (strictly speaking, microgravity) slows the kinetics of the liquid phase sintering process. These gravitational effects on the kinetics are particularly significant at small sintering times.

On the basis of two-dimensional microstructural measurements, German and co-workers[50] concluded that kinetics of the liquid phase sintering process are slower in microgravity environment. The present unbiased three-dimensional microstructural data lead to the same conclusion.

As mentioned in Chapter II, data on volume weighted average volume can be used to estimate the variance and coefficient of variation (CV) of the distribution of grain volume without involving any assumption concerning microstructural geometry. Table 4.4 reports the calculated variance and CV^2 of the tungsten grain volume distributions in microstructures 83wt%-Ni-Fe alloy specimens liquid phase sintered in normal gravity and microgravity. Note that the variance and CV^2 values for the specimen processed in microgravity are **lower than the values for the corresponding specimens processed in normal gravity**. Therefore, reduced gravity leads to narrower grain volume distributions.

During liquid phase sintering, grain coalescence and grain coarsening are the two processes that lead to increase in the average grain size. The process of grain coalescence involves two contacting grains of dissimilar size merging into one by directional grain growth of one, whereas the grain coarsening process is essentially similar to particle coarsening. The grain coalescence process is expected to contribute significantly to the increase in the grain size at small sintering times, where as grain coarsening dominates at the large sintering times. The measured average grain size (average grain volume) reflect overall increase in the scale of the structure due to contributions from both of these phenomena. Gravity is expected to affect both grain coalescence and grain coarsening: reduced gravity is expected to slow down both of these processes.

The experimental data show that at small sintering times (one minute), the average grain volume, average size of tungsten grains etc. in the specimen processed in the normal gravity are significantly larger than those in the corresponding specimen processed in the

microgravity environment for one minute. These differences are due to the effect of gravity on the grain coalescence process that dominates at short times. There is no quantitative theory of grain coalescence that predicts the increase in the grain size with time due to grain coalescence alone. Coalescence requires contacts between large grains and very small grains. Larger the coordination number, larger is the number of larger grains in contact with very small grains, and consequently higher is the extent of grain coalescence. Recall that the mean coordination number of the specimens processed in normal gravity is significantly larger than the corresponding specimens processed in microgravity. Therefore, the specimen processed in normal gravity is expected to experience more grain coalescence (and therefore, larger grain size) than the one processed in microgravity, simply due to these gravity induced differences in the spatial arrangement of grains. This explains the observed larger grain size of specimen processed in normal gravity for one minute as compared to the corresponding specimen processed in microgravity.

As mentioned earlier, at large sintering times, classical grain/particle coarsening essentially governs the kinetics of liquid phase sintering. Theories of kinetics of grain coarsening are reasonably well developed[36-47]. Although the theoretically predicted grain size distributions differ from those measured experimentally (see Section 4.4), there is a general agreement that during the grain coarsening, the time (t) dependence of the average grain size D can be expressed in terms of a simple power law:

$$D^n - D^n_0 = K\,t \qquad 4.10$$

where K is the grain growth constant, the exponent n is a constant depending upon the growth mechanism, D_0 is the initial particle size (usually taken as zero because at the start of liquid formation all the powder particles are fragmented to single crystal grains which are of the order of 1mm), and D is the grain size at time *t*. The value of exponent n has been found to be about three for most of the studies on the tungsten heavy alloys [100-103]. Almost all the theories (in spite of other differences) predict the value of exponent n = 3 for diffusion controlled growth. In equation 4.10, the rate constant K may be affected by gravity due to two different reasons. Gravity causes solid-liquid separation, and results in microstructural gradients in the specimens liquid phase sintered in the normal gravity (see Table 4.3 for variation in volume fraction with location). As a result of solid liquid separation the volume fraction of solid in the specimens processed in normal gravity specimens is **highe**r than that in the same location of corresponding specimen microgravity. The higher volume fraction of grains in turn decreases the diffusional distances, and leads to an increase in the rate of grain coarsening. Recently German [50] has pointed out another effect of gravity that leads to increase in the rate of coarsening. The driving force for coarsening is the differences in curvatures of solid particles which results in differences in solubility causing diffusional mass transport. The differences in solubility can also be caused by the differences in the stress state of the particles. German et al. showed that the solubility increase due to stress exerted by particles on top of each other at the bottom of a 10 mm specimen will be 4% over that due to curvature (for particles of 10 μm size). This increase in solubility is very small but it was predicted that this will result in large grain size

difference at long times. Based on these concepts, German et al[50] have derived an equation for the kinetic rate constant K, that accounts for both volume fraction and gravitational pressure effects. Based on this model one can predict the mean size as a function of time for both gravity and microgravity, when grain coalescence is negligible (i.e. at high sintering times). For the alloy under present investigation, this model predictions average grain sizes of 26.2 μm and 29.5 μm after 120 minutes of LPS for samples sintered in microgravity and gravity, which amounts to a difference of 35% in mean grain volume and 12% in mean grain size. However, the observed differences in the mean grain volume of the specimens processed in normal gravity and microgravity for 120 minutes are much lower than this estimate and the mean grain size are almost similar. This discrepancy may be due to the errors in the auxiliary data (surface energy, diffusion coefficient, etc.) used for calculation of grain size differences using German et al. model. Experiments in microgravity and normal gravity environments for much longer sintering times may confirm the differences in the grain sizes due to gravitational effects predicted by German et al. model.

4.6 Effect of Gravity on Densification During Liquid Phase Sintering

Densification is well-established phenomena in the liquid phase sintered microstructures, when the specimens are processed in normal gravity. It is well documented that the volume fraction of the grains at a given location in the specimen increases with time during the liquid phase sintering process [7,100]. It must be pointed out that densification is different from the initial gravitational settling. The densification continues after a stable

and rigid interconnected grain structure is formed, at which point the gravitational settling ceases. Densification involves pulling together of the skeleton of the network of interconnected grains, leading to an increase in solid volume fraction with time at any location in the specimen. Densification is attributed to a combined effect of settling of extricated particles from a skeleton [106] and grain shape accommodation [105] resulting from an increase in solubility due to gravitational stresses [50]. This suggests that densification should occur only in gravity and not in microgravity. Table 4.3 shows the volume fraction of tungsten grains at two locations at two different sintering times for the specimens of 78wt% and 83wt% W-Ni-Fe alloys liquid phase sintered in normal gravity and microgravity. Observe that for the specimens processed in the normal gravity, at a given location, the volume fraction of W grains is somewhat higher at 120minutes than that at one minute. These differences are observed at both top and bottom locations of the specimens of both the compositions processed in the normal gravity, indicating the densification of grains, which is quite expected. However, there is no increase in the volume fraction of W grains with time at a given location in the specimens processed in microgravity for specimens of all the three compositions: there is no densification in microgravity. This observation agrees with the expected trends as suggested by previously described theories on densification [105,106]. However this is for the first time that it has been experimentally shown that no densification occurs micro-gravity.

CHAPTER V

CONCLUSIONS AND SCOPE FOR FUTURE WORK

The purpose of this research to quantitatively characterize the effect of gravity on the microstructural evolution during liquid phase sintering process was successfully completed. Some of the important techniques developed in the course of this research were, image analysis procedure to automatically measure volume-weighted average volume, montage based efficient serial sectioning technique, large volume high resolution three-dimensional microstructural reconstruction, and unbiased estimation of three-dimensional coordination number and grain size distribution from a stack of serial sections. In addition, numerous computer codes were written to extract descriptors of spatial arrangement of grains from the raw image analysis data. There are consistent differences in the microstructural attributes of the specimens sintered in microgravity from the corresponding gravity specimens. This is seen in the spatial arrangements of tungsten grains, mean number of inter-particle contacts, mean grain sizes and its distribution, and number density. The following are the main conclusions of this research:

5.1 Effect of Gravity on the Evolution of Spatial Arrangement

3D coordination numbers

a) In specimens processed in both gravity and microgravity environment there are

practically no isolated grains "floating around" in the matrix. This is expected in gravity where the grains have to contact each other to provide normal force to balance gravity, but it is quite surprising to see this in microgravity.

b) At a given sintering time, the coordination number in microgravity is significantly lower than that in gravity.

c) In microgravity, the coordination number remains constant whereas in gravity, it increases with time. This increase is attributed to grain shape accommodation.

d) There exists a strong correlation between the coordination number and the mean surface area of grains forming that coordination. This can be expressed as follows:

$$\frac{\overline{D_{Nc}^2}}{\overline{D^2}} = \frac{Nc}{\overline{Nc}}$$

where $\overline{D_i^2}$ is the mean of square of the sizes of the grains which form *i* contacts, Nc is the mean coordination number, and $\overline{D^2}$ is the mean of the square of the whole size distribution.

Nearest neighbor distribution function

a) In spite of significant differences between the volume fractions of gravity and microgravity samples (and even larger differences in the values of mean free path), the 1st and 2nd 3D nearest neighbor distances are only a scale change, with the scale factor being the mean grain size

5.2 Effect of gravity on kinetics

a) In the initial stages (until approximately 1 minute), the kinetics of grain growth is slower in microgravity than in gravity environment resulting in a significant difference in the grain sizes. However, the difference in grain size after 120 minutes of sintering becomes insignificant.

b) The observed difference in rates of grain growth at lower times (upto 1 minute) is attributed to the effect of coalescence.

5.3 Effect of gravity on densification

a) There is **no** densification with time in microgravity though this effect is seen in gravity.

b) The densification in gravity is attributed to settling of extricated particles, and grain shape accommodation, which is also responsible for increase in coordination numbers with time.

5.4 Effect of gravity on the evolution of grain size distribution

a) The observed grain size distributions do not match most theoretical models, including classical LSW model, BW model, BWEM model and DeHoff's Communicating Neighbor model.

b) The size distributions for gravity samples show only a scale change, whereas those for microgravity do not.

The implications of this work for future research in this area are significant. The large

volume 3D reconstruction can be utilized to directly perform numerical simulations on the true microstructure. Future LPS experiments can be designed with single crystal particles with bivariate size distributions to study the kinetics of late stage grain growth. Since the major differences found in this research were in the one minute case, it would be helpful to perform some experiments in microgravity on samples which have been first sintered for one minute on earth. Finally, experiments with different pre-sintering conditions can be performed to study the effect of microgravity on pre-sintering.

REFERENCES

1. V.N. Eremenko, Y.V. Naidich, and I.A. Lavrinenko, *Liquid Phase Sintering*, Consultants Bureau, New York, NY, 1970.

2. J.S. Hirschhorn, *Introduction to powder metallurgy*, American Powder Metallurgy Institute, New York, NY, 1969.

3. R.M. German, *Liquid Phase Sintering*, Plenum Press, New York, NY, 1985.

4. H.S. Nayar: *Modern developments in Powder metallurgy*, H.H. Hausner and P.W. Taubenblat, eds., Metal Powder Industries Fedration, Princeton, NJ, vol 11, pp 109-41, 1977.

5. S.C. Hardy and P.W. Voorhees, *Ostwald ripening in a system with a high volume fraction of coarsening phase*, Metallurgical Transactions A, vol 19A , pp 2713-21, 1988.

6. W.E. Gurwell, *Heavy Metal Alloys Containing 30% to 90% Tungsten*, Progress in Powder Metallurgy, vol 41, pp 327- 46, 1985.

7. S.C. Yang and R.M. German, *Gravitational limit of particle volume fraction in liquid-phase sintering*, Metallurgical Transactions A, vol 22A, pp 786 - 91, 1991.

8. R.G. Iacocca, R.M. Greman, *Experimental design for liquid phase sintering in microgravity*, Ad. Pow. Met., Metal Powder Industries Fedration, Princeton, NJ, vol 2, pp 181-94, 1993.

9. L.B. Ekbom and A. Eliasson, Modern Developments in Powder Metallurgy, vol 19, eds., PU Gummeson and D.A. Gustafson, Princeton, pp 63-73, 1988.

10. L.B. Ekbom, *Results from the melting of tungsten composites under microgravity in space (Texus 10 flight)*, Inter J. Refract. Hard Mater.,vol 6, pp 231-232, 1987.

11. L.B. Ekbom and A. Eliasson, Adv. Space res., vol 8, pp 315-, 1988.

12. L.B. Ekbom, H. Fredriksson, and A. Eliasson, *Liquid-phase sintering of tungsten composites in space. Agglomerate separation and particle growth*, High Temperatures High Pressures, vol 21, pp 507-514, 1989.

13. S. Kohara, *Study on Liquid Phase Sintering*, Science University of Tokyo, Tokyo,

Japan, May 1994.

14. F.Aldinger, *Controlled porosity by an extreme kirkendall effect*, Acta Met., vol 22, pp 923-928, 1974.

15. L. Froschauer and R.M. Fulrath, *Direct observation of liquid phase sintering in the system Tungsten Carbide-cobalt*, J.Maters. Sci., vol 11, pp 142-149,1976.

16. O.J. Kwon and D.N. Yoon, *The liquid phase sintering of W-Ni, Sintering Processes*, ed. G.C. Kuczynski, Plenum Press, New York, NY, pp 203-218, 1980.

17. W.J. Huppmann and G. Petzow, *The elementary mechanisms of Liquid Phase sintering, Sintering Processes*, ed. G.C. Kuczynski, Plenum Press, New York, NY, pp 189-201, 1980.

18. S.R. Jurewicz and E.B. Watson, *Distribution of partial melt in a Felsic system: importance if surface energy*, Contrib. Mineral. Pwtrol., vol 85, pp 25-29, 1984.

19. J.W. Cahn and R.B. Heady, *Analysis of capillary force in Liquid Phase sintering of Jagged particles*, J. Amer. Ceramic Soc., vol 53, pp 406-409, 1970.

20. W.J. Huppmann, *The elemintary mechanisms of Liquid Phase sintering, 2. Solution Reprecipitation*, Z. Metallkde., vol 70, pp 792-797, 1979.

21. W.D. Kingery, *Densification during sintering in the presence of a Liquid Phase. I* Theory, J. Appl. Phys., vol 30, pp 301-306, 1959.

22. D.N. Yoon and W.J. Huppmann, *Grain Growth and densification during Liquid Phase sintering of W-Ni*, Acta Met., vol 27, pp693-698, 1979.

23. G.H. Gessinger, H.F. Fischmeister, *A Model for the sintering of Tungsten with Nickel additions*, J. Less-common Metals, vol 27, pp 129-141, 1972.

24. G.H. Gessinger, H.F. Fischmeister and H.L. Lukas, *A model for second -stage Liquid Phase sintering with a partially wetting liquid*, Acta Met., vol 21, pp 715-724, 1973.

25. S. Takajo, W.A. Kaysser and G. Peetzow, *Analysis of particle growth by Coalescence During Liquid Phase sintering*, Acta Met., vol 32, pp 107-113, 1984.

26. T.H. Courtney and J.K. Lee, *An analysis for estimating the proprability of particle coalescence in Liquid Phase sintering systems*, Metall. Trans. A , vol 11A, pp 943-

947, 1980.

27. S.J.L. Kang, W.A. Kaysser, G. Petzow, and D.N. Yoon, *Elimination of pores during liquid phase sintering of Mo-Ni*, Powder Met., vol 27, pp 97-100, 1984.

28. M.P. Anderson, D.J. Srolovitz, G.S. Grest, and P.S. Sahni, *Computer simulation of grain growth -I Kinetics*, Acta Met., vol 32, pp 783-791, 1984.

29. P.W. Voorhees, *Ostwal Ripening in Two phase mixtures*, PhD. Thesis, Rensselaer Polytechnic Institute, Troy, NY 1982.

30. P.W. Voorhees and M.E. Glicksman, *Solution to the multi-particle diffusion problem with application to ostwald ripening - I Theory*, Acta Met., vol 32, pp 2001-2011, 1984.

31. P.W. Voorhees and M.E. Glicksman, *Solution to the multi-particle diffusion problem with application to ostwald ripening - II Computer simulation*, Acta Met., vol 32, pp 2013-2030, 1984.

32. W.W. Mullins, in Metal Surfaces, vol 17, American Society for Metals, 1962.

33. W.Ostwald, Z. Phys. Chem., vol 37, pp 385, 1901.

34. G.W. Greenwood, *Growth of dispersed precipitates in solutions*, Acta Metallurgica, vol 4, pp 243-248, 1956.

35. W.D. Kingery, *Densification during sintering in the presence of a liquid phase - II*, J. Applied Physics, vol 30, no 3, pp 301-310, 1959.

36. I.M. Lifshitz and V.V. Slyozov, *The kinetics of precipitation from supersaturated solid solutions*, J. Phys. Chem. Solids, vol 19, no 1, pp 35-50, 1961.

37. C. Wagner, *Theorie der Alterung von Niederschlagen durch Umlosen*, Z. Elektrochemie, vol 65, no 7, pp 581-591, 1961.

38. P.W. Voorhees, *The Theory of Ostwald Ripening*, Journal of Statistical Physics, vol 38, no 1, pp 231-252, 1985.

39. A.J. Ardell, *The effect of volume fraction on particle coarsening: Theoretical Considerations*, Acta Metallurgica, vol 20, pp 61-71, 1972.

40. A.J. Ardell, *On the coarsening of grain boundary precipitates*, Acta Metallurgica,

vol 20, pp 601-609, 1972.

41. A.D. Brailsford and P. Wynblatt, *The dependence of Ostwald Ripening kinetics on particle volume fraction*, Acta Metallurgica, vol 27, pp 489-497, 1979.

42. C.K.L. Davies, P. Nash and R.N. Stevens, *The effect of volume fraction of precipitate on Ostwald ripening*, Acta Metallurgica, vol 28, pp 179-189, 1980.

43. C.S. Jayanth and P. Nash, *Review: Factors affecting particle coarsening kinetics and size distribution*, J. of Materials Sc., vol 24, pp 3041-3052, 1989.

44. C.S. Jayanth and P. Nash, *Experimental evaluation of particle coarsening theories*, The Institute of Metals, pp 405-413, 1990.

45. J.A. Marqusee and J. Ross, J. Chem. Phys, vol 80, pp 536, 1984.

46. M. Tokuyama and K.Kawasaki, Physica, vol 123A, pp 386, 1984.

47. R.T. DeHoff, *Geometrically general theory of diffusion controlled coarsening*, Acta Metall., vol 39, pp 2349-60, 1991.

48. W.W. Mullins and J. Vinals, *Self-similarity and grain growth kinetics driven by surface free energy reduction*, Acta Metall, vol 37, no 4, pp 991-997, 1989.

49. R.T. DeHoff, Metall. Trans., vol 2, pp 521-26, 1971.

50. German, R.M.; Yixiong Liu; Griffo, A., Metallurgical and Materials Transactions A, vol 28A, no1,pp 215-21, 1997.

51. Yixiong Liu; German, R.M, Acta Materialia ,vol 44, no 4, pp1657-63 , 1996.

52. Yixiong Liu; Iacocca, R.G.; Johnson, J.L.; German, R.M.; Kohara, S., Metallurgical and Materials Transactions A (Physical Metallurgy and Materials, vol 26A, no 9, pp 2484-6, 1995.

53. German, R.M.; Yixiong Liu, Journal of Materials Synthesis and Processing,vol 4, no 1, pp 23-34 , 1996.

54. Xue, Z.; Noojin, S.L.; Vandegrift, J.G.; Kuruvilla, A.K.; Smith, J.E, High Temperatures - High Pressures.,vol 29, no 3, pp 349-57, 1997.

55. Vandegrift, J.G.; Noojin, S.L.; Ryan, K.; Xue, Z.; Smith, J.E., Jr. Schiffman, R.A., 7th International Symposium on Experimental Methods for Microgravity Materials Scien ce. Proceedings, pp.79-85 , 1995.

56. Xue, Z.; Noojin, S.L.; Vandegrift, J.G.; Kuruvilla, A.K., Smith, J.E., Jr., JIM, vol 37, no 5 pp1084-90 , 1996.

57. Xue, Z.; Vandegrift, J.G.; Smith, J.E., Jr., Microgravity Science and Technology ,vol 8, no 2, pp 112-17, 1995.

58. A.M. Gokhale, *Interpretation of grain size descriptors*, Transactions of Indian Institute of Metals, vol 35, no 6, pp 595-600, 1982.

59. E.E. Underwood, *Quantitative Stereology*, Addison-Wesley, 1970.

60. A.M. Gokhale, Estimation of bivariate size and orientation distribution of microcracks; Acta mater., vol 44, no 2, pp 475-485, 1996.

61. V. Benes, A.M. Gokhale, M. Slamova, *Unfolding the bivariate size-orientation distribution*, 1996.

62. E.B. Jensen and H.J.G. Gundersen, *The stereological estimation of moments of particle volume*, J. of Applied Probability, 1985.

63. H.J.G. Gundersen and E.B. Jensen, *Stereological estimation of the volume-weighted mean volume of arbitrary particles observed on random sections*, J. of Microscopy, vol 138, pt 2, pp 127-142, 1985.

64. R. Pyrz, *Quantitative descriptionn of composite's microstructure. Part I Morphology of unidirectional composite systems*, Composite Sc. & Tech., vol 50, pp 197-208, 1994.

65. K.H. Hanish and D. Stoyan, *Stereological Estimation of the Radial Distribution Function of Center of Spheres*, Journal of Microscopy (Royal Miscrosc. Soc., U.K.), vol 122, pt 2, pp 131-141, 1980.

66. J.A. Given, J. Blawzdziewicz and G. Stell, J. Chem. Phy., vol 93, pp 8156, 1990.

67. K.H. Hanish, *On The Estimation of Second Order Characteristics of Hard Core Spheres*, Biometrics Journal, vol 25, pp 731-738, 1983.

68. B.D.Ripley, *Spatial Statistics,* John Wiley and Sons, London, U.K. 1981.

69. K.H. Hanish, D. Konig, and D. Stoyan, *The Pair Correlation Function for Point and Fiber Systems and its Stereological Determination by Plane Sections*, Journal of Microscopy (Royal Miscrosc. Soc., U.K.), Vol 140, Part-3, pp 361-370, 1985.

70. S. Chandrasekhar, *Stochaistic Problems in Physics and Astronomy*,Rev. Mod. Phys., vol 15, pp 86-89, 1943.

71. A.J. Ardell and P.P. Bansal, Average Nearest Neighbor Distance Between Uniformly Distributed Finite Particles, Metallography, 1972, Vol 5, pp 97-111.

72. H. Schwartz and H.E. Exner, *The Characterization of Arrangements of Feature Centroids in Planes and Volume*, Journal of Microscopy (Royal Miscrosc. Soc., U.K.), vol 129, pp 155-169, 1983.

73. R.M. German, *The Two-dimensional connectivity of liquid phase sintered microstructures*, Metallurgical Transactions A, vol 18 A, pp 909-914, 1987.

74. K. Wiencek, H. Hougardy, *Description of the homogeneity of particle arrangement*, Acta Stereol., vol 6, no 1, pp 69-74, 1987.

75. K. Wiencek, D. Stoyan, *Spatial correlations in metal structures and their analysis, II: the covariance*, Materials Char., vol 31, pp 47-53, 1993.

76. P. Sabella, *A rendering algorithm for visualizing 3D scalar fields,Computer* Graphics, vol 22, no- 4, pp 51-8, 1988.

77. E. Keppel, *Approximating Complex Surfaces by Triangulation of Contour lines*, IBM Journal of Research & Development, vol 19, no 1, pp 2-11. 1975.

78. E.W. Lorensen, H.E. Cline, *Marching Cubes: A highresolution 3D surface construction algorithms*, Computer graphics, vol 21, no 4, pp 38-44, 1987.

79. Luis-M. Cruz Orive, *Particle size-shape distributions: the general spheroid problem: I Mathematical model*, J. Microscopy, vol 107, pp 235-253, 1976.

80. S.D. Wicksell, *The corpuscle problem. Second memoir. Case of ellipsoidal corpuscles*, Biometrika, vol 18, pp 152, 1926.

81. R.T. DeHoff, *The determination of size distribution of ellipsoidal particles from*

measurements made on random plane sections, Trans. A.I.M.E. vol 224, pp 474, 1962.

82. G.M. Tallis, *Estimating the distribution of spherical and elliptical bodies in conglomerates from plane sections*, Biometrics, vol 26, pp 87, 1970.

83. P.A.P. Moran, *The probabilistic basis of stereology*, Suppl. Adv. Appl. Prob., pp 69, 1972.

84. L.M. Cruz Orive, *Correction of stereological parameters from biased samples on nucleated particle phases. I Nuclear volume fraction*, J. Microscopy, vol 106, pp 1, 1976.

85. L.M. Cruz Orive, *Correction of stereological parameters from biased samples on nucleated particle phases. II Specific surface area*, J. Microscopy, vol 106, pp19, 1976.

86. V. Benes, M. Jiruse, M. Slamova, Stereological unfolding of the trivariate size-shape-orientation distribution of spherodial particles with application; Acta mater., vol 45, pp 1105-1113, 1997.

87. H.J.G. Gundersen, *Stereology of arbitrary particles*, J. Microsc., vol 143, pp 3-45, 1986.

88. H.J.G. Gundersen, *The first Decade of the disector*, in: Proc. 51st Annual Meeting of the Microscopy Society of America (Ed. G.W. Bailey & C.L. Rieder), pp 480, San Francisco Press, 1993.

89. R.T. DeHoff, *Curvature and the topological properties of interconnected phases*, in: Quantitative Microscopy (Ed. by R.T. DeHoff and F.N. Rhines) pp 291. McGraw Hill, New York., 1968.

90. R.E. Miles & P. Davy, *Particle number or density can be estimated bu wedge sections*, J. Microsc.,vol 113, pp 45, 1978.

91. Luis-M. Cruz Orive, *On estimation of particle number*, J. Microsc., vol 120, pp 15-27, 1980.

92. D.C. Sterio, *The unbiased estimation of number and sizes of arbitrary particles using the disector*, J. Microsc., vol 134, pp 127-136, 1984.

93. L.M. Karlsson & L.M. Cruz-Orive, *Estimation of pore size in aluminium using the disector, the selector and Cavalieri's principle.* In: MiCon 90 Symposium on Advances in Video Technology: Materials Science Application, 1990.

94. H.J.G. Gundersen, *Notes on the estimation of the numerical density of arbitary profilesL the edge effect*, J. Microsc., vol 111, pp 219-233, 1977.

95. M.Geiser, L.M. Cruz-Orive, V. Im Hof & P. Gehr, *Counting particles retained in the human lungs with the fractionator*, Acta Stereol, 8/Suppl II, 419-424, 1989.

96. E.M. Jack, L.M. Cruz-Orive, F. Waechter & W. Staubli *Unbiased estimation of cell and nuclear volume in preneoplastic and uninvolved tissue from the same rat liver using the nucleator*, Acta Stereol., 8/Suppl II, 257-262., 1989

97. Pascal Louis and A.M. Gokhale, *Application of Image Analysis for Characterization of Spatial Arrangement of Features in Microstructures*, Metallurgical and Materials Transactions, vol 26A, pp 1449-1456, 1995.

98. Y.Liu, D.F. Heaney, and R.M. German, *Gravity induced solid grain packing during liquid phase sintering*, Acta metall. Mater., vol 43, no 4, pp 1587-1592, 19.

99. N.D. Aparicio, and A.C.F. Cocks, *On the representation of random packing of spheres for sintering simulations*, Acta metall. Mater., vol 43, no 10, pp 3873-3884, 1995.

100. R.M.German, *Microstructure of the gravity settled region in a liquid-phase sintered dilute tungsten heavy alloy*, Met trans. A, vol 26A, pp 279-288, 1995.

101. Zubillaga, C.; Hernandez, F.; Urcola, J.J.; Fuentes, M.,*Experimental analysis of tungsten coarsening in a heavy metal during liquid phase sintering*, Acta Metallurgica vol 37, no 7, pp 1865-72, 1989.

102. Y.Masuda and R.Watanabe: in Sintering Processes, G.C. Kuczynski, ed., Plenum Press, New Your, NY, pp 3-21, 1980.

103. Boettinger, W.J.; Voorhees, P.W.; Dobbyn, R.C.; Burdette, H.E, *A study of the coarsening of liquid-solid mixtures using synchrotron radiation microradiography*, Metall. Trans. A, vol 18A, pp 487-90, 1987.

104. E.G. Zukas, P.S.Z. Rogers, and R.S. Rogers, *Spheroid growth by coalescence during liquid phase sintering*, Z. Metallkd., vol 67, pp 591-95, 1976.

105. R.M. German; A. Bose.; S.S. Mani, *Sintering time and atmosphere influences on the microstructure and mechanical properties of tungsten heavy alloys*, Metallurgical Transactions A, vol 23A, no 1, pp 211-19, 1992.

106. T.H. Courtney; *Gravitational effects on microstructural development in liquid phase sintered*, Scripta Materialia, vol.35, no 5, pp.567-71, 1996.

Table 2.1 Effect of solubility ratio on different alloy systems in liquid phase sintering.

Base	Additive	Solubility ratio S_B/S_A	Behavior
Al	Zn	0.004	Swell
Cu	Al	0.1	Swell
Cu	Sn	0.001	Swell
Cu	Ti	4	Shrink
Fe	Al	0.02	Swell
Fe	B	7	Shrink
Fe	Cu	0.07	Swell
Fe	Sn	0.01	Swell
Fe	Ti	3	Shrink
Mo	Ni	20	Shrink
Ti	Al	0.0003	Swell
W	Fe	5	Shrink

Table 2.2 Different mechanisms of neck growth and coarsening.

Factor	Contact Flattening	Dissolution of fine grains	Solid neck growth	Coalescence
Material source	contact zone	small grains	grain boundary	connected grain
Transport path	liquid	liquid	solid	solid
Driving force	solid-liquid interfacial	solid-liquid interfacial	solid-liquid interfacial	curved solid-solid interface
Grain coarsening	No	Yes	No	Yes
Shape accommodation	Yes	Yes	Yes	Yes
center-to-center approach	Yes	Not necessarily	Yes	No
Solubility in liquid	Required	Required	Not required	Not required

Table 2.3 Rate controlling step for grain growth in different alloy systems.

Diffusion Controlled grain growth	Reaction controlled grain growth
W-Ni-Cu	WC-Co
W-Ni-Fe	NbC-Fe-B
W-Ni	TiN-TiC-Ni
Mo-Ni-Fe	PbS-NaCl-KCl
Pb-Sn	$SmCo_5$-Sm-Co
TiC-Co	
Co-Cu	
Cu-Ag	
Fe-Cu	

Table 2.4 List of field specific, region specific and spatial attributes of the microstructure.

Field Specific attribute	**Region Specific attribute**	**Spatial attribute**
Volume fraction	Grain size and distribution	Radial Distribution function
Surface area per unit volume	Grain shape and orientation	Nearest neighbor distribution function
Length per unit volume		
Mean free path in a phase		

Table 3.1 Relation between the mean number of particle contacts in 3D (N_C) to the mean value observed in 2D [73].

Dihedral angle ϕ, Deg	Mean value observed in 2D for $N_C = 4$	Mean value observed in 2D for $N_C = 6$	Mean value observed in 2D for $N_C = 8$
15	0.42±0.59	0.42±0.59	0.42±0.59
30	0.80±0.75	1.22±0.89	1.63±1.03
45	1.21±0.83	1.81±0.95	2.38±1.12
60	1.56±0.85	2.34±1.00	3.10±1.25
75	1.93±0.86	2.83±1.03	3.69±1.52

Table 4.1 Mean number of inter-particle contacts per particle in 3D and that in 2D measured in 83 wt% WHA(using three dimensional probe disector) .

Microstuctural property	Sample description and location of measurements	Normal gravity		Microgravity	
		1 min	120 min	1 min	120 min
Mean number of inter-particle contacts per particle in 2D.	83 wt % WHA, BOTTOM	1.03	1.10	0.84	0.74
Mean number of inter-particle contacts per particle in 3D.	83 wt % WHA, BOTTOM	3.7	4.3	2.9	2.9

Table 4.2 Experimentally computed value of proportionality constant C_0, in the equation 4.10 representing the variation of coordination number with height.

	83 wt% WHA, 1 min, gravity	83 wt% WHA, 120 min, gravity	Calculated by Lui et al.
C_0	1.2	2.3	1.9

Table 4.3 Global microstructural properties of 78 wt% W-Ni-Fe and 83 wt% W-Ni-Fe liquid phase sintered alloys.

Microstructural Property	Sample description and location of measurements	Normal Gravity		Microgravity	
		1 minute	120 minute	1 minute	120 minute
Volume fraction of W grains V_V	78 wt % WHA, TOP	0.63	0.67	0.58	0.56
	83 wt% WHA TOP	0.61	0.67	0.58	0.58
	83 wt% WHA BOTTOM	0.69	0.74	0.59	0.59
Surface area of W grain-matrix interface S_V $(\mu m)^{-1}$	78 wt % WHA, TOP	0.132	0.089	0.155	0.083
	83 wt% WHA BOTTOM	0.135	0.092	0.152	0.082
Mean free path λ (μm)	78 wt % WHA, TOP	2.8	3.7	2.7	5.2
	83 wt% WHA BOTTOM	2.3	2.8	2.7	5.0

Table 4.4 True mean 3D calliper diameter (i.e. 3D size), volume number density Nv (measured by disector), mean grain volume (ratio of volume fraction and Nv), volume weighted mean volume, and CV of the volume distribution (calculated from volume weighted mean volume and mean volume) are listed for the 83 wt% WHA.

Microstuctural property	Sample description and location of measurements	Normal gravity		Microgravity	
		1 min	120 min	1 min	120 min
Mean 3D calliper diameter (μm)	83 wt % WHA, BOTTOM	15.7	29.8	12.0	30.6
Number density of tungsten grains in 3D measured by disector. $(\mu m)^{-3}$	83 wt % WHA, BOTTOM	12.3 E-05	2.6 E-05	20.9 E-05	2.4 E-05
Mean volume (μm)	83 wt % WHA, BOTTOM	5.6 E+03	28 E+03	2.8 E+03	25 E+03
Volume weighted mean volume $(\mu m)^3$	83 wt % WHA, BOTTOM	9.8 E+03	55 E+03	5.1 E+03	38 E+03
Coefficient of variation (CV) of grain volume distribution	83 wt % WHA, BOTTOM	0.74	0.97	0.81	0.55

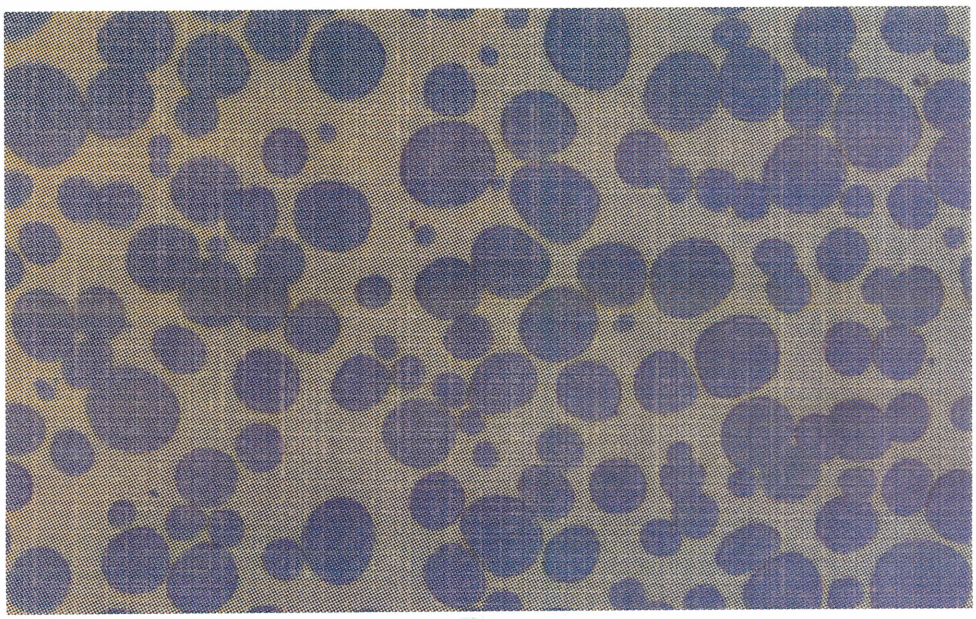

Figure 2.1 A typical micrograph of liqiud phase sintered tungsten heavy alloy.

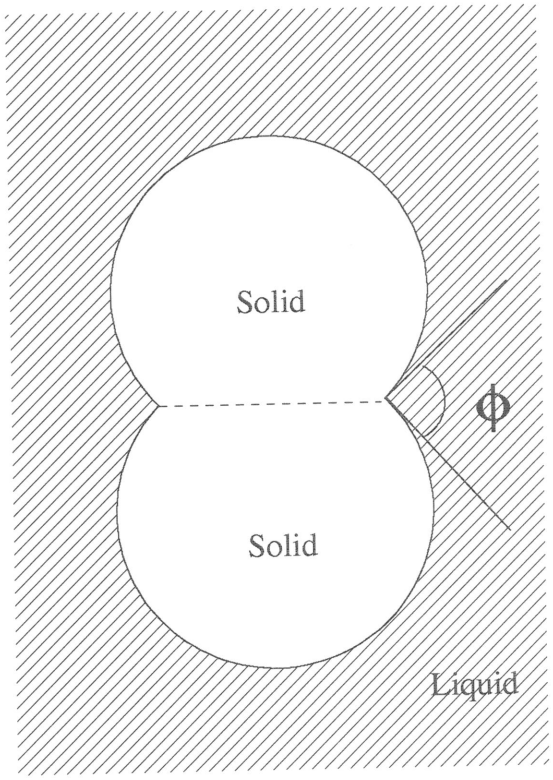

Figure 2.2 Dihedral angle is the angle between the two solid - liquid interfacial surfaces.

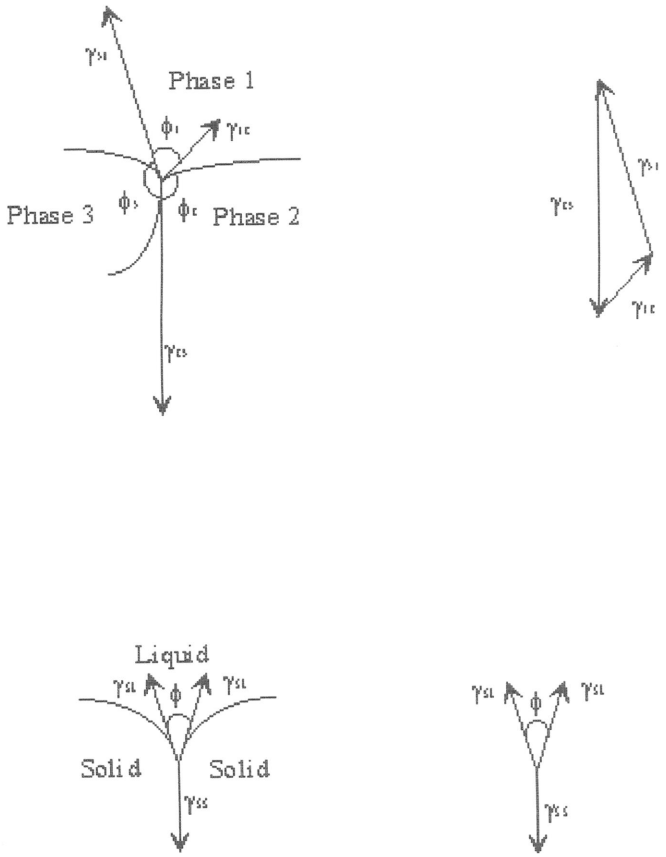

Figure 2.3 Surface energy equilibrium at interfaces. (a) Equilibrium at three phase intersection, (b) Special case of three phase equilibrium, in which two phases are same (i.e., solid)

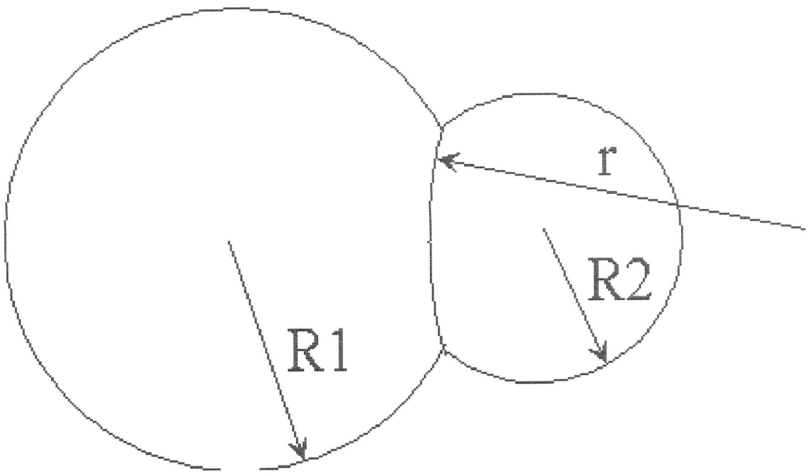

Figure 2.4 Geometry of intergranular boundary between two grains of different sizes.

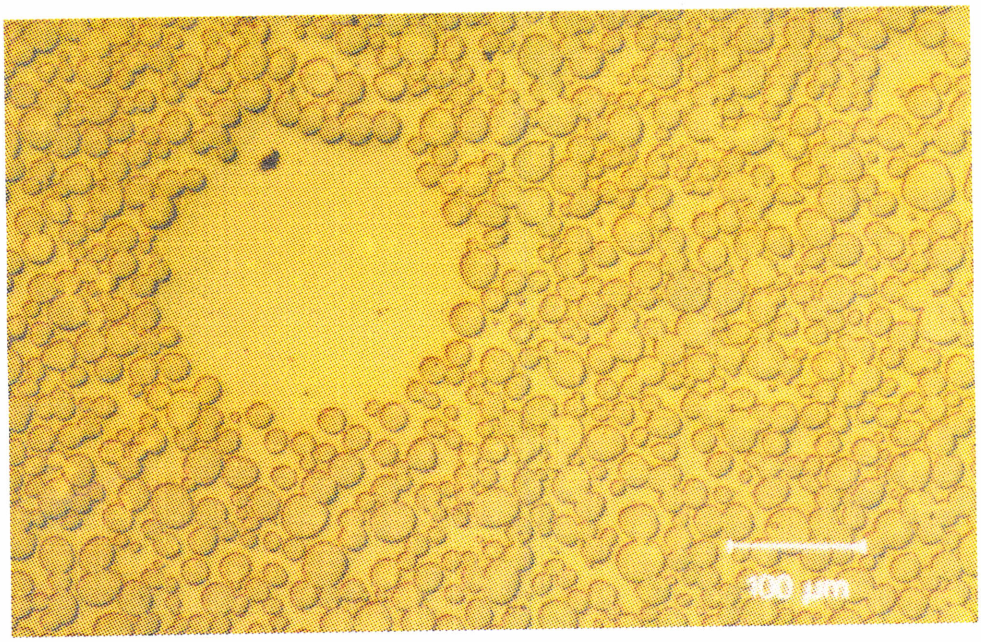

Figure 2.5 Micrograph of tungsten heavy alloy showing regions with no particles, known as liquid pockets.

S_B = Solubility of base in addative

S_A = Solubility of addative in base

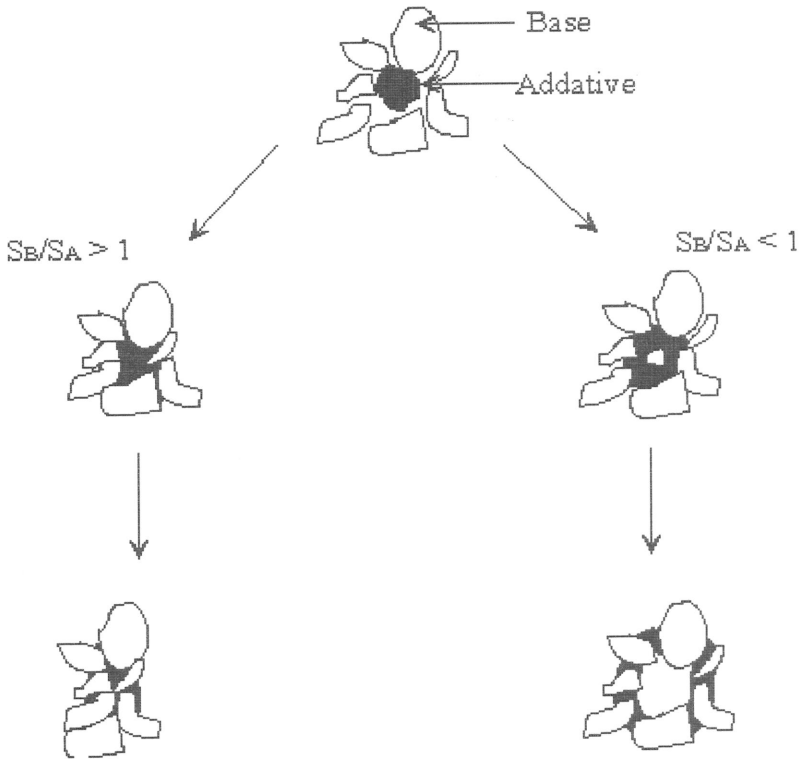

Figure 2.6 Effect of solubility ratio on initial densification.

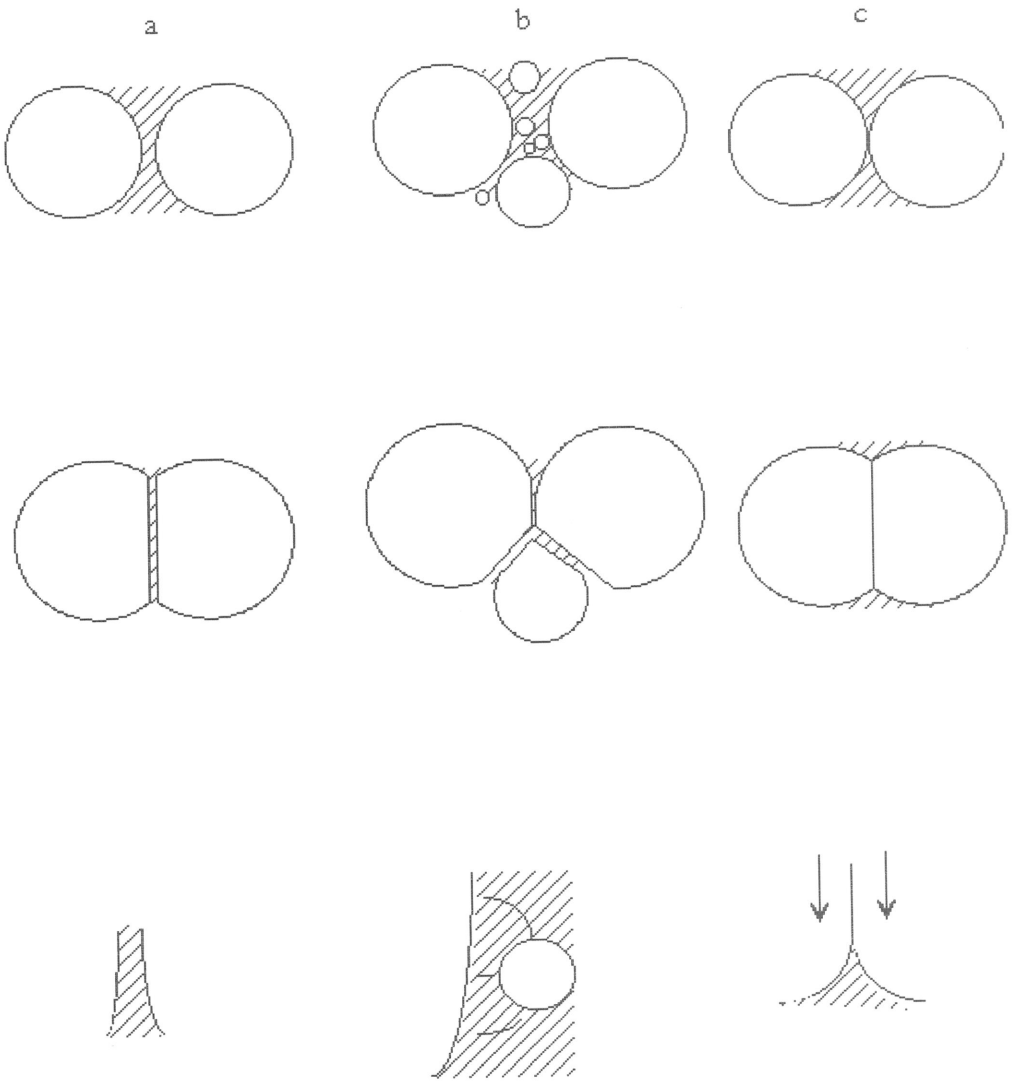

Figure 2.7 Different mechanisms of grain shape accomodation. (a) Contact flattening, (b) dissolution of small grains, and (c) solid state diffusion.

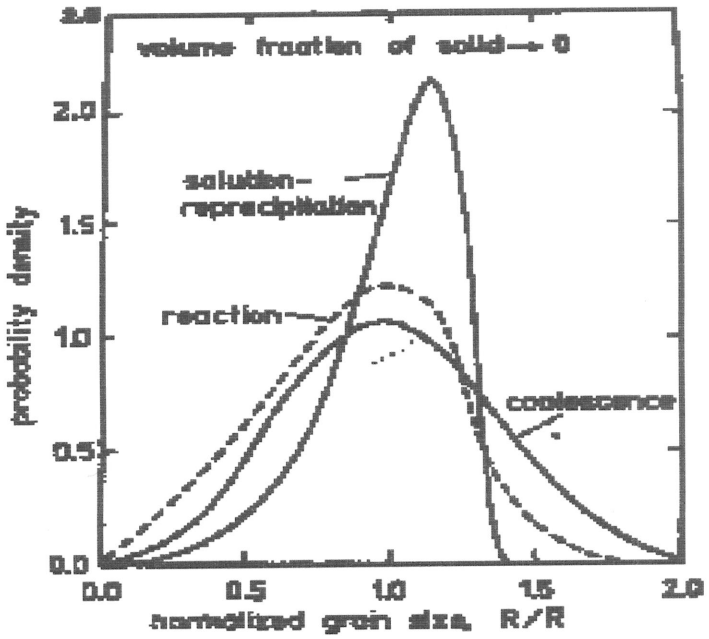

Figure 2.8 Predicted particle size distribution during liquid phase sintering based on different mechanisms [ref. 3].

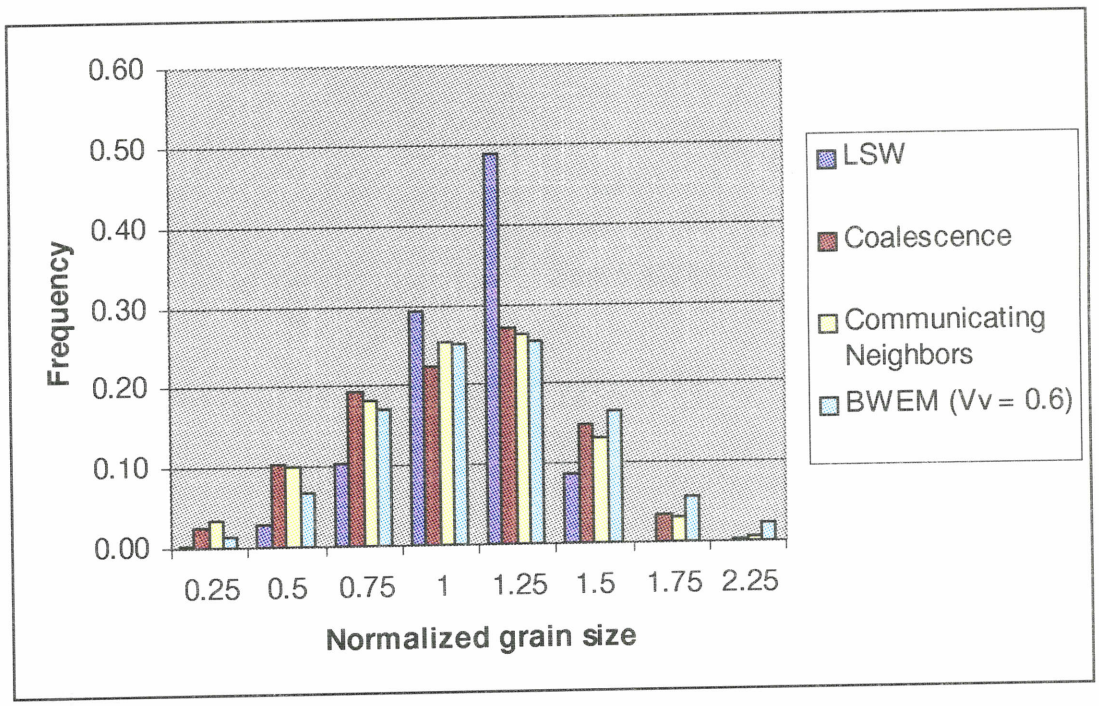

Figure 2.9 Prediction of particle size distribution during liquid phase sintering by various models.

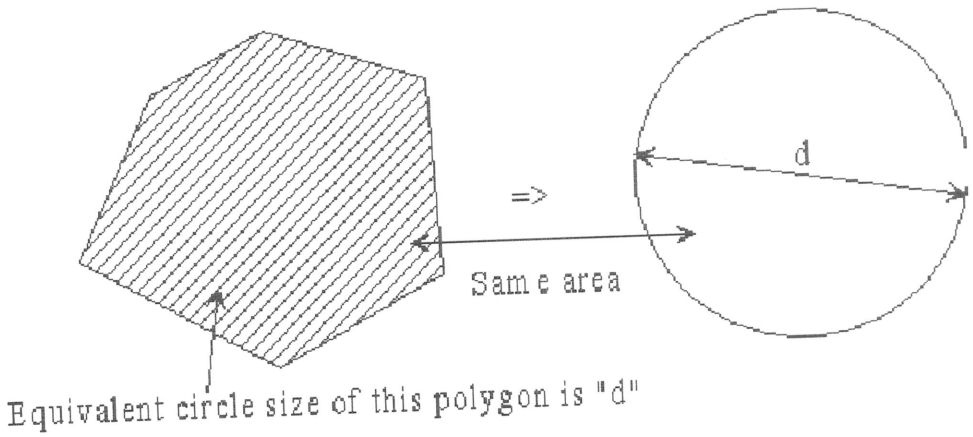

Figure 2.10 Schema for estimation of 2D size of sections of non-circular objects.

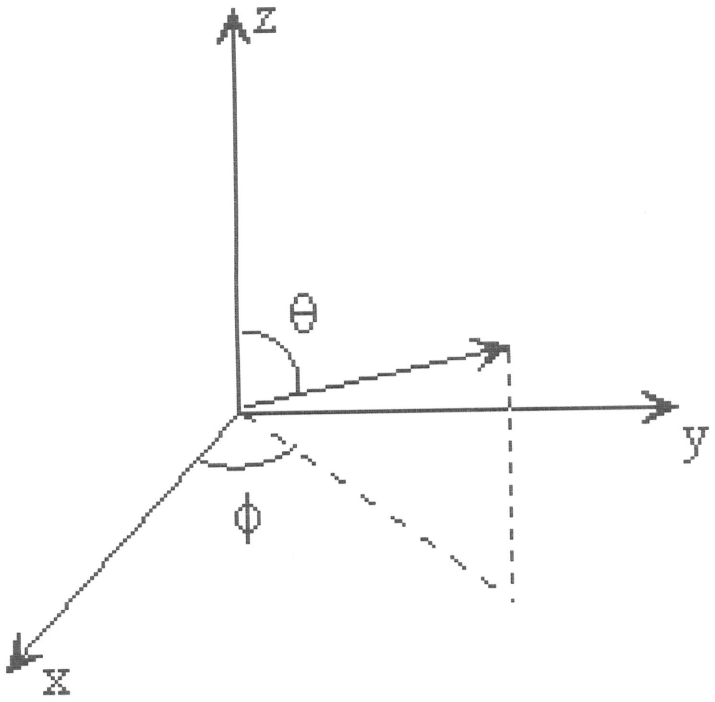

Figure 2.11 Representation of orientation of objects in 3D requires the knowledge of angles θ and angle φ. For systems with rotational symmetry about z-axis (reffered as vertical axis in the text) only the knowledge of angles θ is required to fully describe their orientation.

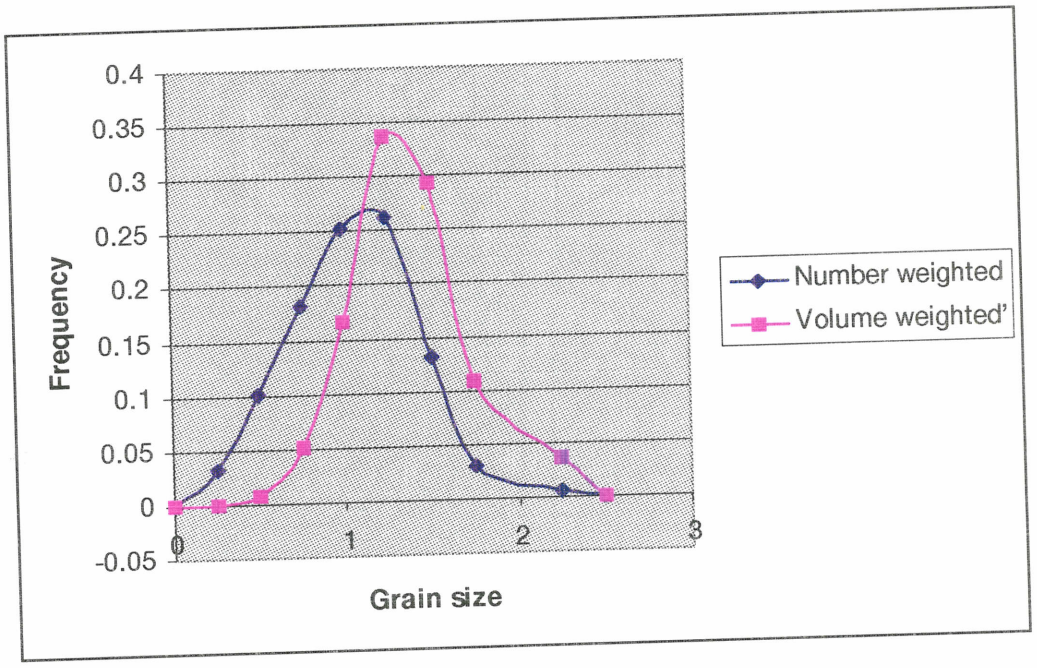

Figure 2.12 A typical number weighted and volume weighted particle size distribution.

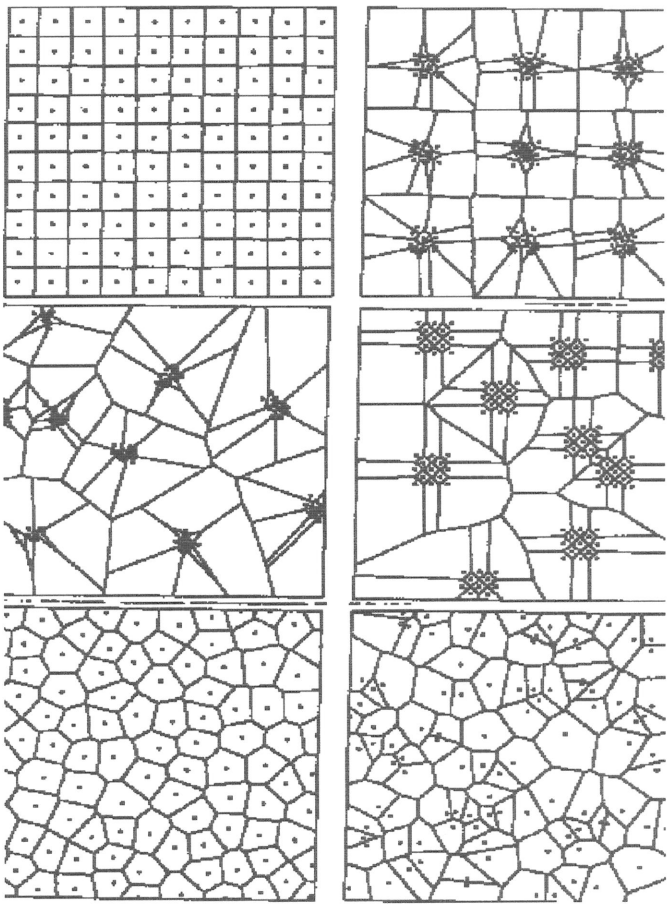

Figure 2.13 Classification of point patterns [ref. 36] (from top left to bottom right): regular, regular-cluster, random-cluster, regular-random, hard-core, Poisson.

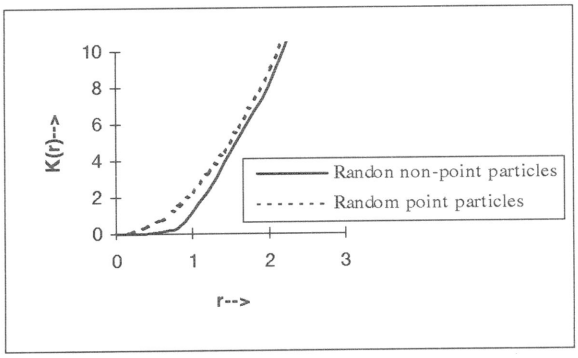

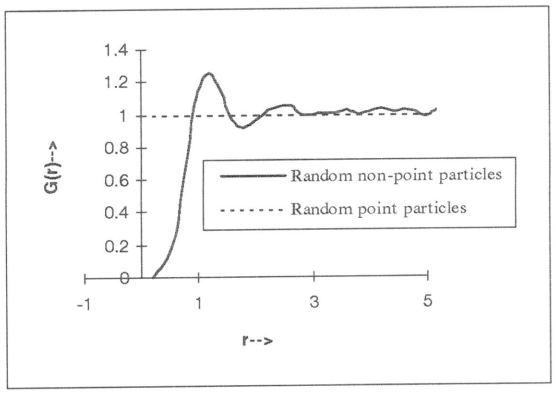

Figure 2.14 K(r) and G(r) functions for random point particles and random non-point particles (i.e., hard-core) in 2D.

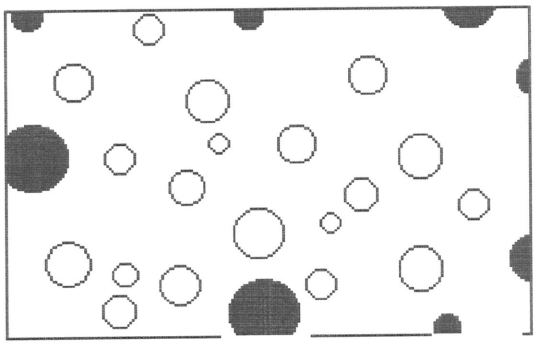

Figure 2.15 Particles cutting the edges cannot be properly accounted, this leads to edge effect problem.

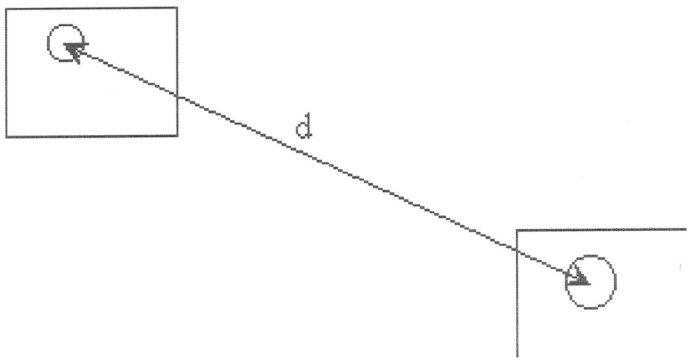

Figure 2.16 One cannot measure the distance between two particles which are present in two far away field, unless they are in a montage.

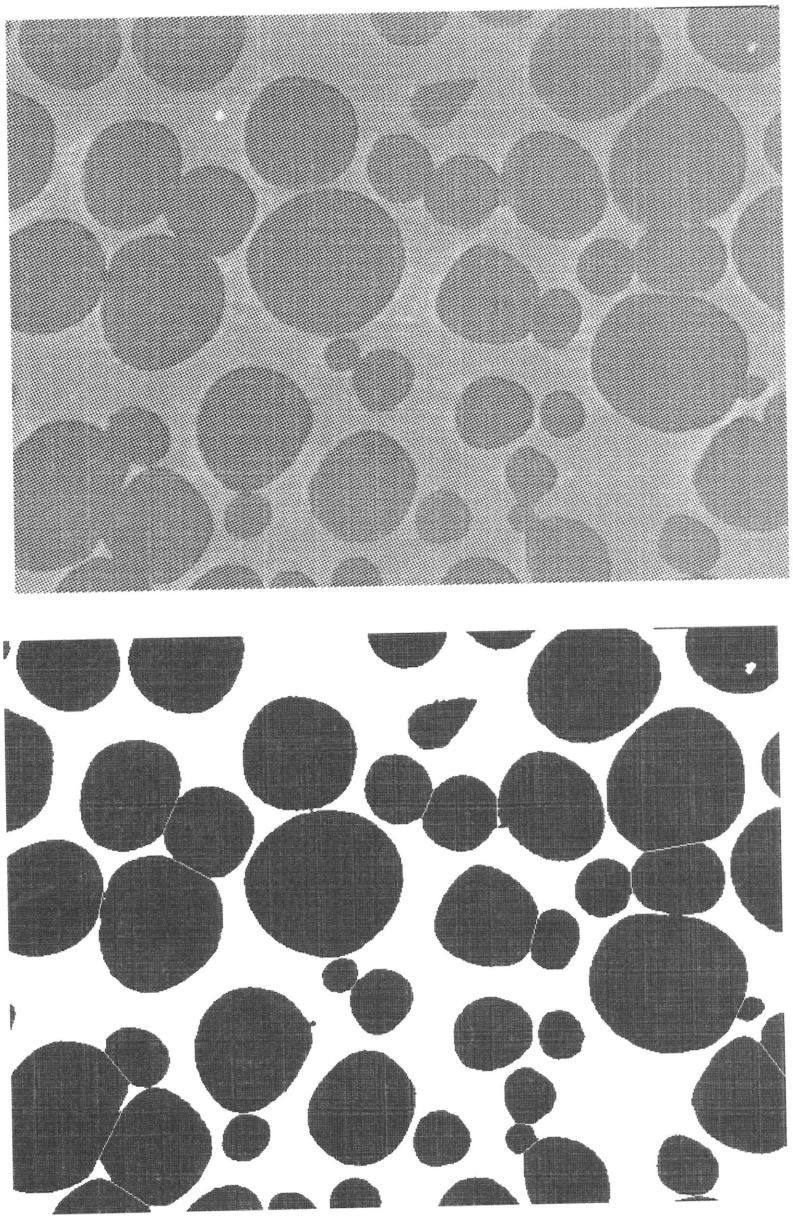

Figure 2.17 A schematic display of the process of segmentation and feature separation.

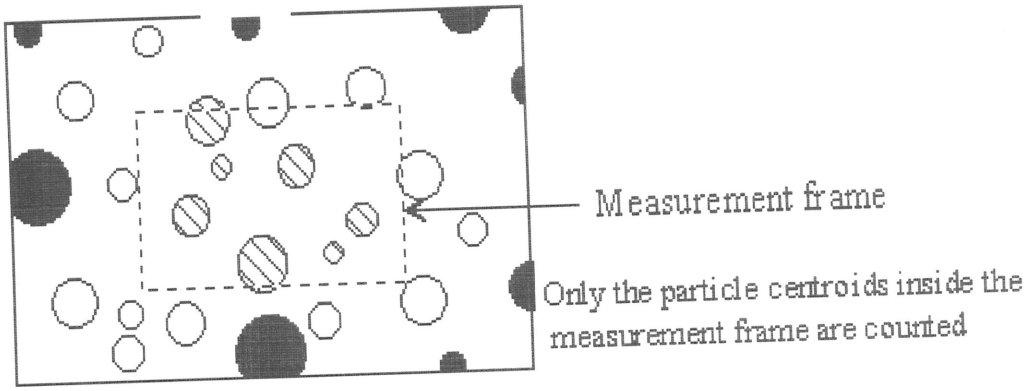

Figure 2.18 Measurement in a montage using measurement frame.

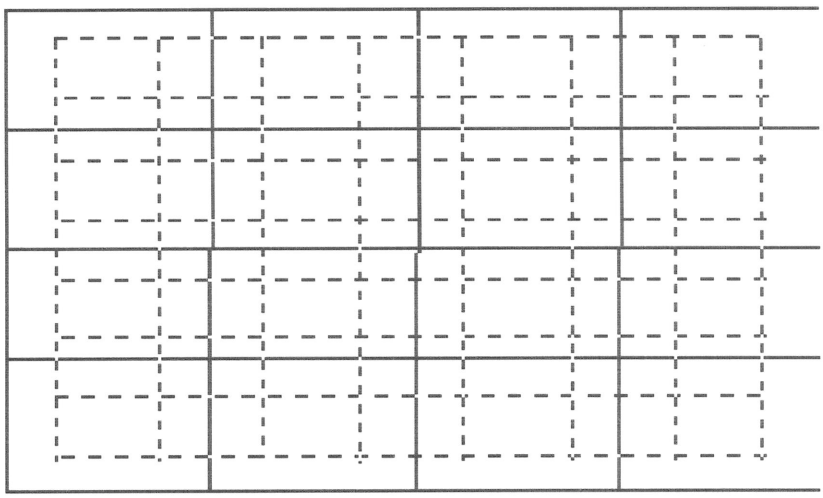

Figure 2.19 Application of measurement frame to a montage of 16 field of views.

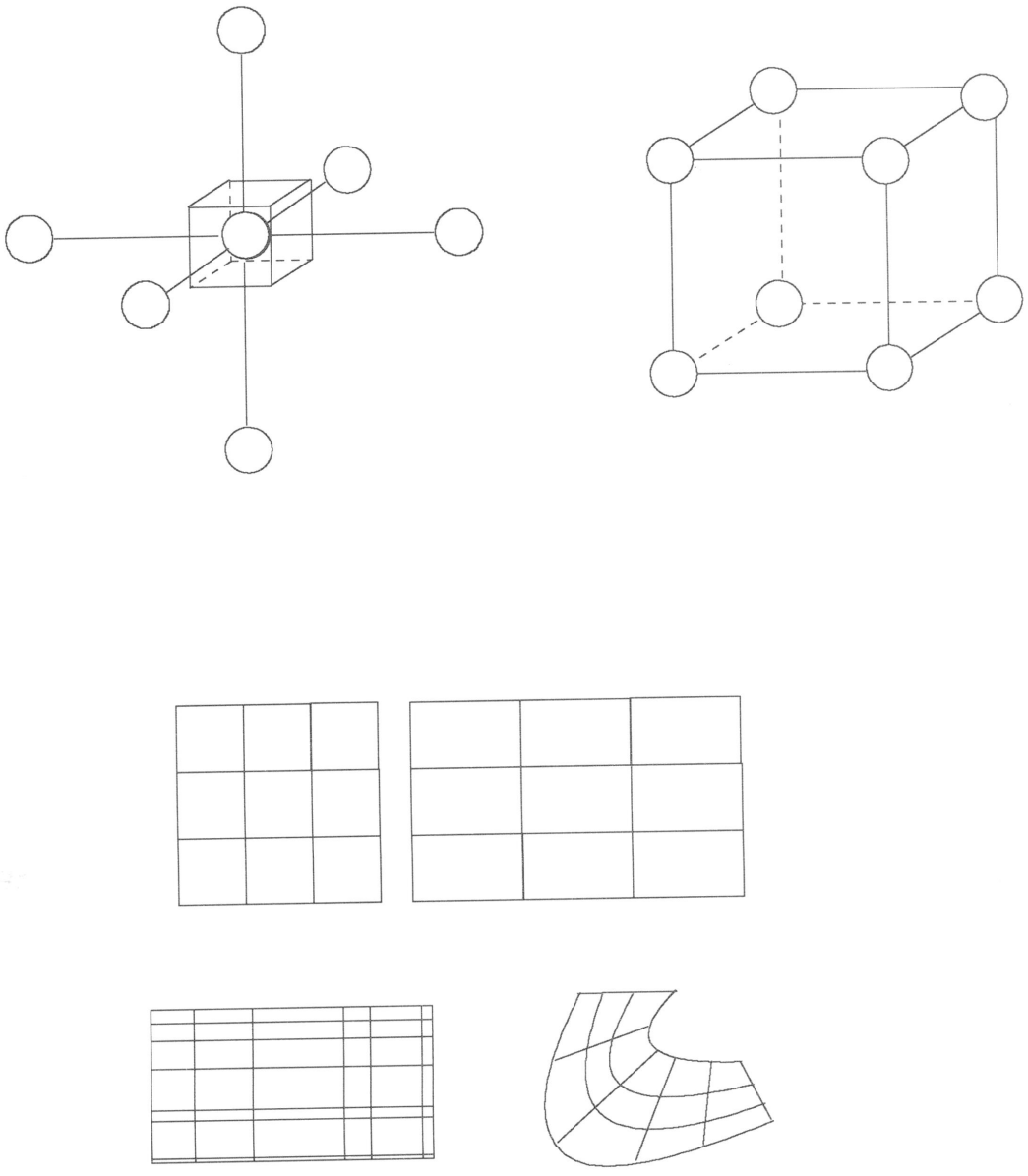

Figure 2.20 Two ways of representation of volume data by voxels and cells.

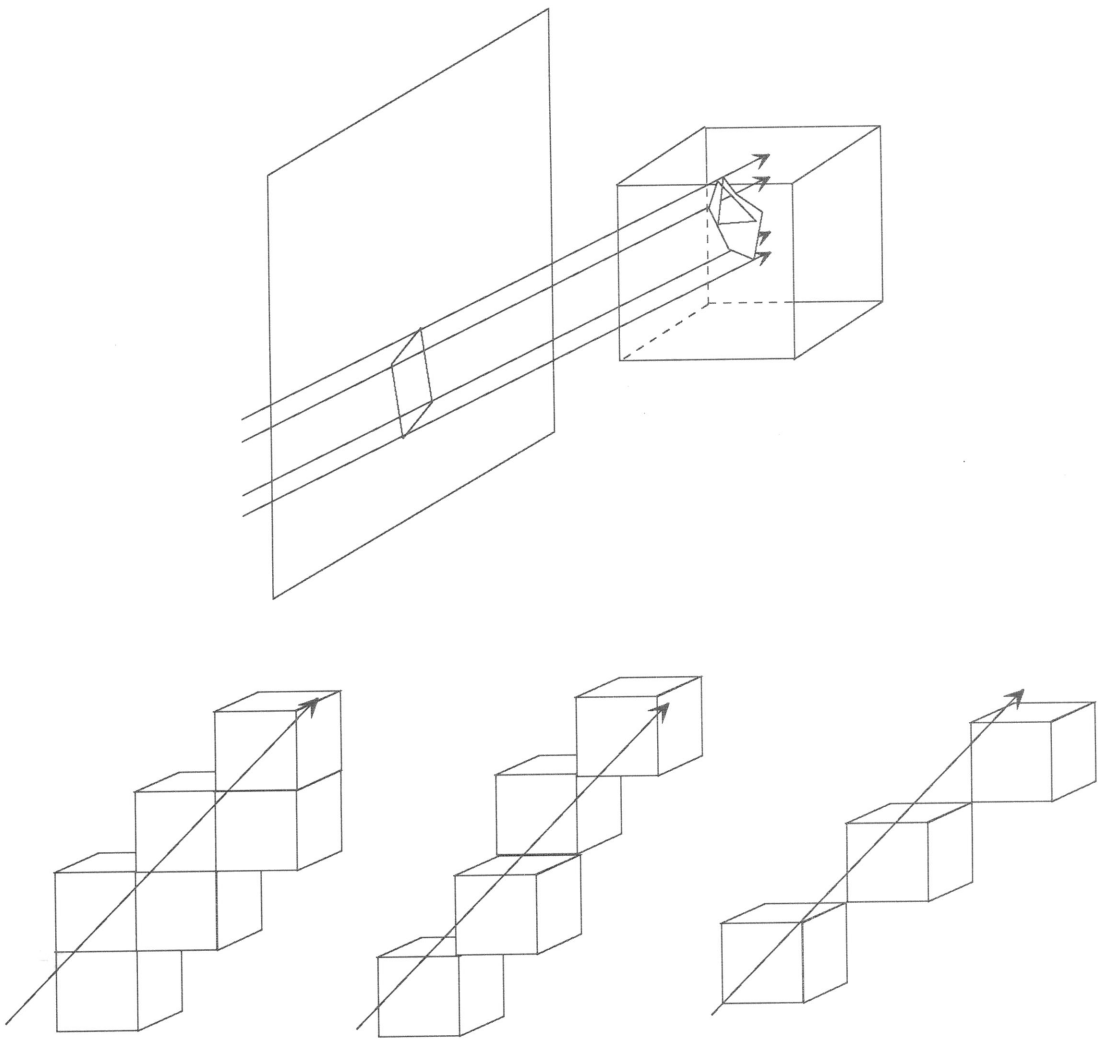

Figure 2.21 a) Data traversal in Ray-casting surface rendering algorithm is from the image plane to the volume. b) Different types of connectivity which are possible in 3D.

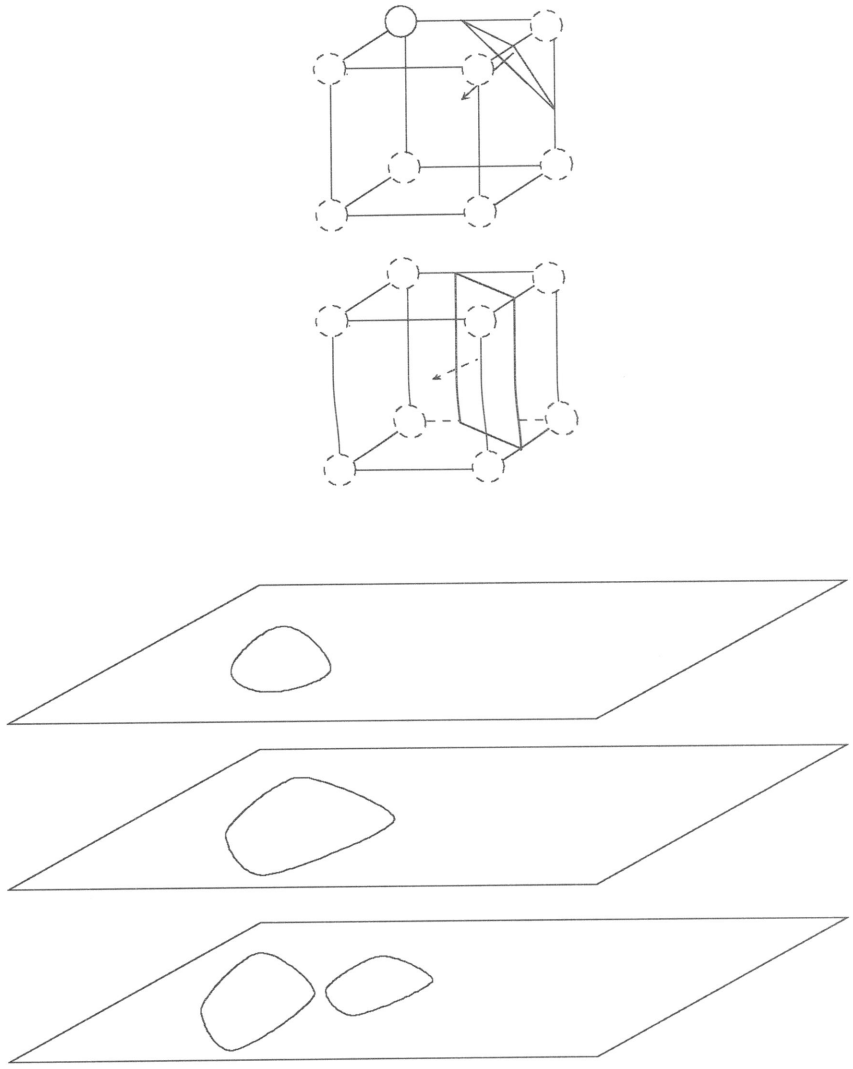

Figure 2.22 a) Problems associated with contour connecting algorithm when contours breakup into smaller contours in adjacent sections. b) Extraction of iso-surfaces using marching-cube algorithm.

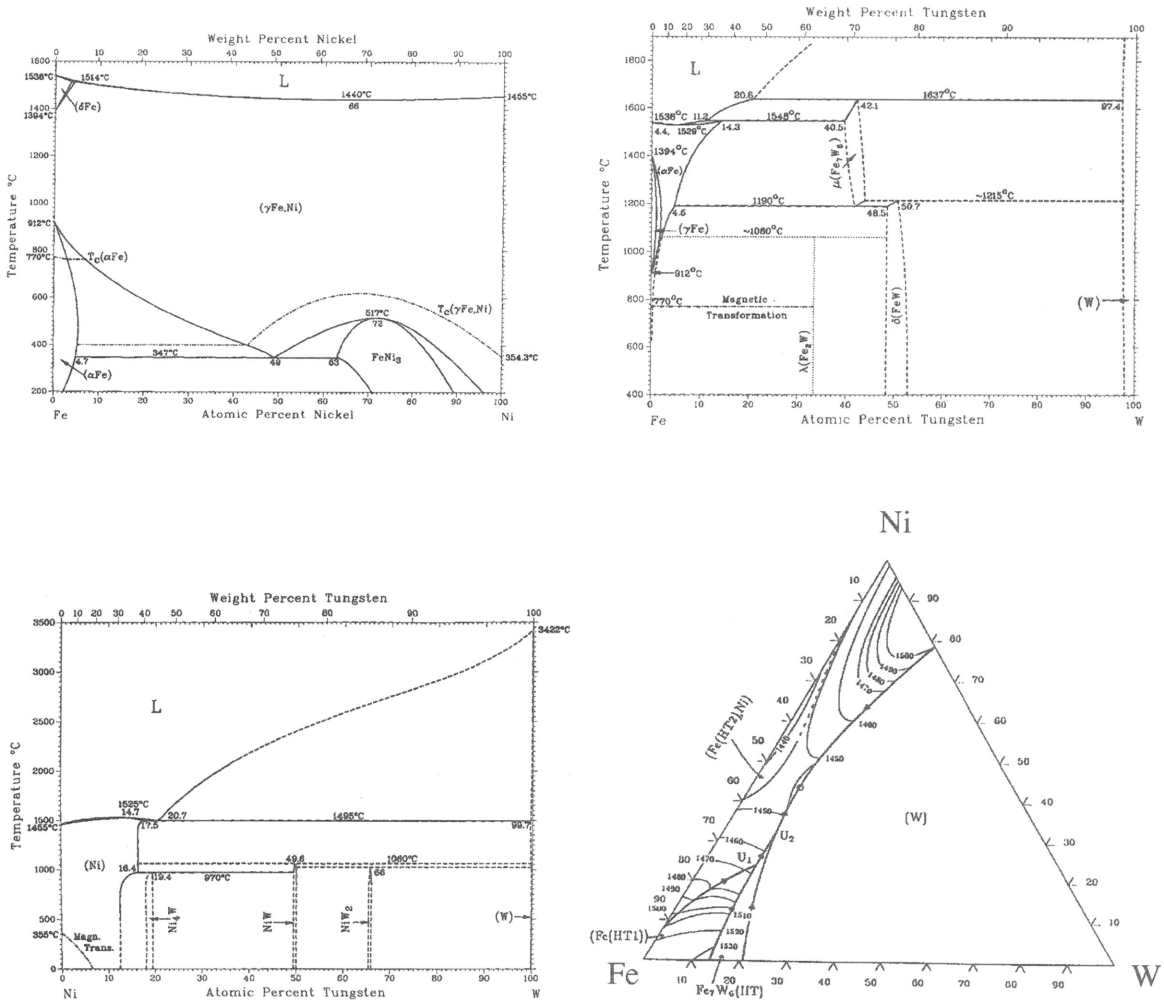

Figure 3.1 Binary and ternary phase diagram for W-Ni-Fe system.

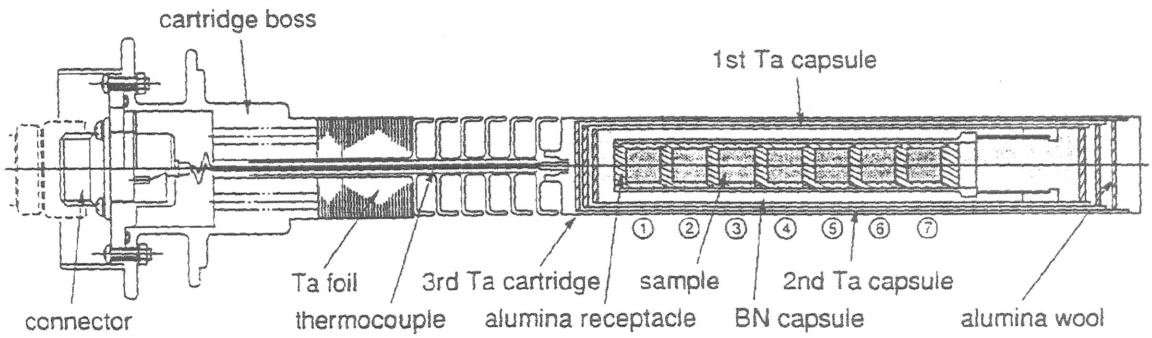

Figure 3.2 Experimental setup for the furnace used in space shuttle Columbia.

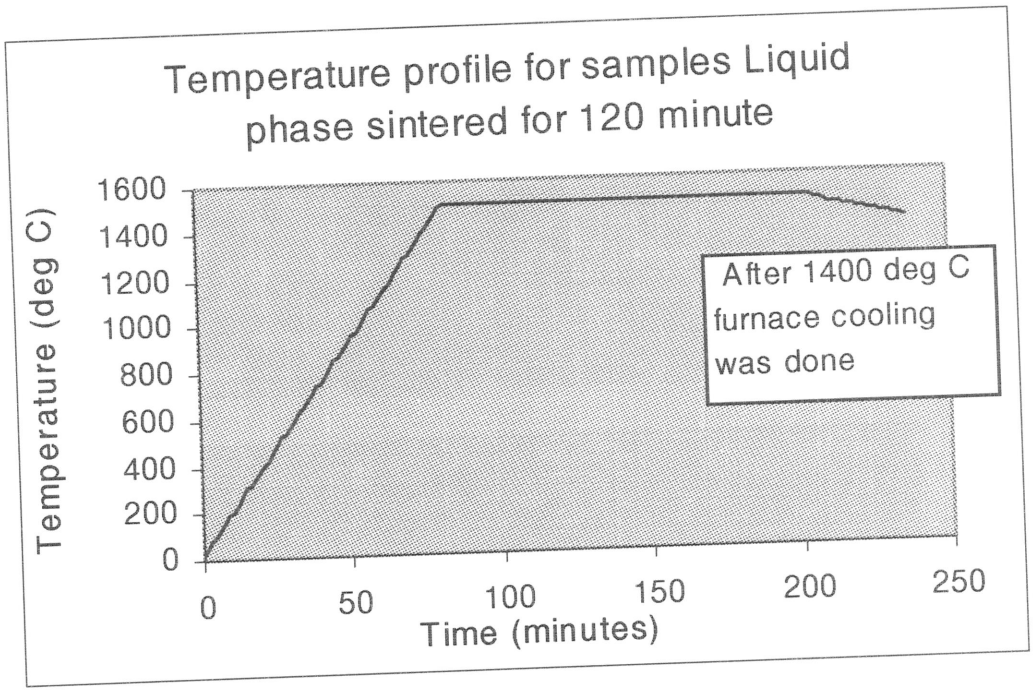

Figure 3.3 Time-temperature profile of the specimen during LPS.

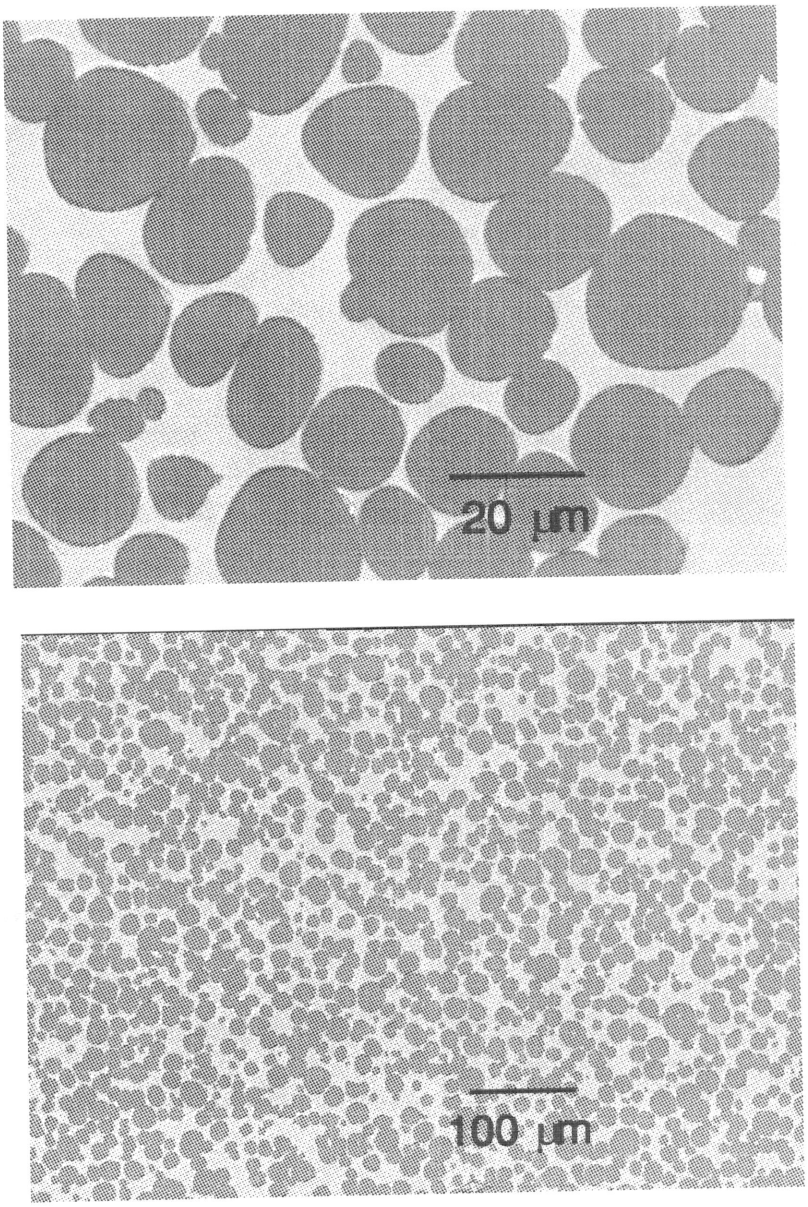

Figure 3.4 a) A typical micrograph of 83 wt% W 11.9% Ni and 5.1% Fe alloy liquid phase sintered in micro-gravity at 1780 K for a duration of 1 minute. b) A low resolution micrograph of the same alloy as in Figure-3.4a.

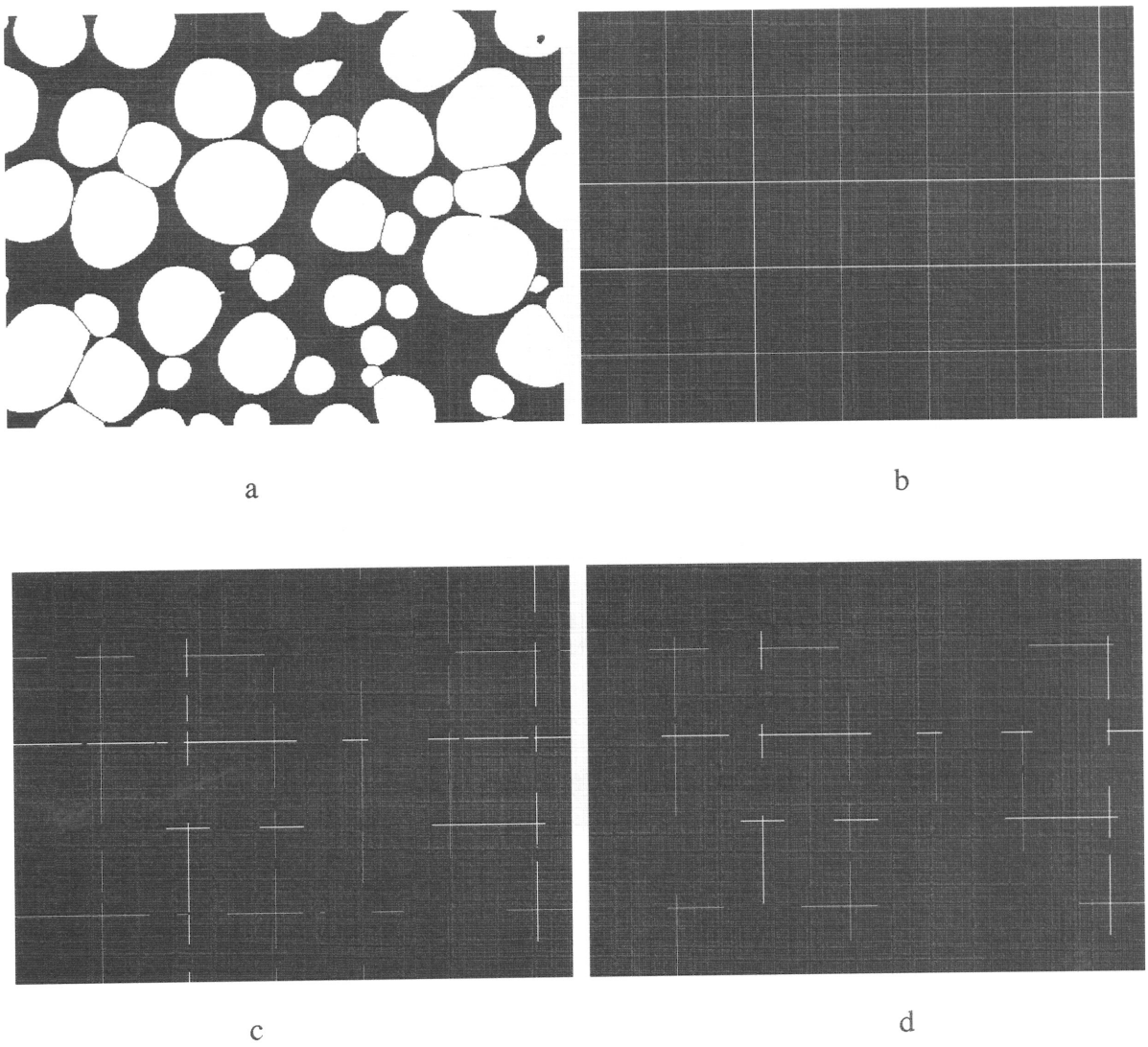

Figure 3.5 Digital image processing steps to measure volume weighted mean volume of the tungsten grains.

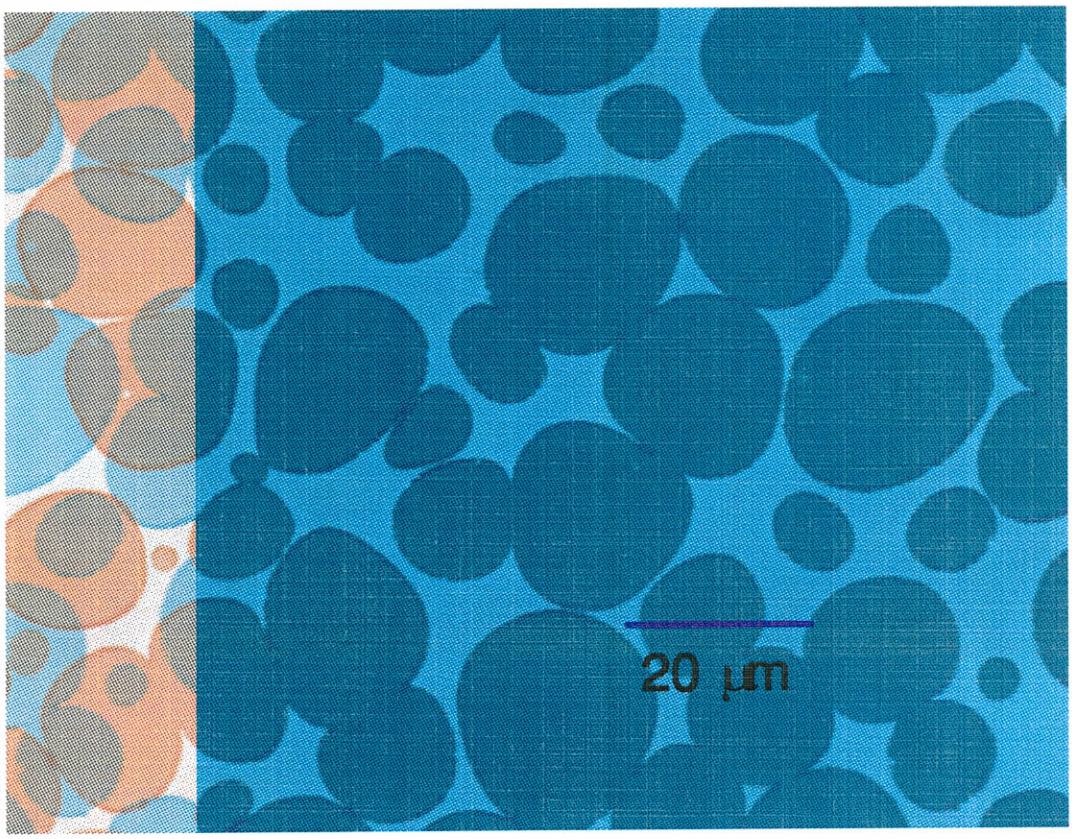

Figure 3.6 A display frame in the process of montage creation. The frame shows a live image with a superimposed image on the left border (the superimposed image is made up of the live image and the right border of the previous image).

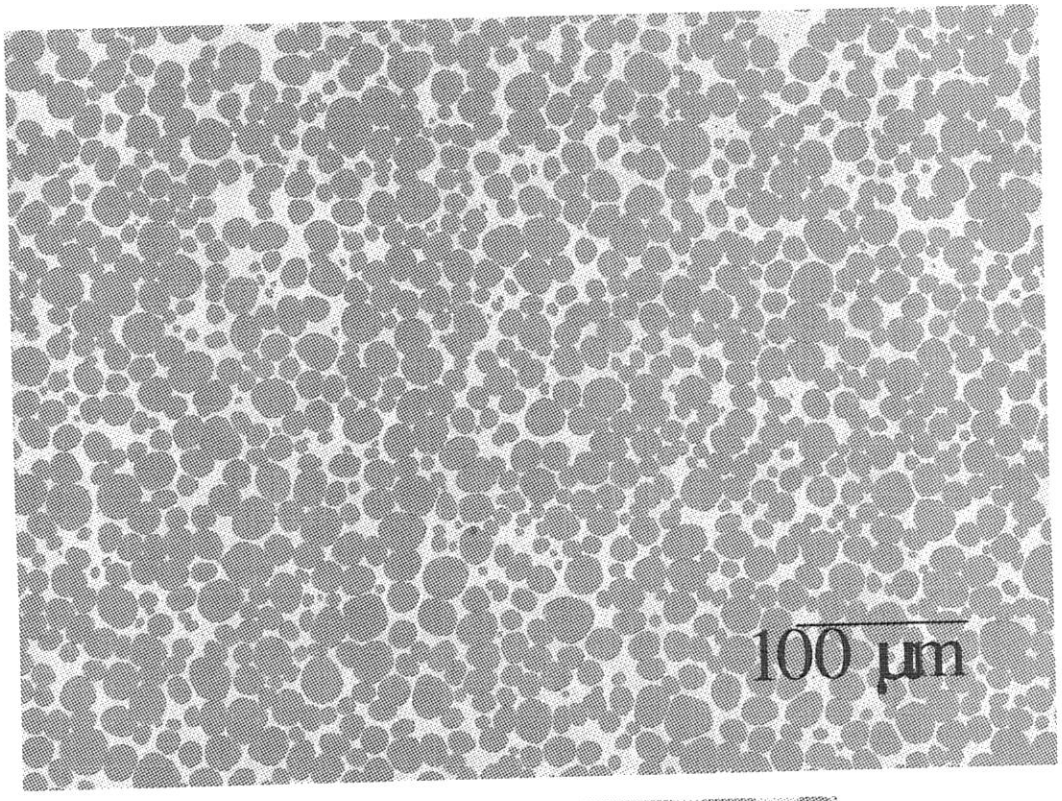

Figure 3.7 a) A montage of exactly contiguous 25 fields of view. This is a very high resolution image and covers a very large area of the microstructure. The resolution of this image not apparent because it has been compressed for the display purpose. b) This is one field of view of the 25 FOV of the montage at its full resolution. The whole montage of 25 FOV shown in Figure-7a is at this high resolution.

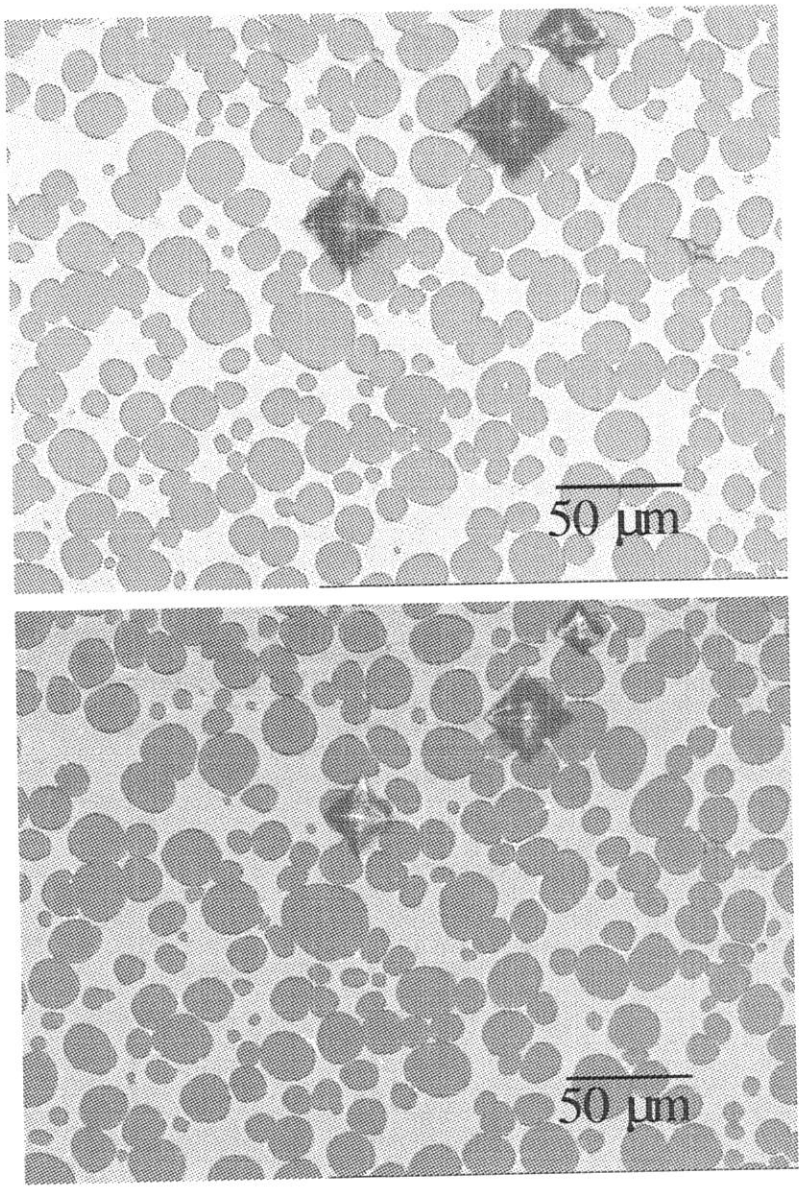

Figure 3.8 Two micrographs showing the fading micro-hardness indents on the metallographic sections on serial sectioning. These indents were used for measuring the amount of material removed during each sectioning and for aligning the serial sections.

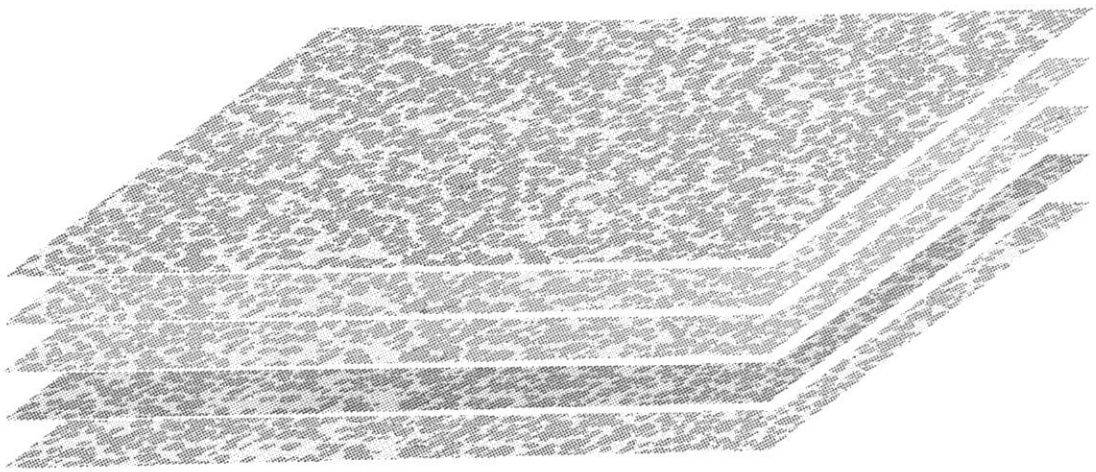

Figure 3.9 Stack of five montage serial sections. There are 90 such serial sections used in this research to do 3-D reconstruction.

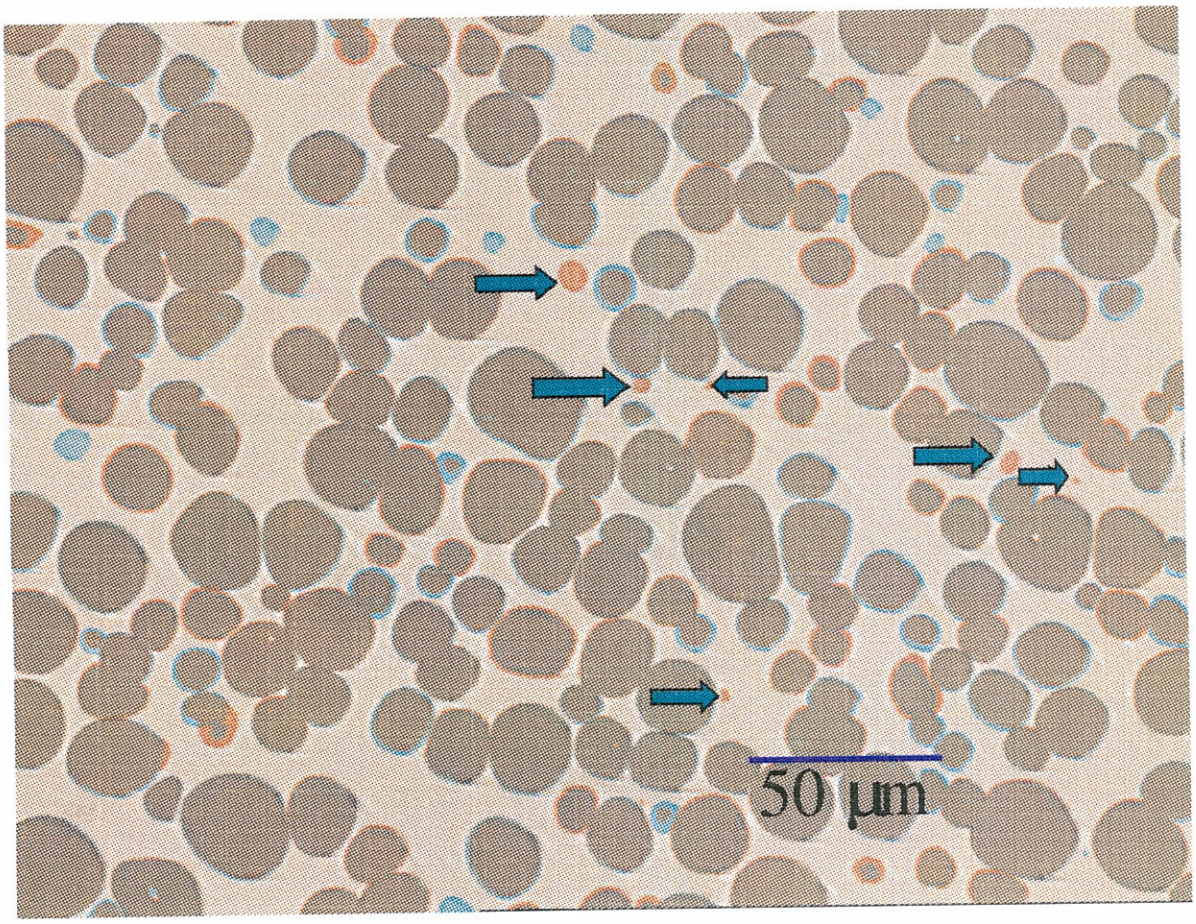

Figure 3.10 Sampling tungsten grains using disector. Figure is a false colored image with red image plane being represented by the first section and blue and green image plane being represented by the next section. The appearance of new particle in the image can be seen by red colored particles (which are not present in the red image plane i.e. the first section, but are present in the green and blue image plane, i.e. the next section) shown by arrows

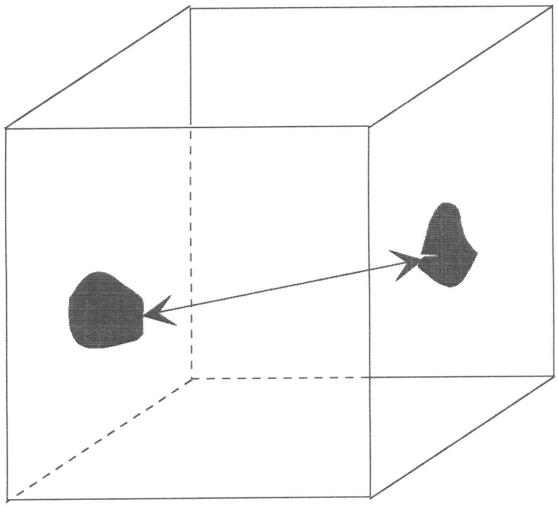

Figure3.11 A 3-D cubic element of the microstructure showing two pores. On observing just this element one way reach to a wrong conclusion that these two pores are the nearest neighbor of each other

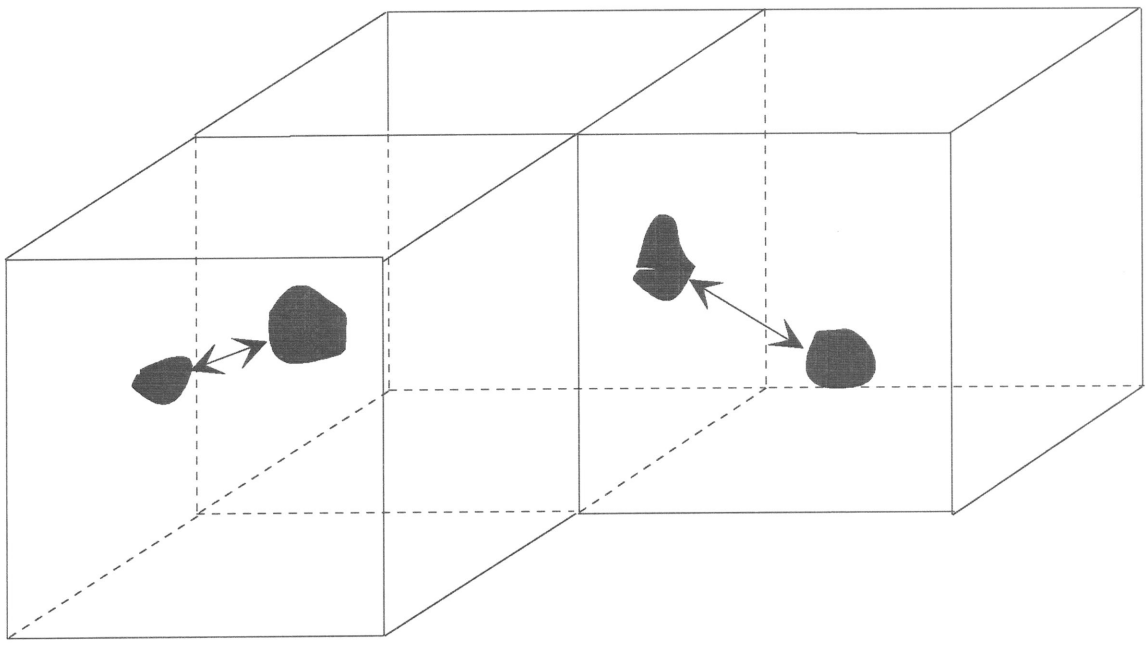

Figure 3.12 A 3-D analog of montage is shown with three cubic elements of the microstructure with the center element being the same as in Figure-3.11. It is now clear that the nearest neighbors of the two pores in the center element are present in the adjoining cubes. Thus the conclusions about nearest neighbor cannot be drawn from observations of just one isolated cubic element.

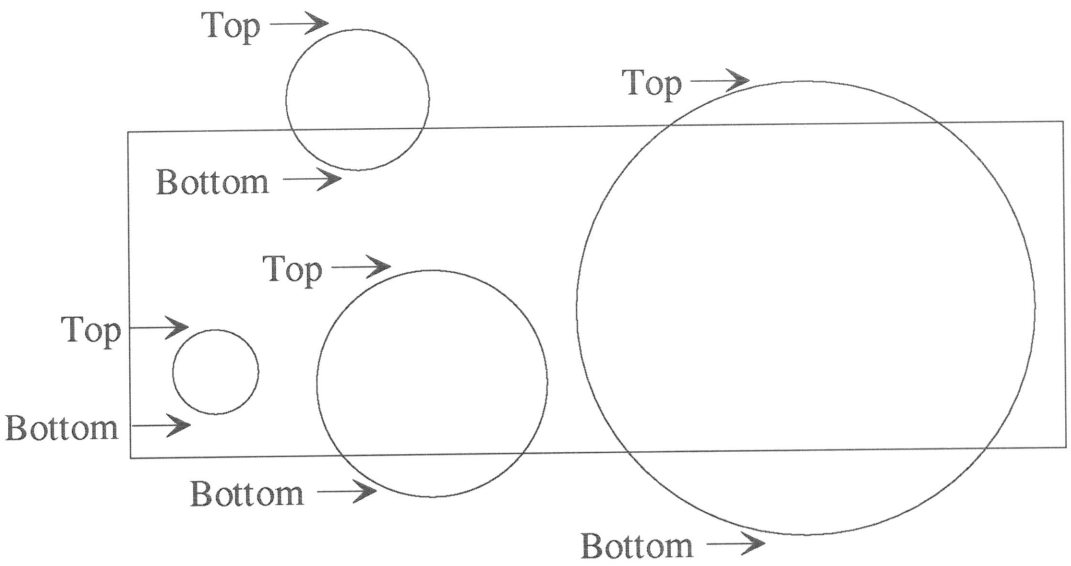

Figure 3.13 This shows all possible ways in which particles can be arranged which have their centroids in the volume of consideration.

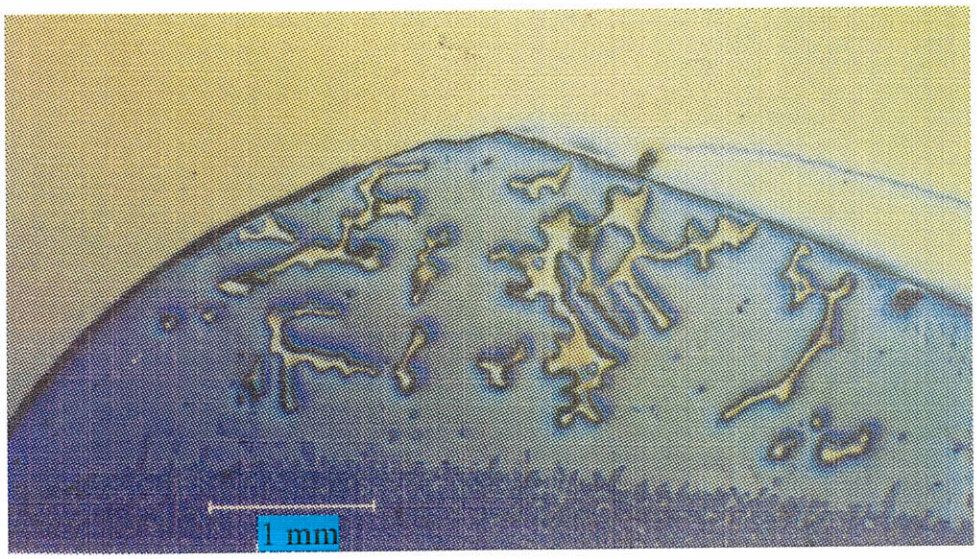

Figure 4.1 Low magnification micrograph of 78wt % W-N-Fe specimen, liquid phase sintered for 120 minute in normal gravity.

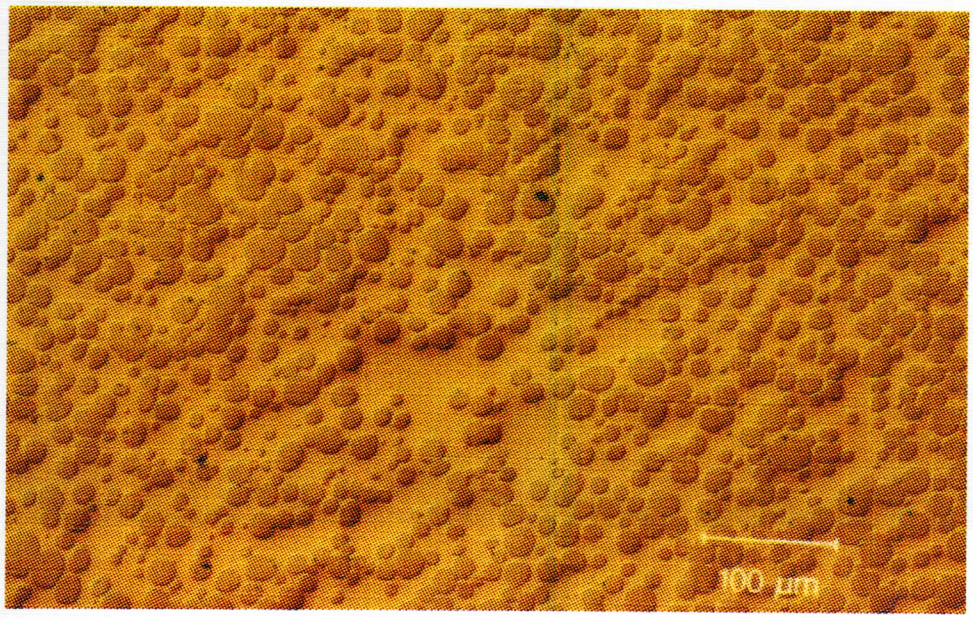

Figure 4.2 A typical micrograph of 78wt % W-N-Fe specimen, liquid phase sintered for 120 minute in microgravity.

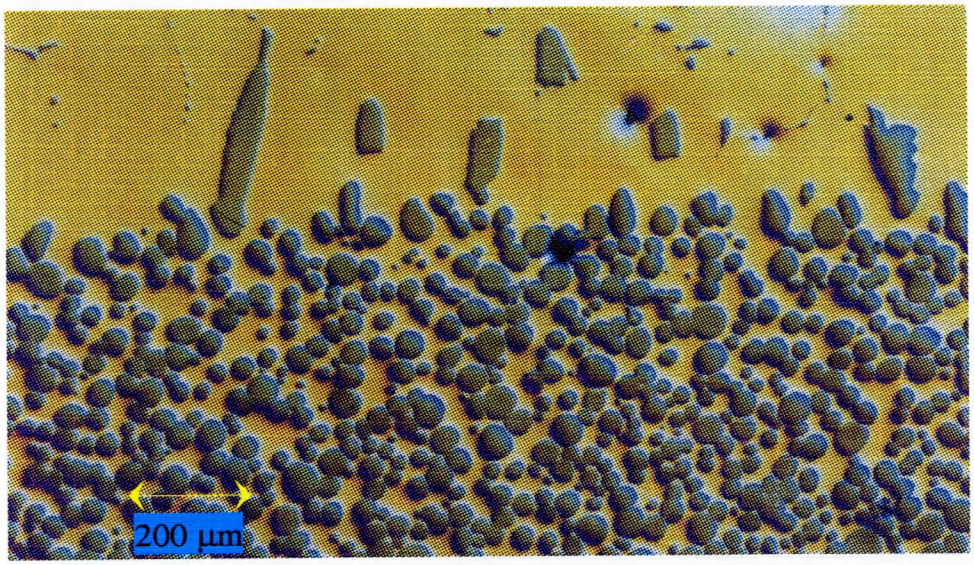

Figure 4.3 Elongated tungsten grains below the liquid dome in specimen liquid phase sintered for 120 minute in normal gravity.

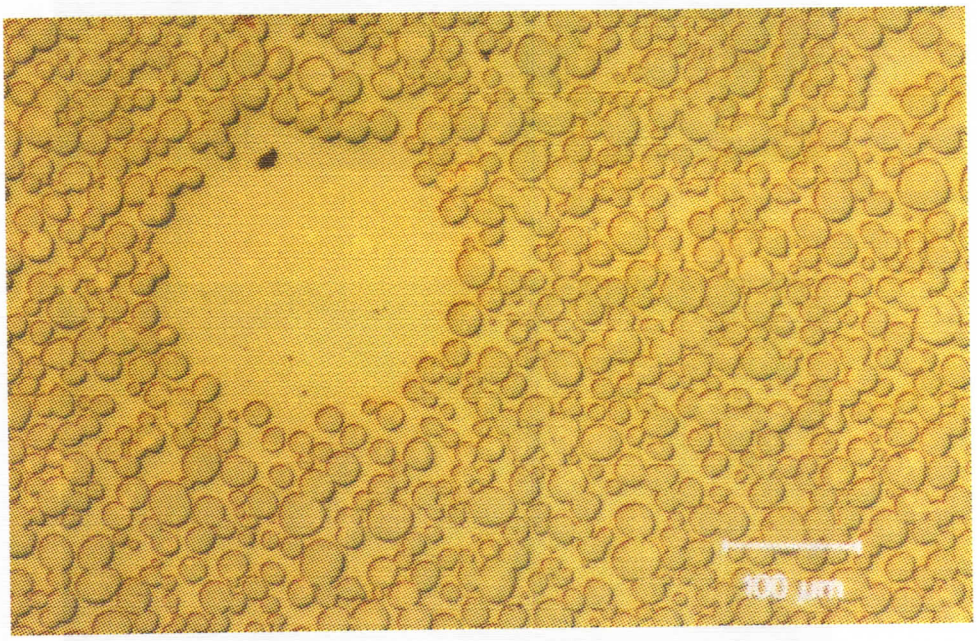

Figure 4.4 Liquid pockets in 78wt % W-N-Fe specimen, liquid phase sintered for 120 minute in (a) normal gravity and (b) microgravity.

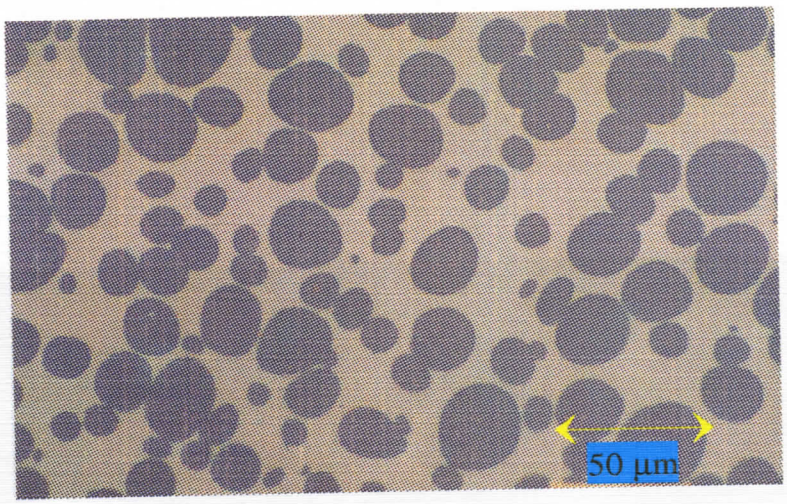

a

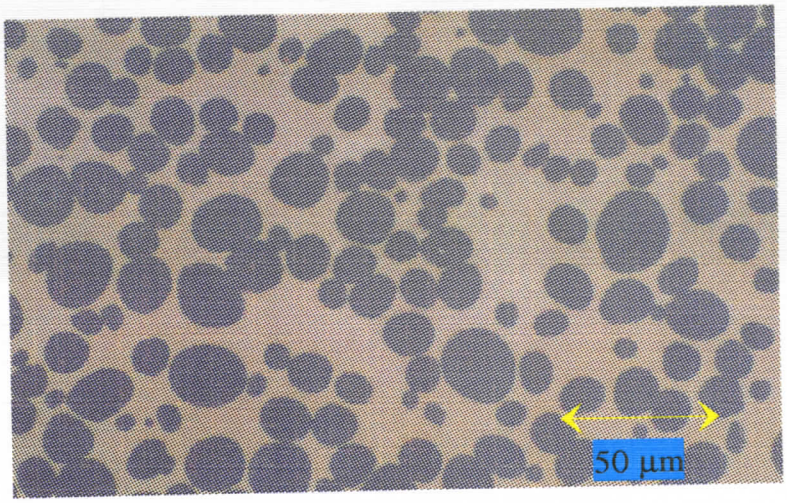

b

Figure 4.5 Typical grain shape in 83wt % W-N-Fe specimen, liquid phase sintered for 120 minute in (a) normal gravity and (b) microgravity.

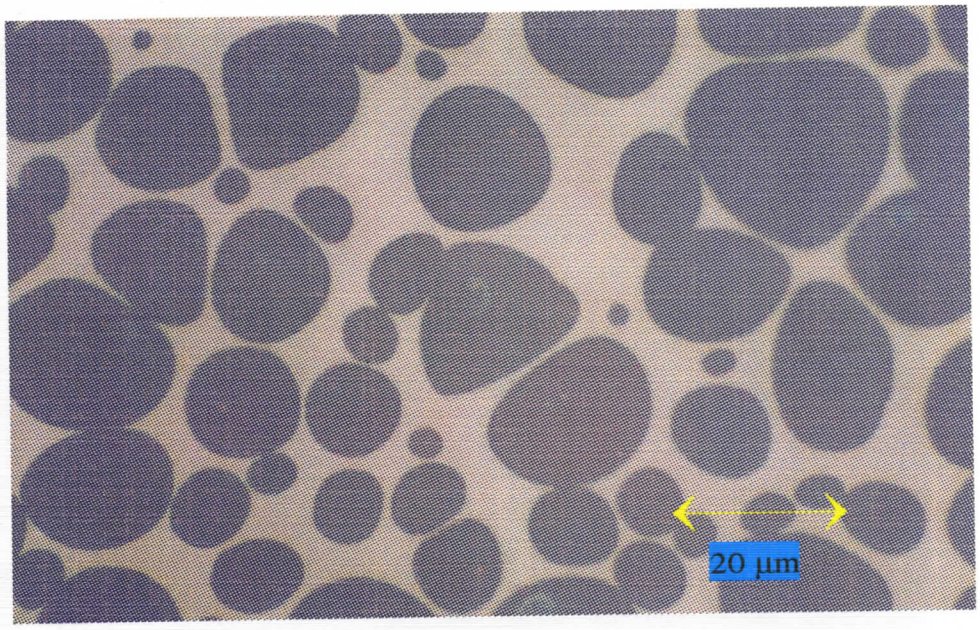

Figure 4.6 Grain shape accommodation through contact flattening in liquid phase sintered *W-N-Fe specimen*

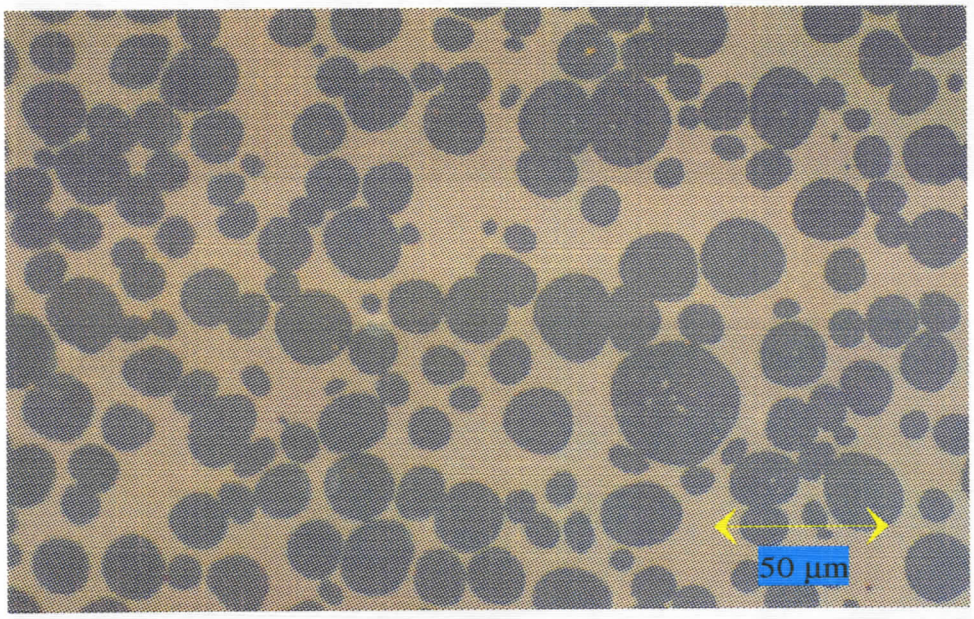

Figure 4.7 Grain shape accommodation through inter-particle neck in liquid phase sintered W-N-Fe specimen

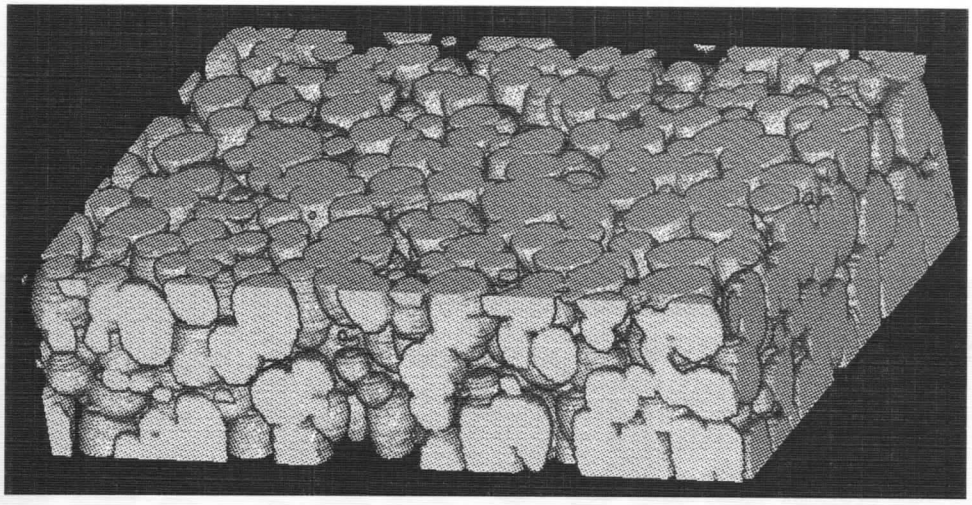

a

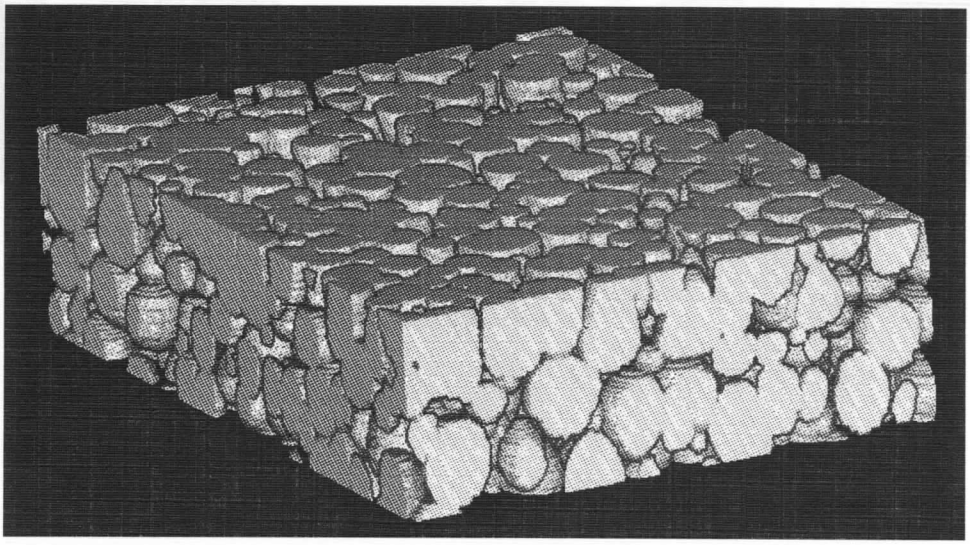

b

Figure 4.8 Two orientations of surface rendered three dimensional microstructure (reconstructed from serial sections) of 83 wt% THA liquid phase sintered in microgravity for 1 minute. The microstructure shows high topological connectivity.

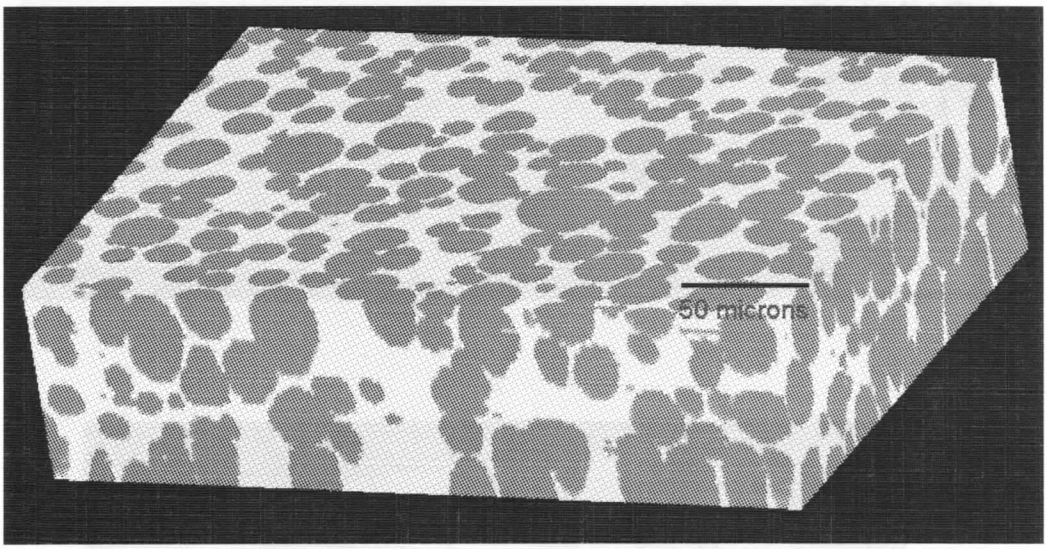

Figure 4.9 Volume rendering of the three-dimensional microstructure shown in the previous figure.

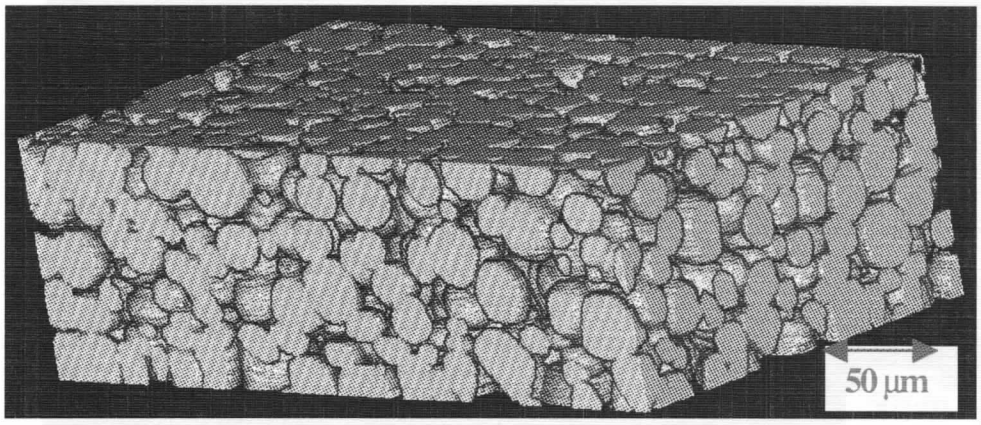

a

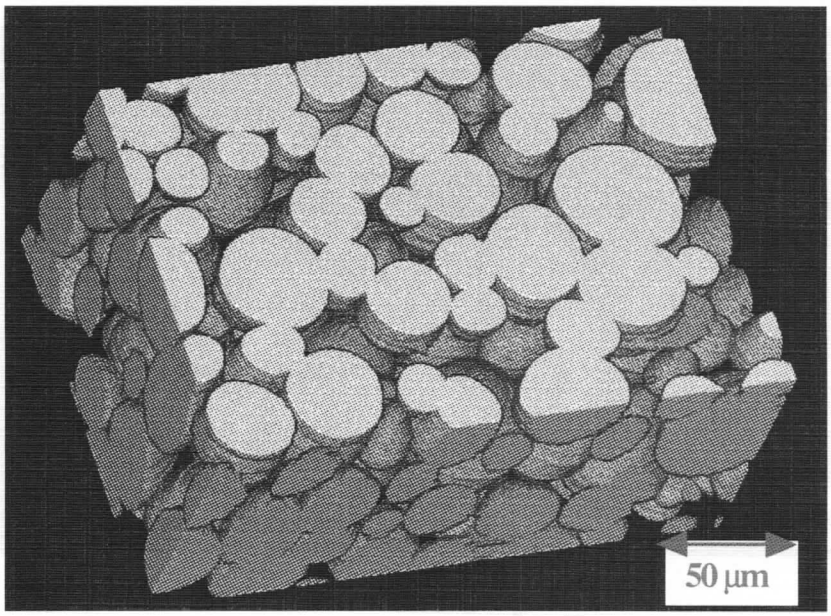

b

Figure 4.10 Visualization of coarsening of the microstructure with time for 83 wt% THA liquid phase sintered im microgravity. (a) Surface rendered microstructure for 83wt% THA sintered for 1 minute in microgravity (b) Surface rendered microstructure for 83wt% THA sintered for 120 minute in microgravity

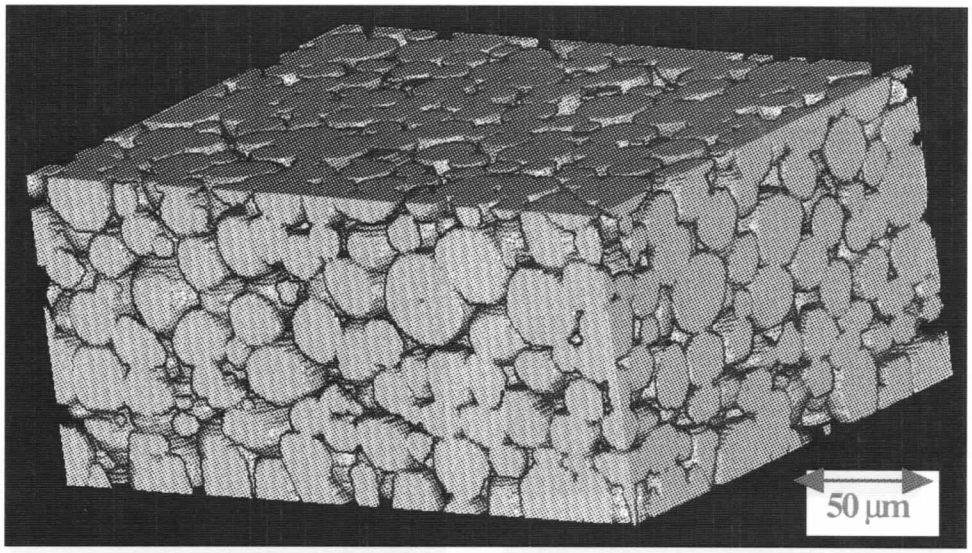

a

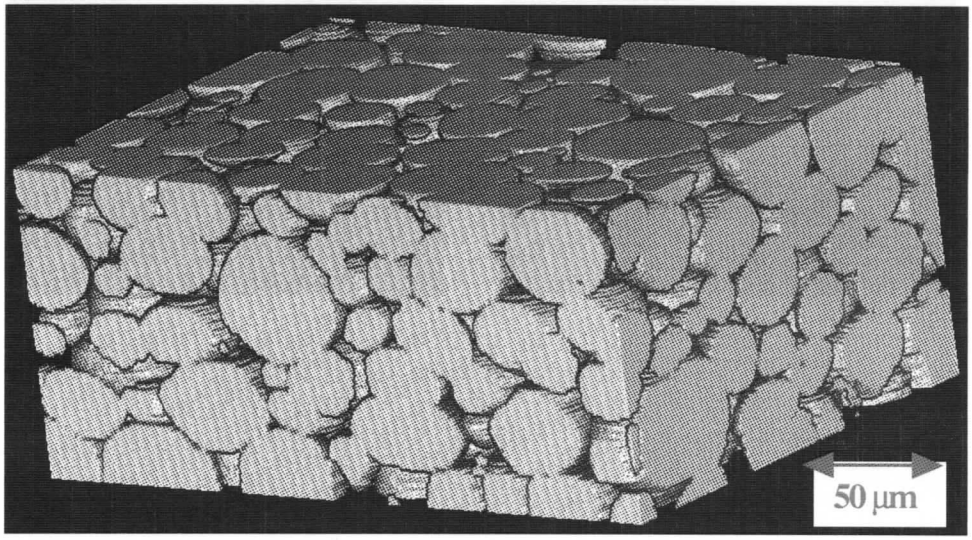

b

Figure 4.11 Visualization of coarsening of the microstructure with time for 83 wt% THA liquid phase sintered im microgravity. (a) Surface rendered microstructure for 83wt% THA sintered for 1 minute in microgravity (b) Surface rendered microstructure for 83wt% THA sintered for 120 minute in microgravity

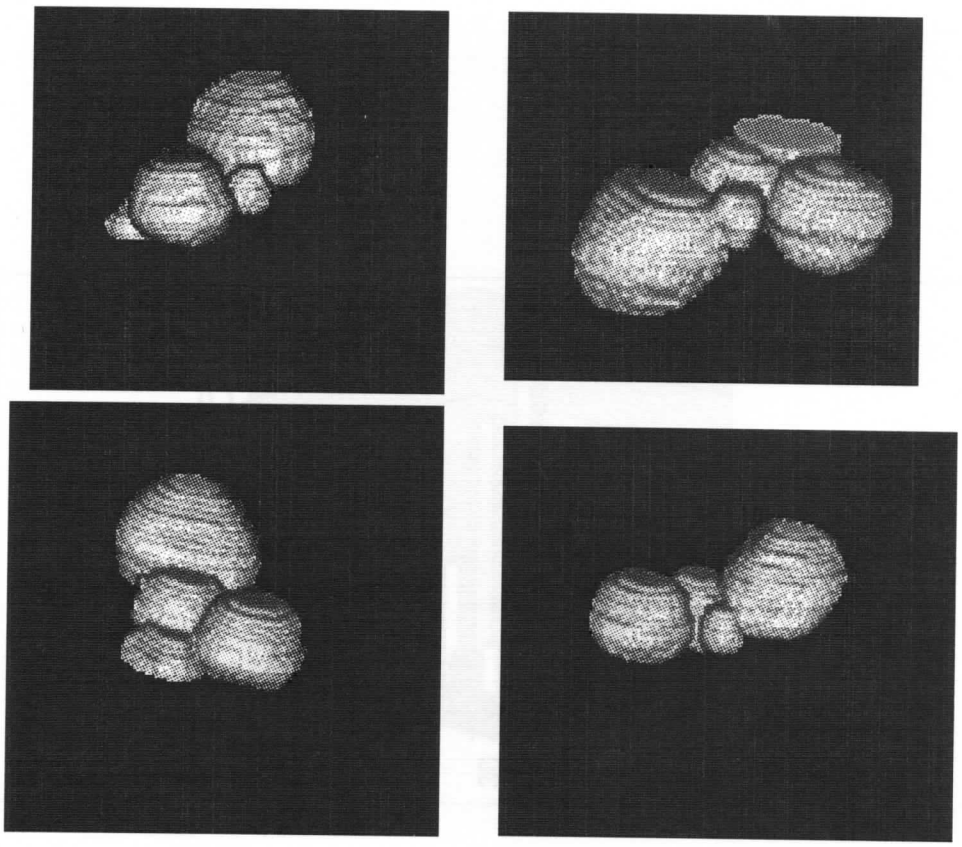

Figure 4.12 Surface rendering of a particle chain extracted from the 3D reconstruction.

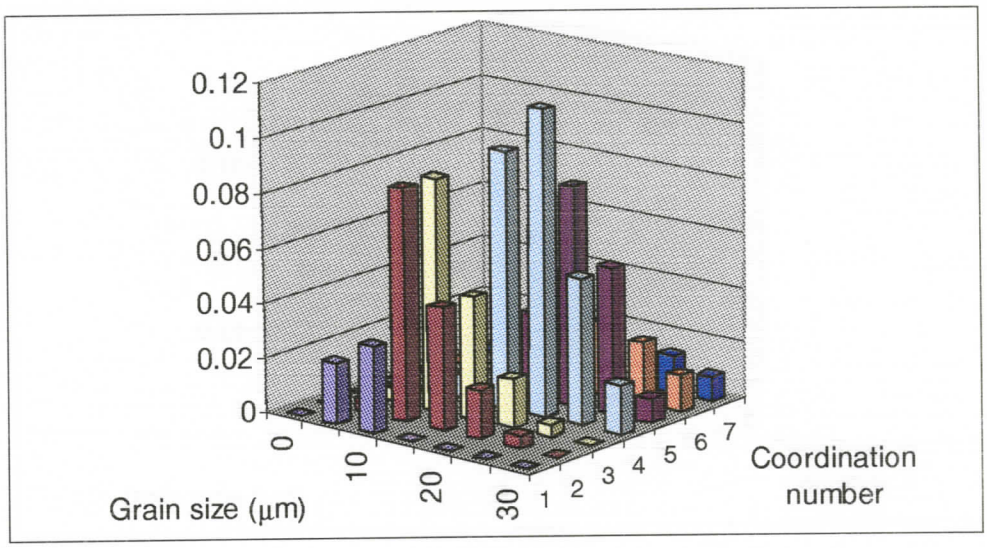

Figure 4.13 Bivariate distribution of number of inter-particle contacts in 3D and 3D size of contacting particles for 83 wt% W-Ni-Fe specimen liquid phase sintered for 1 minute in normal gravity.

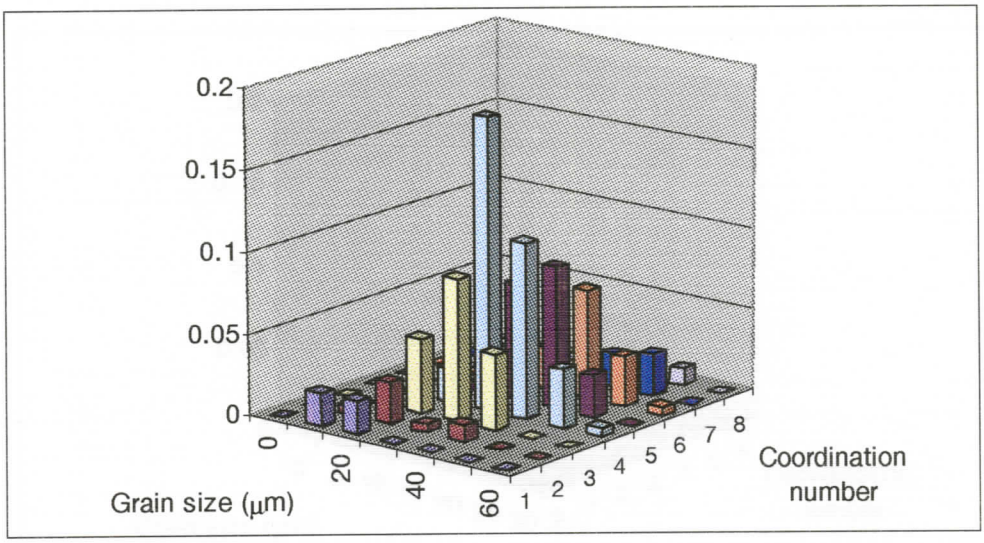

Figure 4.14 Bivariate distribution of number of inter-particle contacts in 3D and 3D size of contacting particles for 83 wt% W-Ni-Fe specimen liquid phase sintered for 1 minute in micro-gravity.

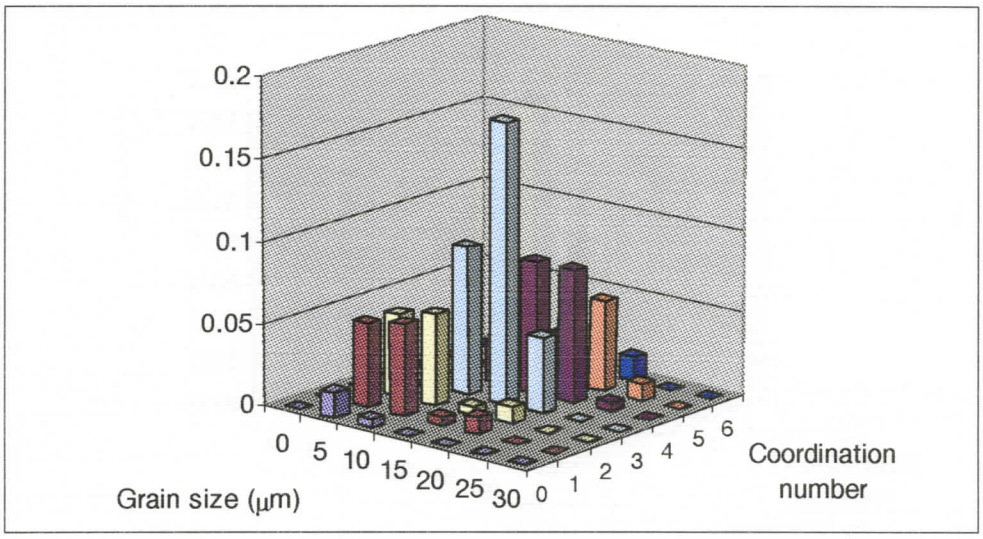

Figure 4.15 Bivariate distribution of number of inter-particle contacts in 3D and 3D size of contacting particles for 83 wt% W-Ni-Fe specimen liquid phase sintered for 120 minute in normal gravity.

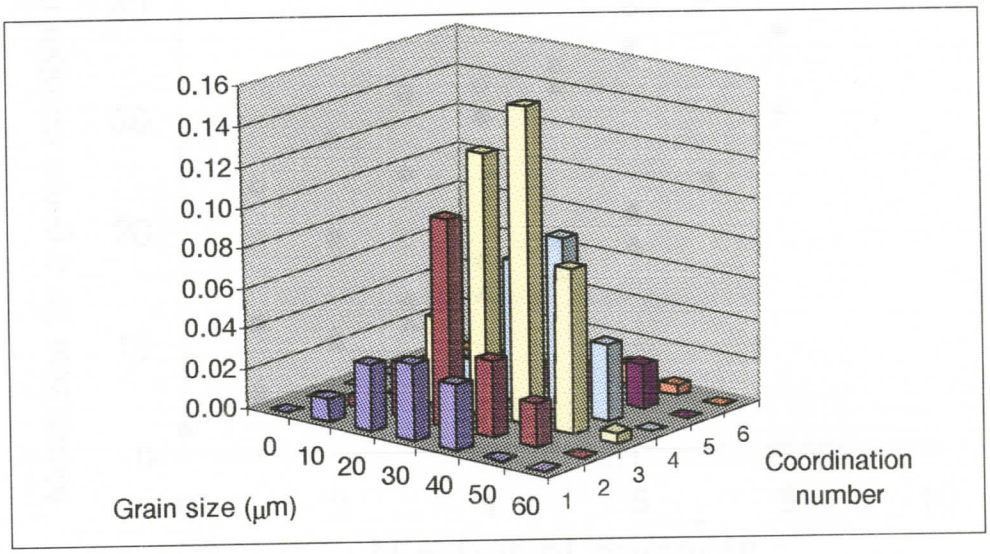

Figure 4.16 Bivariate distribution of number of inter-particle contacts in 3D and 3D size of contacting particles for 83 wt% W-Ni-Fe specimen liquid phase sintered for 120 minute in micro-gravity.

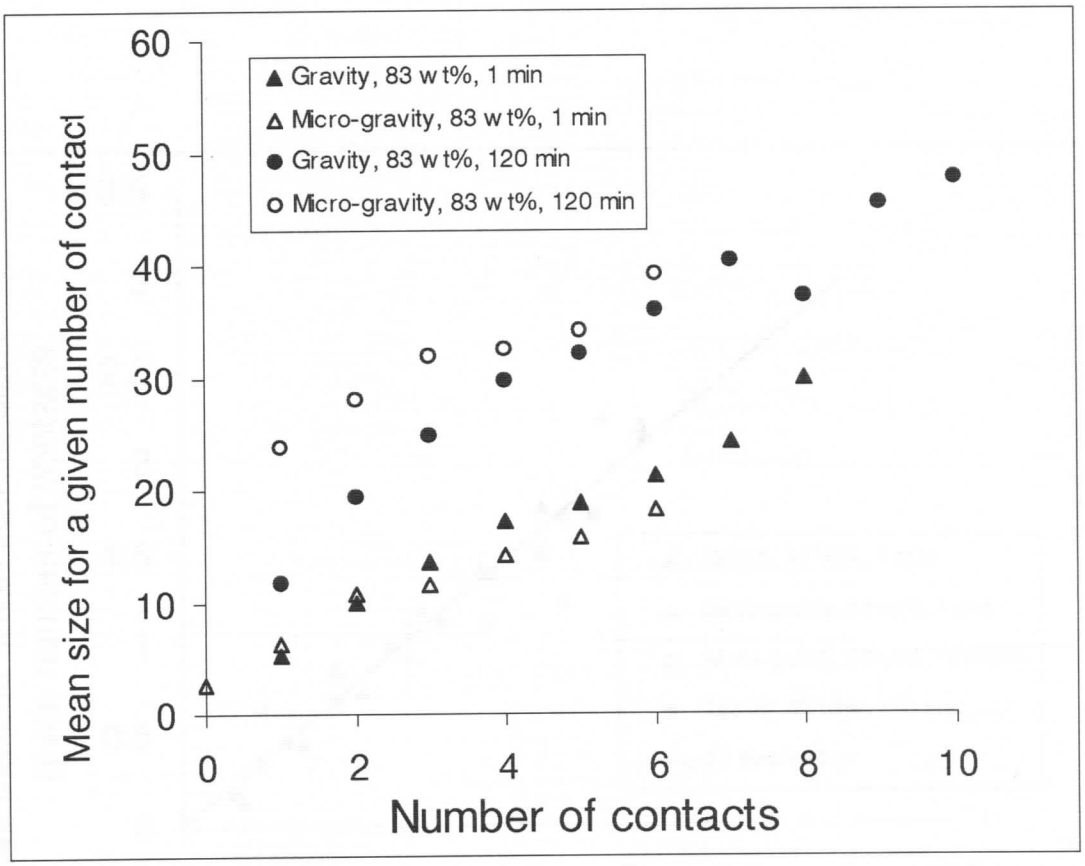

Figure 4.17 Plot of number of inter-particle contacts in 3D along the x-axis versus mean of the sizes of the particles forming those contacts.

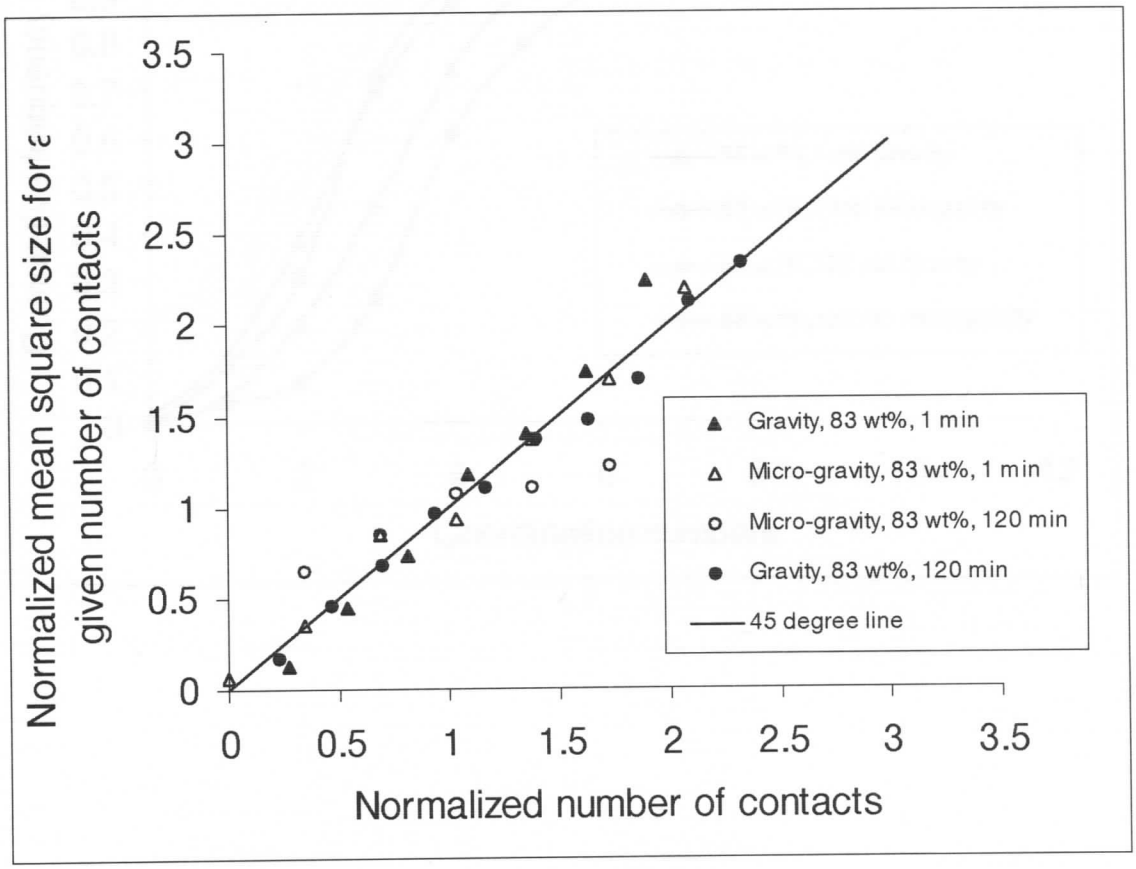

Figure 4.18 Plot of number of normalized inter-particle contacts in 3D (normalized by the mean coordination number) along the x-axis versus normalized mean of the square of the particle sizes forming those contacts (normalized by the mean square particle size).

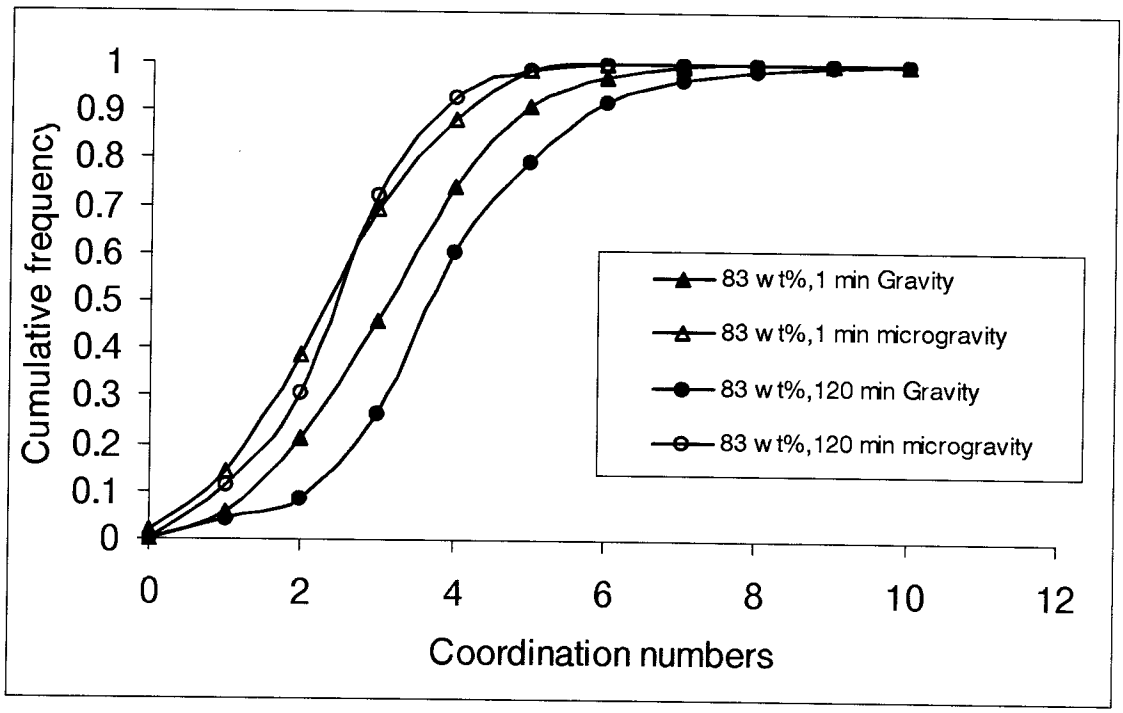

Figure 4.19 Cumulative plot of coordination number distribution in 3D for all the four 83 wt% W-Ni-Fe specimens (liquid phase sintered for 1 and 120 minutes in both normal gravity and microgravity).

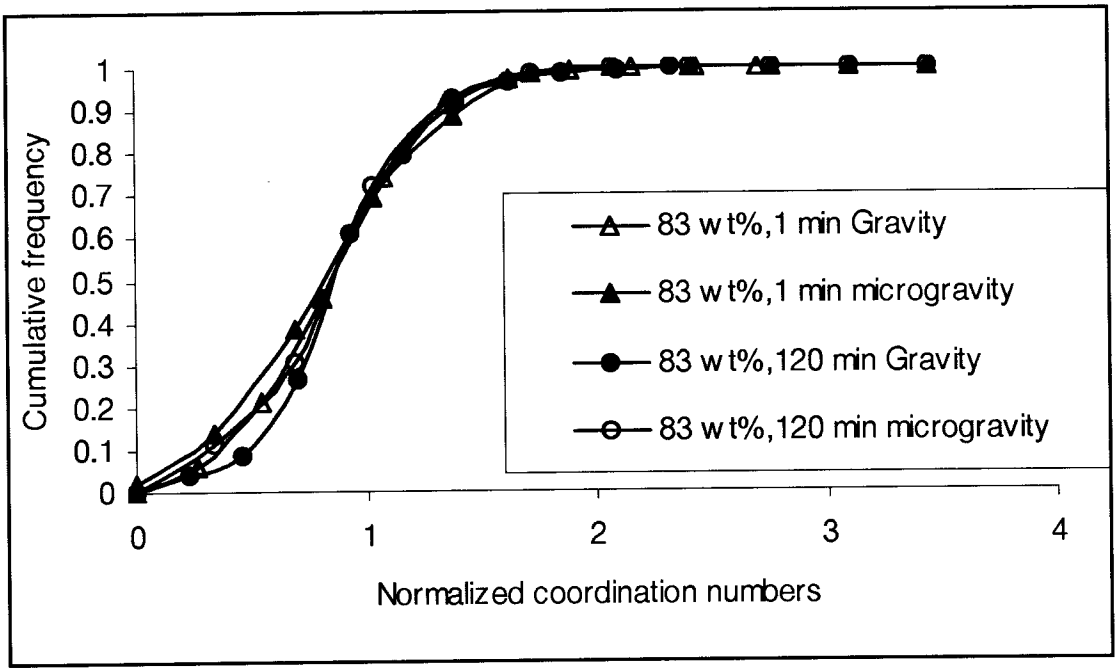

Figure 4.20 Normalized cumulative plot of coordination number distribution (normalized with corresponding mean coordination number) in 3D for all the four 83 wt% W-Ni-Fe specimens. It is seen that all the distributions, after normalization, superimpose.

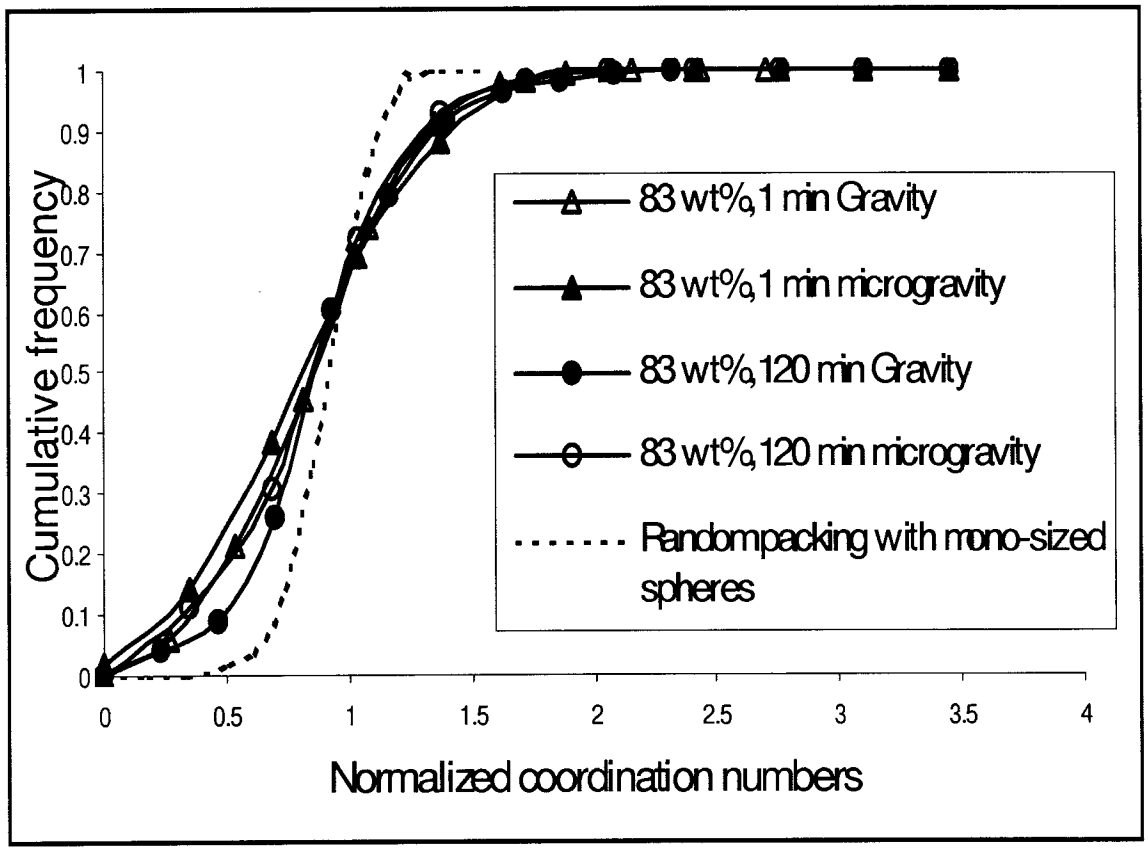

Figure 4.21 Comparison of normalized cumulative plot of Figure 4.20 with the computer simulated coordination number distribution (for a hard-core monosized spheres randomly packed in gravity). The experimental data is significantly different from the computer simulation.

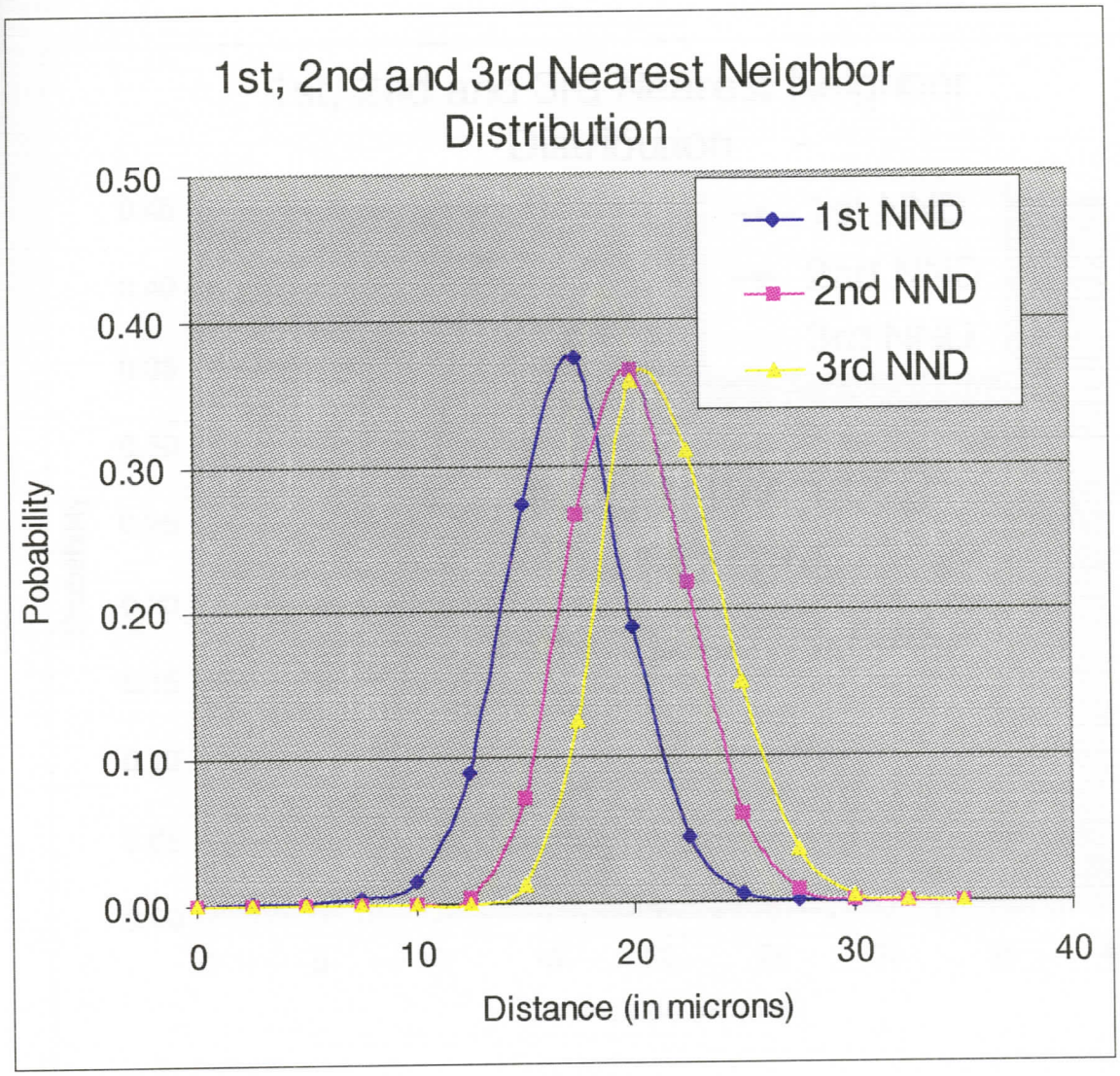

Figure 4.22 First, second and third nearest neighbor distribution function of tungsten grains in 3D for 83 wt% W-Ni-Fe specimen liquid phase sintered for 1 minute in normal gravity.

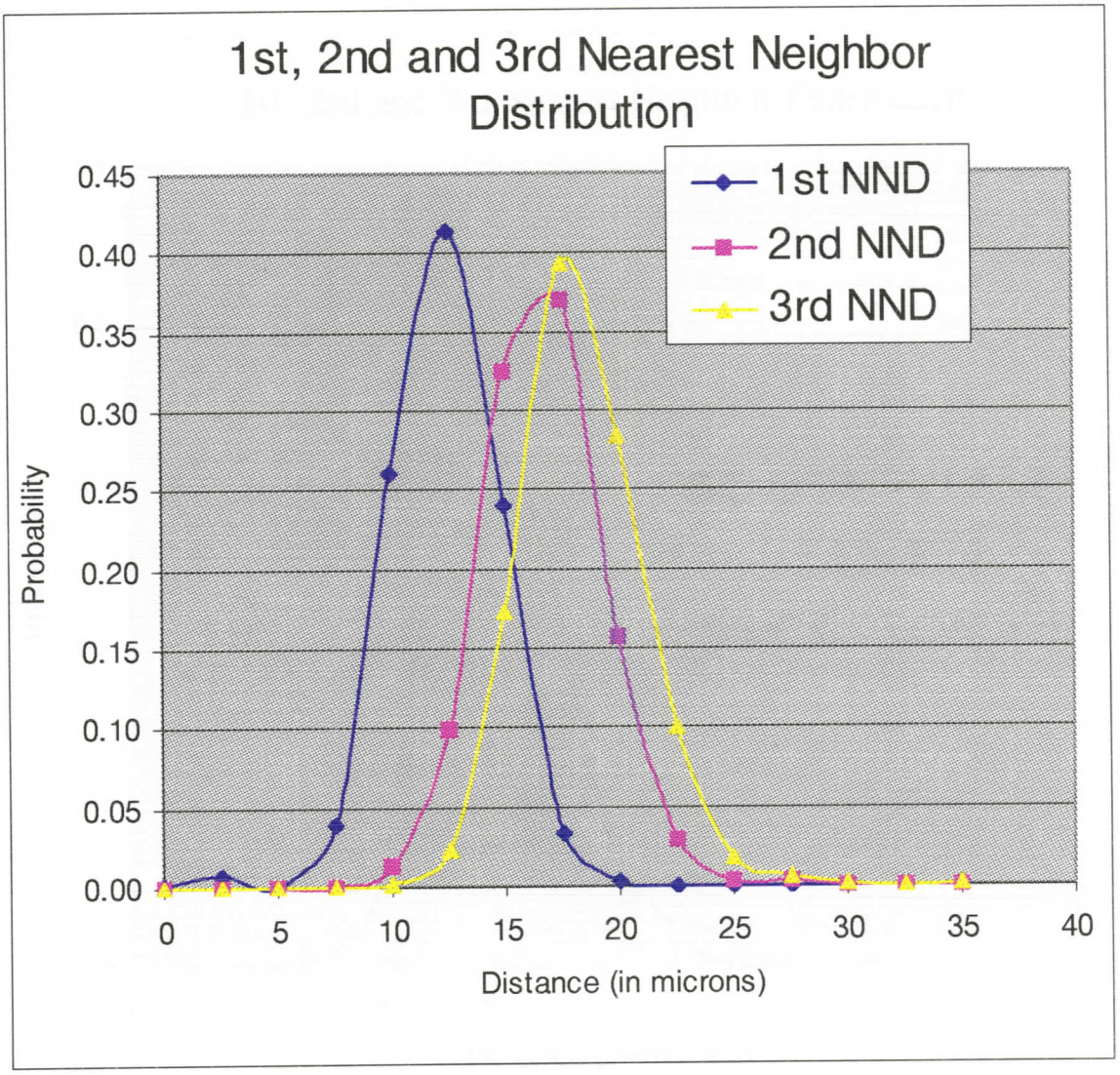

Figure 4.23 First, second and third nearest neighbor distribution function of tungsten grains in 3D for 83 wt% W-Ni-Fe specimen liquid phase sintered for 1 minute in micro-gravity.

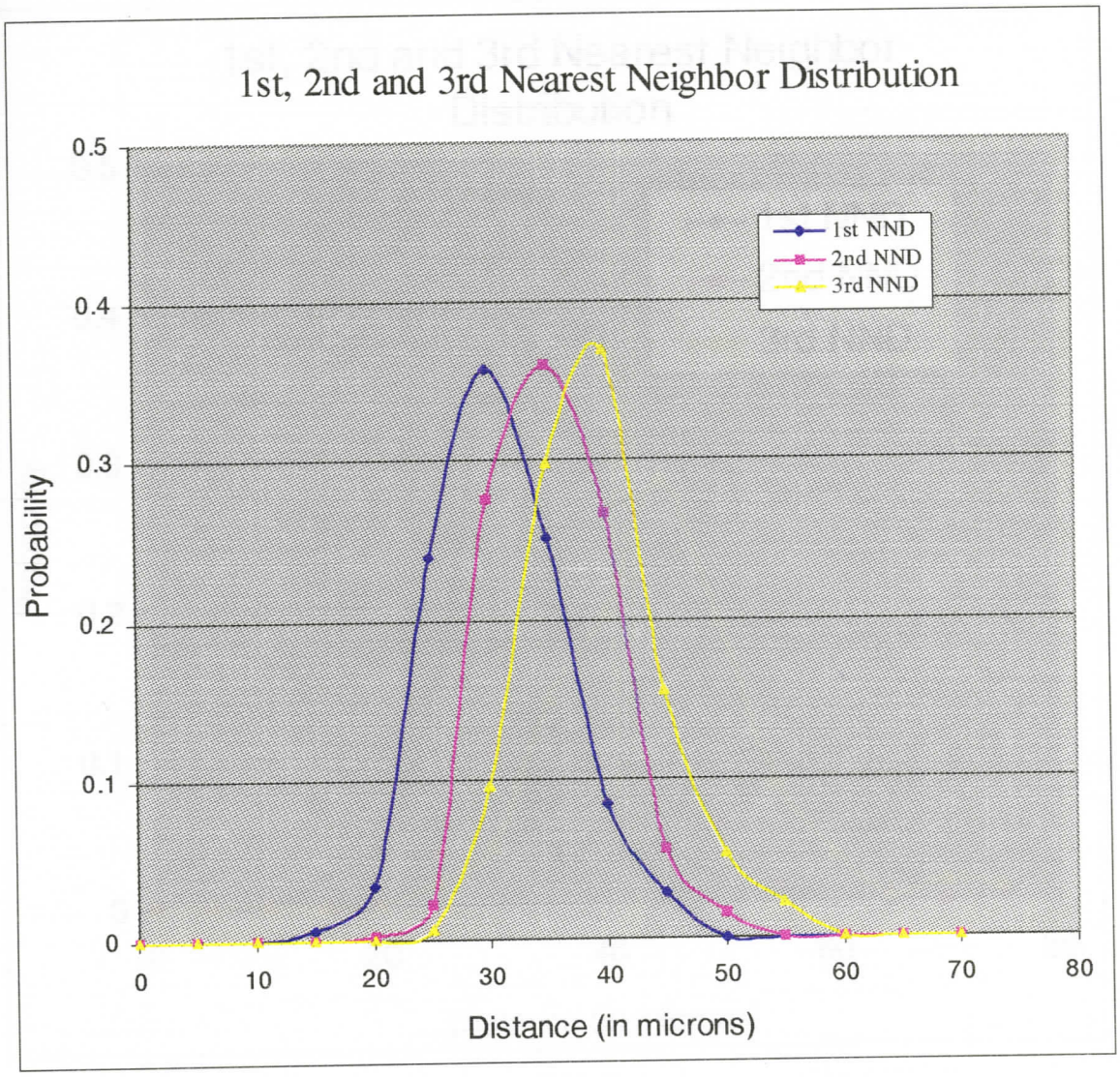

Figure 4.24 First, second and third nearest neighbor distribution function of tungsten grains in 3D for 83 wt% W-Ni-Fe specimen liquid phase sintered for 120 minute in normal gravity.

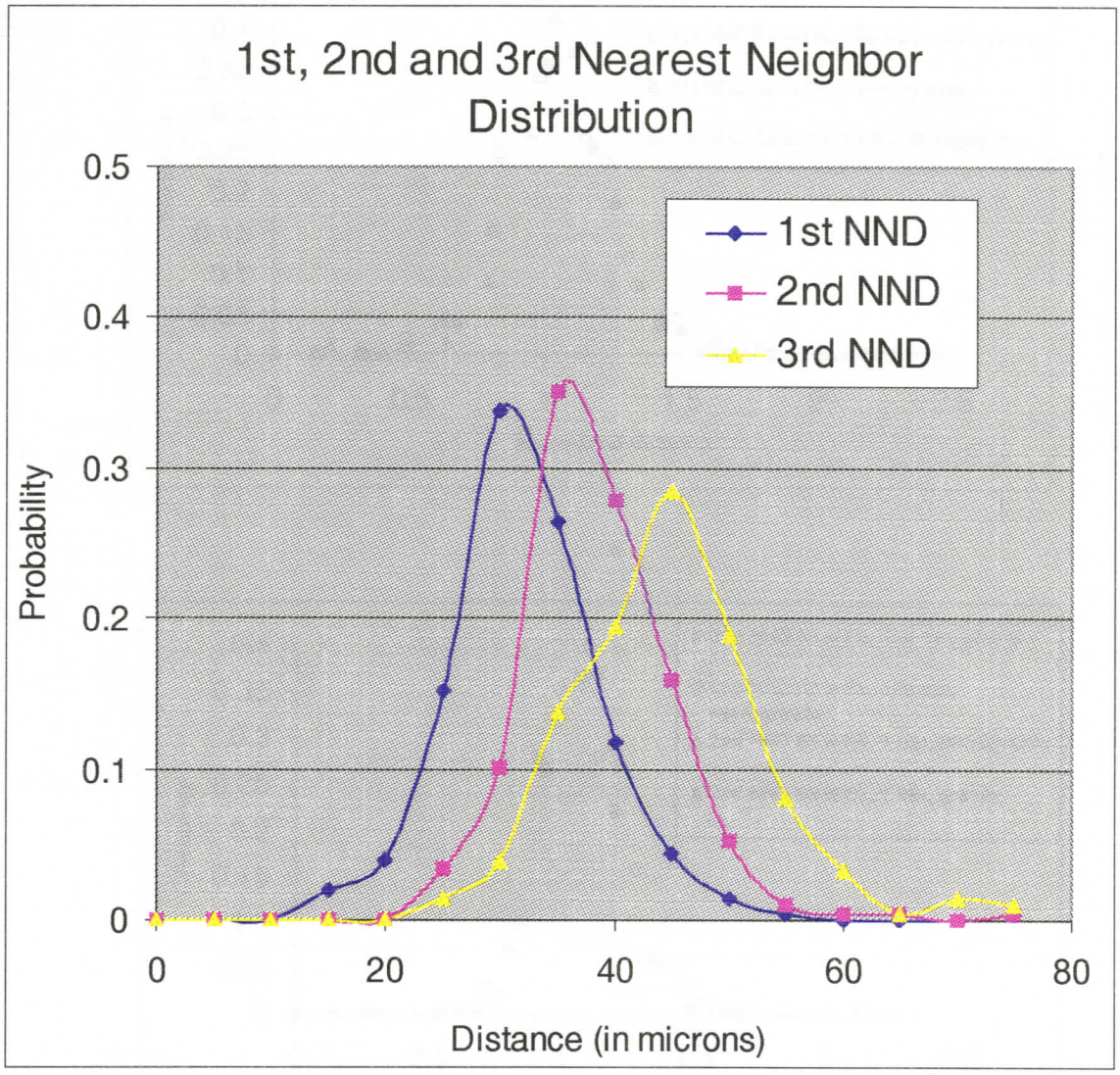

Figure 4.25 First, second and third nearest neighbor distribution function of tungsten grains in 3D for 83 wt% W-Ni-Fe specimen liquid phase sintered for 120 minute in micro-gravity.

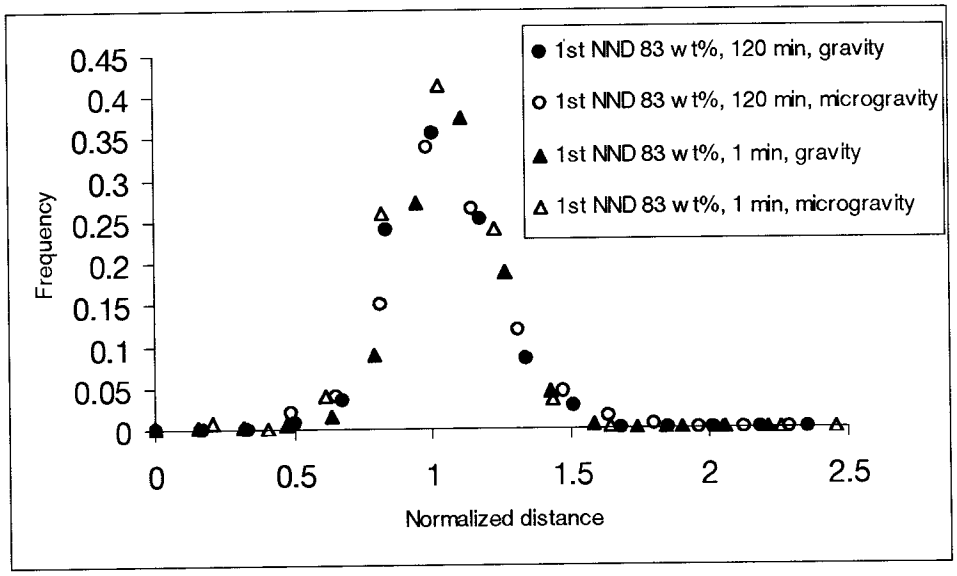

a

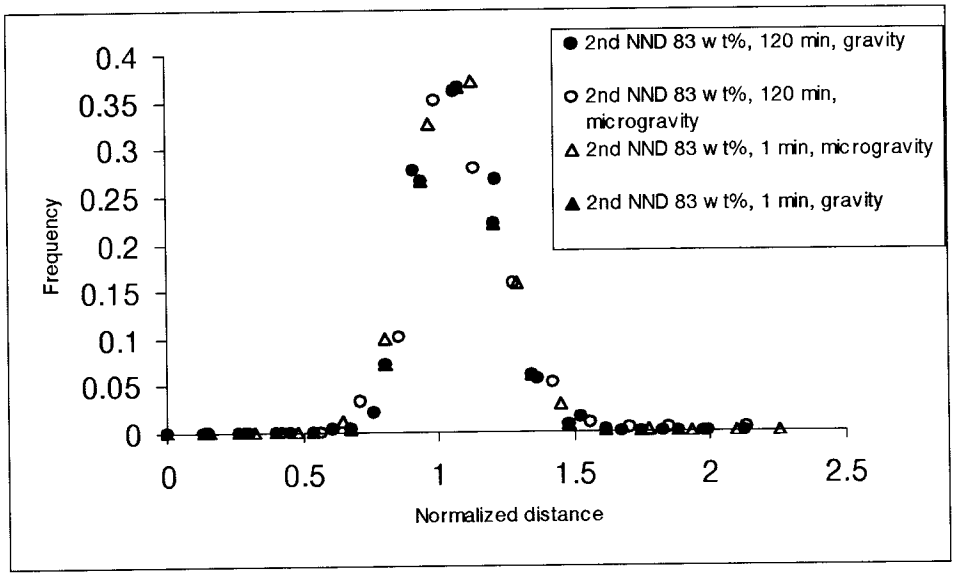

b

Figure 4.26 Normalized (a) first and (b) second nearest neighbor distribution function of tungsten grains in 3D for all the 83 wt% W-Ni-Fe specimen.

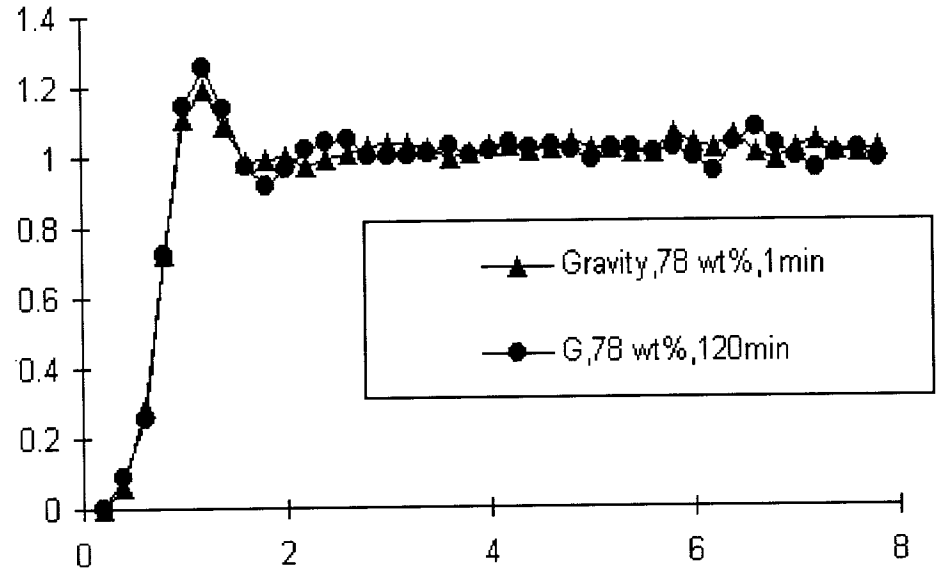

Figure 4.27 Radial distribution function of centroids of tungsten grain sections versus normalized radial distance for 78 wt% THA processed under normal gravity. The normalization is with respect to their corresponding 2D mean sizes.

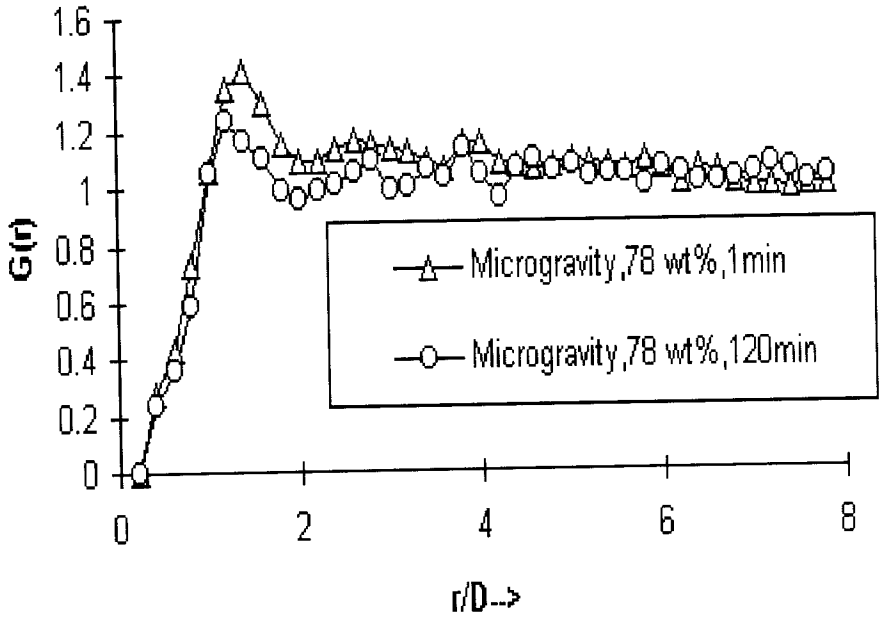

Figure 4.28 Radial distribution function of centroids of tungsten grain sections versus normalized radial distance for 78 wt% THA processed under micro-gravity. The normalization is with respect to their corresponding 2D mean sizes.

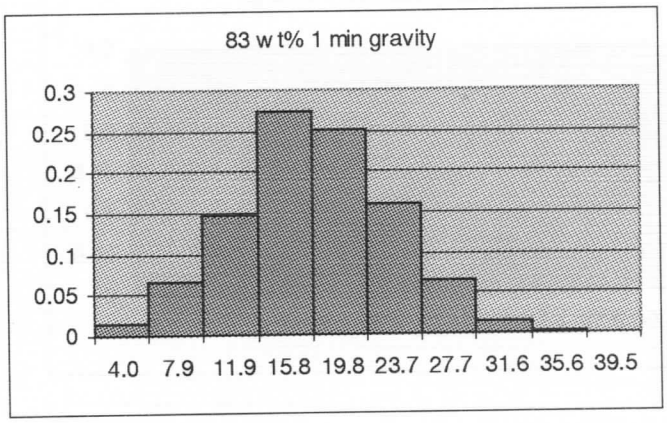

a

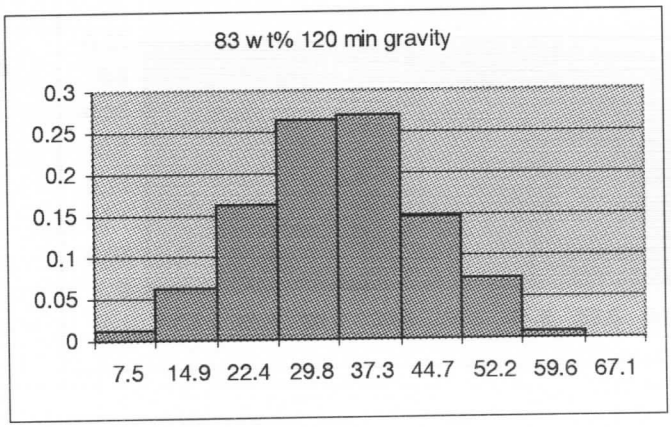

b

Figure 4.29 Three dimensional calliper diameter distribution measured in the reconstructed volume of 83 wt% THA.(a) specimen liquid phase sintered for 1 minute in normal gravity (b) specimen liquid phase sintered for 120 minute in normal gravity.

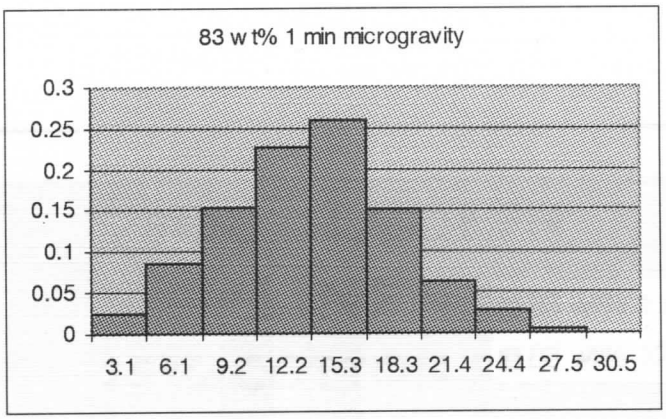

a

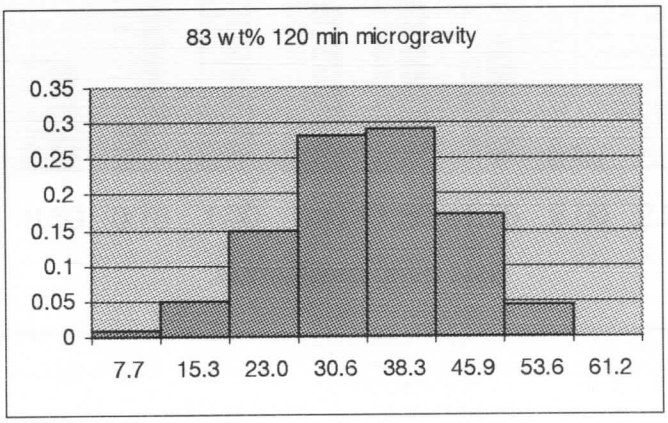

b

Figure 4.30 Three dimensional calliper diameter distribution measured in the reconstructed volume of 83 wt% THA.(a) specimen liquid phase sintered for 1 minute in micro-gravity (b) specimen liquid phase sintered for 120 minute in micro-gravity.

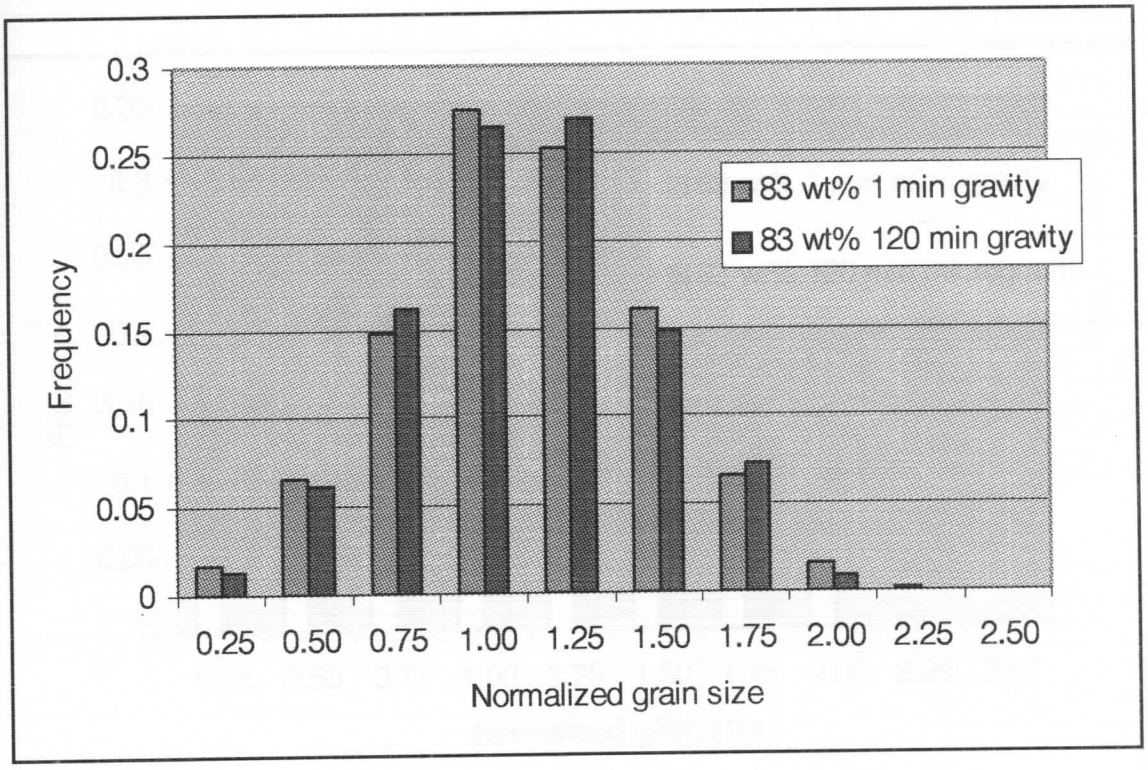

Figure 4.31 The normalized three dimensional calliper diameter distribution of 83 wt% THA. specimens liquid phase sintered for 1 minute and 120 minute under normal gravity are compared. The analysis by Chi-squared test reveals that the two distributions are similar.

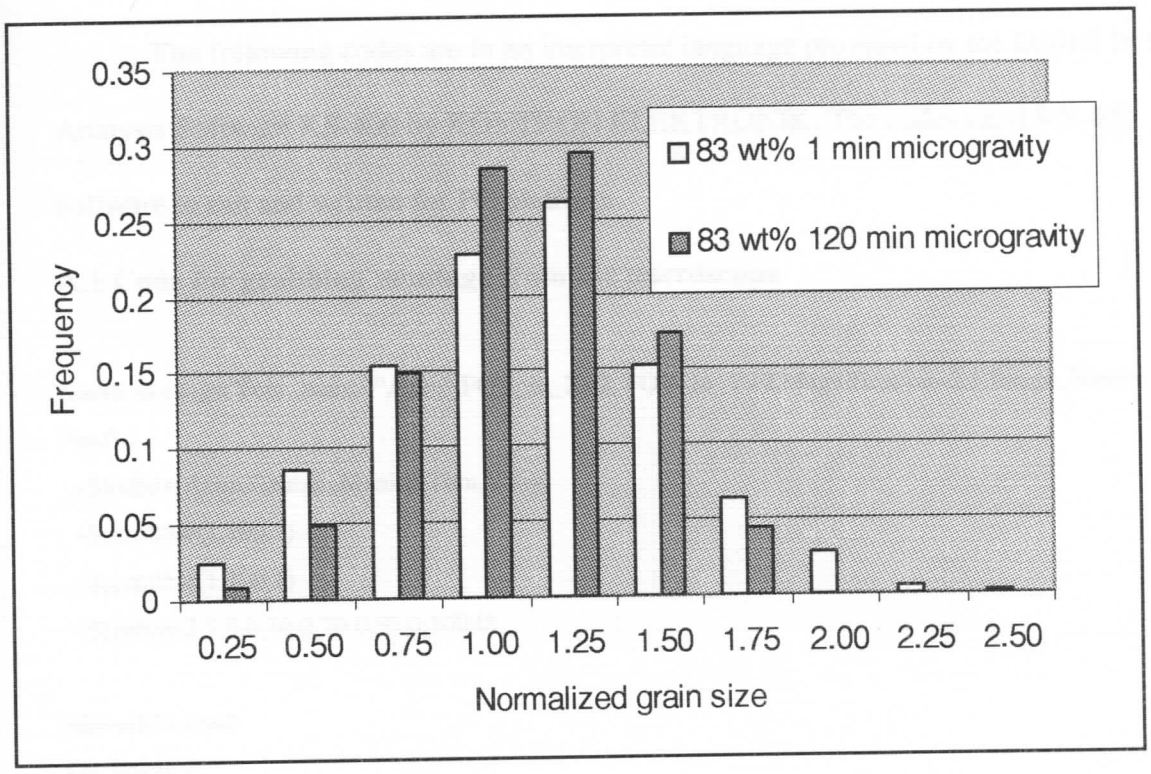

Figure 4.32 The normalized three dimensional calliper diameter distribution of 83 wt% THA. specimens liquid phase sintered for 1 minute and 120 minute in microgravity are compared. The analysis by Chi-squared test reveals that the two distributions are statistically different.

APPENDIX A

Computer codes for Digital Image analysis

The following codes are in an interpreter language provided by the Digital Image Analysis Software KS-400 by KONTRON ELEKTRONIK. The codes need KS-400 software to run and written for PC platform.

A.1 Code for grabbing montage from the microscope

```
macro montage(Your_name="Asim",FOV_in_X=2, FOV_in_Y=2,Magnification=2.5,Image_Name=
"test")
 ~$listbox(Asim,Gautam,Manish,Tom,Yang)
 ~$scrollbar(1,100,1)
 ~$scrollbar(1,100,1)
 ~$listbox(2.5,5.0,10.0,20.0,50.0,100.0)

ManualFocus=0
Set_Focus=1
Set_Home=1

write Your_name
if (Your_name=="Asim") : imgsetpath "D:\images"
if (Your_name=="Gautam") : imgsetpath "E:\Gautam\images"
if (Your_name=="Manish") : imgsetpath "E:\images"
if (Your_name=="Tom") : imgsetpath "F:\images"
if (Your_name=="Yang") : imgsetpath "G:\images"

frame_x=640
frame_y=480
overlap_x=104
```

```
overlap_y=80

Delete_img

info_x=frame_x-overlap_x
info_y=frame_y-overlap_y

mag = Magnification
if mag==100.0
        x_inc= -106.0
endif
if mag ==50.0
        x_inc= -212.0
endif
if mag ==20.0
        x_inc= -529.0
endif
if mag ==10.0
        x_inc= -1046.0
endif
if mag ==5.0
        x_inc= -2098.0
endif
if mag ==2.5
        x_inc= -3984.0
endif

x_1=(x_inc/536.0)*info_x
# Note the value of overlap is added because the x_1 value is negative
x_2=(0/480.0)*info_y

y_1=(-x_inc/536.0)*info_y
y_2=(0/512.0)*info_x
```

```
write y_1
write info_x

imgdisplay 3
tvframe 10,0,frame_x,frame_y
imgdelete "*"
STopen "asim1"
# STdefscale
# STdirections

name_img=Image_Name

if  (Set_Focus==1)
caption = "Set Focus"
text1 = "Move to focus plane"
text2 = ""
text3 = "Hit OK to continue"
STmoveint 2,4,1,caption,text1,text2,text3
endif

man_focus = ManualFocus

MCPfocusset int(800*2.5/mag)
STautofocus

if  (Set_Home==1)
caption = "Set Home position i.e. image 1_1"
text1 = "Move to the first frame, i.e. home position"
text2 = ""
text3 = "Hit OK to continue"
STmoveint 2,4,1,caption,text1,text2,text3
endif
```

```
STsethome

STsetprop "VelocityX",100*int(50/mag)
STsetprop "VelocityY",300*int(50/mag)
STsetprop "VelocityZ",100*int(50/mag)

tvinput "Stage"
imgdisplay "Stage"
xi=FOV_in_X
yi=FOV_in_Y

STclearposlist
write xi,yi

x_move = 0

z_at_y1=0
previous_z=0

for x=1; x <= xi; x = x+1
for y=1; y <= yi; y = y+1
STwait "XYZ"
STclearposlist
# write name
write x
write y

if (y==2)
STgetpos 0,0,z_at_y1,0,0
endif

STgetpos 0,0,previous_z,0,0
```

```
if (y==1)
previous_z=z_at_y1
endif

STwritepos "XYZ",int(float(x-1)*x_1+float(y-1)*x_2),int(float(y-1)*y_1+float(x-1)*y_2),previous_z,0,0,1
STmovepos 3,1
STwait "XYZA"
STmovepos 3,1
STwait "XYZA"

if (man_focus ==1)
   STmoveint 2,2,1
else
   if ( not((x==1) &&(y==1)))
      STautofocus
   endif
endif

STwait "XYZA"

imgclear "buffer",0

if ( not((x==1) &&(y==1)))

      if x_move == 1
            x_prev= x-1
            y_prev= y
            name_prev=string(x_prev)+"_"+string(y_prev)+"[1,1]"
            write "Previous Image ",name_prev
            Prev_img = name_img+name_prev+".img"
            imgload Prev_img,"Previous_img"
            wincopy "Previous_img","buffer",536,0,80,480,0,0
      else
```

```
            x_prev= x
            y_prev= y-1
            name_prev=string(x_prev)+"_"+string(y_prev)+"[1,1]"
            write "Previous Image ",name_prev
            Prev_img =name_img+name_prev+".img"
            imgload Prev_img,"Previous_img"
            wincopy "Previous_img","buffer",0,400,640,80,0,0
        endif
        imgdelete "Previous_img"
        write "Calling Manual Match Macro"
        Manual_match "buffer[1,1]"
endif

name=string(x)+"_"+string(y)+"[1,1]"
tvinput name
imgdisplay name
out_name = name_img+name+".img"
imgsave name,out_name
imgdelete name
write out_name
x_move=0
endfor
x_move=1
endfor

endmacro
##########################################################################
macro Manual_match(Image_name="char")
tvinput "AS_ref[1,1]"

imgcopy Image_name,"AS_ref[1,2]"
imgcopy Image_name,"AS_ref[1,3]"
imgdisplay "AS_ref[1]"
```

```
# STautofocus
STwait "XYZA"

x_pos=y_pos=z_pos=0

STclearposlist

while 1
STgetpos x_pos,y_pos,z_pos,0,0
# write "x = ",x_pos,"    y = ", y_pos,"    z = ", z_pos

z_change=0
read move

if move == 9
z_pos = z_pos +5
endif

if move == 99
z_pos = z_pos +25
endif
if move == 999
z_pos = z_pos +50
endif
if move == 9999
z_pos = z_pos +75
endif

if move == 3
z_pos = z_pos +5
endif

if move == 33
```

```
z_pos = z_pos -25
endif
if move == 333
z_pos = z_pos -50
endif
if move == 3333
z_pos = z_pos -75
endif

if move == 6
x_pos = x_pos +1
endif

if move == 66
x_pos = x_pos +5
endif
if move == 666
x_pos = x_pos +25
endif
if move == 6666
x_pos = x_pos +45
endif

if move == 4
x_pos = x_pos -1
endif
if move == 44
x_pos = x_pos -5
endif
if move == 444
x_pos = x_pos -25
endif
if move == 4444
```

```
x_pos = x_pos -45
endif

if move == 8
y_pos = y_pos +1
endif

if move == 88
y_pos = y_pos + 5
endif
if move == 888
y_pos = y_pos + 25
endif
if move == 8888
y_pos = y_pos + 45
endif

if move == 2
y_pos = y_pos - 1
endif

if move == 22
y_pos = y_pos - 5
endif
if move == 222
y_pos = y_pos -25
endif
if move == 2222
y_pos = y_pos -45
endif

if move == 5
break
```

```
endif

if move == 55
STautofocus
STwaitpos
STgetpos x_pos,y_pos,z_pos,0,0
z_change=1
endif

if move == 555
STmoveint 2,4,1
STwaitpos
STgetpos x_pos,y_pos,z_pos,0,0
z_change=1
endif

move := int(move)

 write "x = ",x_pos,"    y = ", y_pos,"    z = ", z_pos
STwritepos "XYZ",x_pos,y_pos,z_pos,0,0,1
# STwritepos "XYZ",-211,-1,-149,0,0,0
STmovepos 3,1
STwait "XYZA"
STselmove 3,1,-1,0,"XYZ"
STwaitpos
STmovepos 3,1

# STautofocus
STwait "XYZA"

tvinput "AS_ref[1,1]"
imgdisplay "AS_ref[1]"
```

```
STgetpos x_pos,y_pos,z_pos,0,0
# write "x = ",x_pos,"    y = ", y_pos,"    z = ", z_pos

endwhile

imgcopy "AS_ref[1,1]",Image_name

endmacro
##########################################################################
```

A.2 Code for creating montage from grabbed images

```
macro View_all(Image_name="char",xfov=2,yfov=2)

imgnew "Composite",536*xfov,400*yfov,1,"Grey"
imgdisplay "Composite"

for x=1, x<=xfov, x= x+1
for y=1, y<=yfov,y= y+1
present_image = Image_name+string(x)+"_"+string(y)
write present_image
imgload present_image+".img","PI"
wincopy "PI","Composite",0,0,563,400,536*(x-1),400*(y-1)
endfor
endfor

endmacro
##########################################################################

macro View_partial(Image_name="nnd",x_start=1,x_end=3,y_start=1,y_end=3)

imgnew "Composite",536*(x_end-x_start+1),400*(y_end-y_start+1),1,"Grey"
```

```
imgdisplay "Composite"

x_pos=1

for x=x_start, x<=x_end, x= x+1
y_pos=1
for y=y_start, y<=y_end,y= y+1
present_image = Image_name+string(x)+"_"+string(y)
write present_image
imgload present_image+".img","PI"
wincopy "PI","Composite",0,0,563,400,536*(x_pos-1),400*(y_pos-1)
y_pos=y_pos+1
endfor
x_pos=x_pos+1
endfor

endmacro
##########################################################################
```

A.3 Code for performing generic 2D measurements

```
macro measure_montage (name_img="char",path="c:/asim",xi=2,yi=2,mag=2.5)

showwindow "Display",0
### START OF MEASUREMENT #######
###vvvvvvvvvvvvvvvvvvvvvvvvv#######
Delete_img

DB1= name_img+"_R"
DB2 = name_img+"_F"

write DB1,"    ",DB2
```

```
DBdelete DB1
DBnew DB1,7
DBsetcolumn DB1,1,"CGRAVX","Float","micron"
DBsetcolumn DB1,2,"CGRAVY","Float","micron"
DBsetcolumn DB1,3,"PERIM","Float","micron"
DBsetcolumn DB1,4,"DCIRCLE","Float","micron"
DBsetcolumn DB1,5,"FERETMAX","Float","micron"
DBsetcolumn DB1,6,"FERETMIN","Float","micron"
DBsetcolumn DB1,7,"ANGLEFMAX","Float","deg"

DBnew DB2,2
DBsetcolumn DB2,1,"FLDCOUNT","Float","none"
DBsetcolumn DB2,2,"FLDAREAP","Float","%"

if (mag==2.5 )
MSload "c:/library/micros~1/axiove~1/asim_2_5"
endif

if (mag==5.0)
MSload "c:/library/micros~1/axiove~1/asim_5"
endif


if (mag==10.0)
MSload "c:/library/micros~1/axiove~1/asim_10"
endif

if (mag==20.0)
MSload "c:/library/micros~1/axiove~1/asim_20"
endif

if (mag==50.0)
MSload "c:/library/micros~1/axiove~1/asim_50"
```

```
endif

if (mag==100.0)
MSload "c:/library/micros~1/axiove~1/asim_100"
endif


if (mag==4.0)
MSload "c:/library/micros~1/oldinv~1/asim_4"
endif


if (mag==8.0)
MSload "c:/library/micros~1/oldinv~1/asim_8"
endif


if (mag==16.0)
MSload "c:/library/micros~1/oldinv~1/asim_16"
endif


if (mag==40.0)
MSload "c:/library/micros~1/oldinv~1/asim_40"
endif

if (mag==80.0)
MSload "c:/library/micros~1/oldinv~1/asim_80"
endif


low=0
```

```
high=255

min_scrap=0
max_scrap=0
min_fill=0
max_fill=0

First_img=1

######## Region Specific Measurement
for  x=0;x<2*xi-1;x=x+1
for  y=0;y<2*yi-1;y=y+1
   Cut_paste path+"/"+name_img,x,y

   imgdisplay 6
   seldisplay "Display"
   Grectg 186,140,268,200,6,2
   Grectg 52,40,536,400,6,0
   Grectg 52,40,536,400,6,0

      if (First_img==1)
            Is_this_OK=0
            while (Is_this_OK==0)
                  !dislev 6,5,low,high,1
                  write low
                  write high
                  !binscrap 5,5,min_scrap,max_scrap,0
                  binnot 5,5
                  !binscrap 5,5,min_fill,max_fill,0
                  binnot 5,5
                  imgdisplay 5
                  read Is_this_OK
            endwhile
```

```
        First_img=0
    else
        dislev 6,5,low,high,1
        binscrap 5,5,min_scrap,max_scrap,0
        binnot 5,5
        binscrap 5,5,min_fill,max_fill,0
        binnot 5,5
    endif

RGnew 5,6
stat=1
RGfirstregion
stat=_STATUS
while stat==1
    MSmeasregion 1
    RGnextregion
    stat=_STATUS
    MSgetvalue "CGRAVX",t1
    MSgetvalue "CGRAVY",t2
    MSgetvalue "PERIM",t3
    MSgetvalue "DCIRCLE",t4
    MSgetvalue "FERETMAX",t5
    MSgetvalue "FERETMIN",t6
    MSgetvalue "ANGLEFMAX",t7

    # pause
    newt1=x*268+t1
    newt2=y*200+t2
    DBaddline DB1
    DBsetvalue DB1,1,newt1
    DBsetvalue DB1,2,newt2
    DBsetvalue DB1,3,t3
    DBsetvalue DB1,4,t4
```

```
      DBsetvalue DB1,5,t5
      DBsetvalue DB1,6,t6
      DBsetvalue DB1,7,t7
    endwhile

endfor
endfor

if (mag==2.5)
MSload "c:/library/micros~1/axiove~1/a_f_2_5"
endif

if (mag==5.0)
MSload "c:/library/micros~1/axiove~1/a_f_5"
endif

if (mag==10.0)
MSload "c:/library/micros~1/axiove~1/a_f_10"
endif

if (mag==20.0)
MSload "c:/library/micros~1/axiove~1/a_f_20"
endif


if (mag==50.0)
MSload "c:/library/micros~1/axiove~1/a_f_50"
endif


if (mag==100.0)
MSload "c:/library/micros~1/axiove~1/a_f_100"
endif
```

```
if (mag==4.0)
MSload "c:/library/micros~1/oldinv~1/a_f_4"
endif


if (mag==8.0)
MSload "c:/library/micros~1/oldinv~1/a_f_8"
endif


if (mag==16.0)
MSload "c:/library/micros~1/oldinv~1/a_f_16"
endif


if (mag==40.0)
MSload "c:/library/micros~1/oldinv~1/a_f_40"
endif

if (mag==80.0)
MSload "c:/library/micros~1/oldinv~1/a_f_80"
endif




######## Field Specific Measurement
for  x=1;x<=xi;x=x+1
for  y=1;y<=yi;y=y+1

        name=string(x)+"_"+string(y)
        in_name = path+"/"+name_img+name+".img"
```

```
        imgload in_name,6
        # imgdisplay 6

        dislev 6,5,low,high,1
          binscrap 5,5,min_scrap,max_scrap,0
          binnot 5,5
          binscrap 5,5,min_fill,max_fill,0
          binnot 5,5

        RGnew 5,6
        MSmeasmask 5,6,DB2,1,2,10
endfor
endfor

datalist DB1,0,0
datalist DB2,0,0
endmacro
##########################################################################
```

A.4 Code for performing serial section

```
section_no=2

read section_no

pre = section_no

if (section_no != 1)
pre = section_no -1
endif

STopen "ASIM1"
STmoveint 1,4,1
```

```
########## B A S E  1 ###############
pause "CHANGE THE MAGNIFICATION TO 20X"
if (section_no != 1)
imgload "d:\\images\\base1_"+string(pre)+".img","b1"
Manual_match "b1"
else
STmoveint 1,4,1
endif

tvinput 1
imgdisplay 1
imgcopy "1[1,1]","b1"
imgsave "b1","d:\\images\\base1_"+string(section_no)+".img"
imgdelete "b1"
imgdelete 1

STsethome
STwritepos "XYZ",5602,12748,-1861,0,0,1
STmovepos 3,1
STwaitpos


####### S A M P L E 38_78 ##########
sample_id="38_78"

if (section_no != 1)
imgload "d:\\images\\"+sample_id+"b1_"+string(pre)+".img","b1"
Manual_match "b1"
else
STmoveint 1,4,1
endif

tvinput 1
```

```
imgdisplay 1
imgcopy "1[1,1]","b1"
imgsave "b1","d:\\images\\"+sample_id+"b1_"+string(section_no)+".img"
imgdelete "b1"
imgdelete 1

montage "Asim",1,2,20.0,sample_id+"b2"+string(section_no)
montage "Asim",3,3,20.0,sample_id+string(section_no)



STwritepos "XYZ",-17364,4529,-1999,0,0,1
STmovepos 3,1
STwaitpos

####### S A M P L E 5_83 ##########
sample_id="5_83"

if (section_no != 1)
imgload "d:\\images\\"+sample_id+"b1_"+string(pre)+".img","b1"
Manual_match "b1"
else
STmoveint 1,4,1
endif

tvinput 1
imgdisplay 1
imgcopy "1[1,1]","b1"
imgsave "b1","d:\\images\\"+sample_id+"b1_"+string(section_no)+".img"
imgdelete "b1"
imgdelete 1


montage "Asim",1,2,20.0,sample_id+"b2"+string(section_no)
```

```
montage "Asim",3,3,20.0,sample_id+string(section_no)


STwritepos "XYZ",-17781,-17534,2357,0,0,1
STmovepos 3,1
STwaitpos


####### S A M P L E 15_80 ##########
sample_id="15_80"

if (section_no != 1)
imgload "d:\\images\\"+sample_id+"b1_"+string(pre)+".img","b1"
Manual_match "b1"
else
STmoveint 1,4,1
endif

tvinput 1
imgdisplay 1
imgcopy "1[1,1]","b1"
imgsave "b1","d:\\images\\"+sample_id+"b1_"+string(section_no)+".img"
imgdelete "b1"
imgdelete 1

montage "Asim",1,2,20.0,sample_id+"b2"+string(section_no)
montage "Asim",5,5,20.0,sample_id+string(section_no)



STwritepos "XYZ",15982,-18005,5298,0,0,1
STmovepos 3,1
STwaitpos
```

```
####### S A M P L E 15_75 ##########
sample_id="15_75"

if (section_no != 1)
imgload "d:\\images\\"+sample_id+"b1_"+string(pre)+".img","b1"
Manual_match "b1"
else
STmoveint 1,4,1
endif

tvinput 1
imgdisplay 1
imgcopy "1[1,1]","b1"
imgsave "b1","d:\\images\\"+sample_id+"b1_"+string(section_no)+".img"
imgdelete "b1"
imgdelete 1

montage "Asim",1,2,20.0,sample_id+"b2"+string(section_no)
montage "Asim",5,5,20.0,sample_id+string(section_no)

STwritepos "XYZ",2503,-10933,1635,0,0,1
STmovepos 3,1
STwaitpos


########### B A S E 2 ###############

if (section_no != 1)
imgload "d:\\images\\base2_"+string(pre)+".img","b2"
Manual_match "b2"
else
STmoveint 1,4,1
endif
```

```
tvinput 1
imgdisplay 1
imgcopy "1[1,1]","b2"
imgsave "b2","d:\\images\\base2_"+string(section_no)+".img"
imgdelete "b2"
imgdelete 1


STsethome
STwritepos "XYZ",18609,7932,-1679,0,0,1
STmovepos 3,1
STwaitpos


########## B A S E 3 ###############
pause "CHANGE THE MAGNIFICATION TO 20X"

if (section_no != 1)
imgload "d:\\images\\base3_"+string(pre)+".img","b3"
Manual_match "b3"
else
STmoveint 1,4,1
endif

tvinput 1
imgdisplay 1
imgcopy "1[1,1]","b3"
imgsave "b3","d:\\images\\base3_"+string(section_no)+".img"
imgdelete "b3"
imgdelete 1

STsethome
STwritepos "XYZ",-2929,10966,-852,0,0,1
```

```
STmovepos 3,1
STwaitpos



####### S A M P L E 23_76 ##########
sample_id="23_76"

if (section_no != 1)
imgload "d:\\images\\"+sample_id+"b1_"+string(pre)+".img","b1"
Manual_match "b1"
else
STmoveint 1,4,1
endif

tvinput 1
imgdisplay 1
imgcopy "1[1,1]","b1"
imgsave "b1","d:\\images\\"+sample_id+"b1_"+string(section_no)+".img"
imgdelete "b1"
imgdelete 1

montage "Asim",1,2,20.0,sample_id+"b2"+string(section_no)
montage "Asim",3,3,20.0,sample_id+string(section_no)
#########################################################################
```

A.5 Code for performing disector measurements and measuring calliper diameter on serial sections

```
## This macro is for measuring the coordinates of top and bot of particles
imgdelete "*"
```

```
Gclear 0

imgname=""
DBname:=""

start_sect=30
no_of_sect=50  #number of sections in buffer
end_sect=30+start_sect
Last_sect=90
read start_sect

fact=(1) # and
 read imgname
DBname=imgname+string(start_sect)
DBdelete DBname
DBnew DBname,7
DBsetcolumn DBname,1,"S.No.","Int","<none>"
DBsetcolumn DBname,2,"topx","float","<none>"
DBsetcolumn DBname,3,"topy","float","<none>"
DBsetcolumn DBname,4,"topz","float","<none>"
DBsetcolumn DBname,5,"botx","float","<none>"
DBsetcolumn DBname,6,"boty","float","<none>"
DBsetcolumn DBname,7,"botz","float","<none>"

for i=start_sect; i <= start_sect+no_of_sect; i = i+1
   imgload "c:\\sections\\"+imgname+string(i)+".tif",i
endfor

Gclear 0

imgnew "a",804,600,1,"Colour"
imgnew "b",804,600,1,"Grey"
imgclear "b",0
```

```
# imgcopy 1,"a[1,1]"
# imgcopy 2,"a[1,2]"
# imgcopy 2,"a[1,3]"

x=y=z=0
point =1
i=2
particle_no=1



ijk=start_sect
while (ijk<=end_sect)

    inc=0
    incx=0
    incy=0
    First=1
    Ref_sect=ijk
    lookup_sect=ijk+1
    i=lookup_sect

  while (inc!=11)
      imgcopy Ref_sect,"a[1,1]"
      imgcopy i,"a[1,2]"
      imgcopy i,"a[1,3]"
      imgdisplay "a[1]"

      # read inc
      ! Gpixel incx,incy,0

if (First==1)
x=incx*fact
```

```
y=incy*fact
First=0
endif

if (abs(x/fact-incx)>abs(y/fact-incy))
inc=1
endif

if (abs(x/fact-incx)<abs(y/fact-incy))
inc=-1
endif

dist= ((x/fact-incx)*(x/fact-incx)+(y/fact-incy)*(y/fact-incy) )

if (dist<225)
inc=0
endif

if ( (incx>0) and  (point==1))
inc=0
endif

if ( incx<0)
inc=11
endif

 write "dist = ",dist

        if (inc==0)
            if (point==1)
                write "Click the top"
                # ! Gpixel x,y,0
                x=incx
```

```
            y=incy
            Gcircle x,y,1,1
            Gstring x,y,string(particle_no),10,"SWV___8",0
            x=fact*x # this is because of 0.5 zoom
            y=fact*y
            write "x= ",x,"   y= ",y,"   z= ",i
            DBaddline DBname

            DBsetvalue DBname,"S.No.",particle_no

            DBsetvalue DBname,"topx",x
            DBsetvalue DBname,"topy",y
            DBsetvalue DBname,"topz",i
            point =point+1
            inc=1
            incx=incx+350

      endif
endif

if (inc==0)
      if (point==2)
            write "Click the bot"
            # ! Gpixel x,y,0
            x=incx
            y=incy
            Gcircle x,y,1,9
            # Gstring x,y,string(particle_no),10,"SWV___5",0
            x=fact*x  #this is because of 0.5 zoom
            y=fact*y
            write "x= ",x,"   y= ",y,"   z= ",i
            DBsetvalue DBname,"botx",x
            DBsetvalue DBname,"boty",y
```

```
            DBsetvalue DBname,"botz",i
            point =point+1
            inc=0
        endif
    endif


        if (point==3)
            point =1
            particle_no= particle_no+1
            i=lookup_sect
        endif


    if (inc!=0)
        if (  (( i+inc)<=Ref_sect+no_of_sect-1)    and (i+inc) >= Ref_sect)
            i=i+inc
            write "i = ",i, "    inc = ", inc, "   particle = ",particle_no
        endif
    endif



endwhile

    imgnew "c",804,600,1,"Grey" #
    imgnew "d",804,600,1,"Grey" #
    imgclear "c",0          # This keeps only the last
    imgclear "d",0          # graphics.
    Gmerge "c",255          #
    subtract "c","b","d",1  #
    imgcopy "d","b"         #
    Gclear 0                #
```

```
        Gextract "b",250,255,14   #
        imgdelete "c"
        imgdelete "d"

        write "DISECTOR #", ijk
        imgdelete ijk
        ijk=ijk+1
        imgload "c:\\sections\\"+imgname+string(ijk+no_of_sect)+".tif",(ijk+no_of_sect)
        write (ijk+no_of_sect)
  endwhile
```

A.6 Code for performing coordination number count on serial sections

```
## This macro reads the coordinates of top and bot of particles
## and lets you count the number of necks, and writes it to the output
## along with the top and bottom coordinate

imgdelete "*"
Gclear 0

imgname="n1575"
DBname:=""

start_sect=30
no_of_sect=50  #number of sections in buffer
read start_sect

            # this fact is 1/0.5 for 3x3 montage
fact=(1) # and
            # 1/0.3 for 5x5 montage

read imgname
DBname=imgname+"sn"+string(start_sect)
DBname1=imgname+string(start_sect)
```

```
DBdelete DBname
DBnew DBname,7
DBsetcolumn DBname,1,"No.ofcontacts","Int","<none>"
DBsetcolumn DBname,2,"topx","float","<none>"
DBsetcolumn DBname,3,"topy","float","<none>"
DBsetcolumn DBname,4,"topz","float","<none>"
DBsetcolumn DBname,5,"botx","float","<none>"
DBsetcolumn DBname,6,"boty","float","<none>"
DBsetcolumn DBname,7,"botz","float","<none>"


for i=start_sect; i <= start_sect+no_of_sect; i = i+1
   imgload "c:\\sections\\"+imgname+string(i)+".tif",i
endfor

ex=0
i:=1
j:=1
DBfirstline DBname1

while (ex !=1)
DBgetvalue DBname1,"S.No.",sn_num
DBgetvalue DBname1,"topx",topx
DBgetvalue DBname1,"topy",topy
DBgetvalue DBname1,"topz",topz
DBgetvalue DBname1,"botx",botx
DBgetvalue DBname1,"boty",boty
DBgetvalue DBname1,"botz",botz
inc =1
pre_img=int(topz)-1
imgdisplay pre_img
Gcircle int(topx/fact),int(topy/fact),35,11,0
Gcircle int(topx/fact),int(topy/fact),1,12,0
```

```
# Gstring int(topx/fact),int(topy/fact),string(sn_num),10,"SWV___8",0
write sn_num
j=int(botz-topz)+2

contacts =-1
while (contacts <0)
   for (i=1; i<=j;i=i+1)
      pause
      pre_img=pre_img+inc
      imgdisplay pre_img
   endfor
   inc=inc*(-1)
   pause
 Gcircle int(topx/fact),int(topy/fact),35,12,0
   read contacts
 Gcircle int(topx/fact),int(topy/fact),35,11,0
 endwhile
 Gcircle int(topx/fact),int(topy/fact),35,0,0

 DBaddline DBname
 DBsetvalue DBname,"No.ofcontacts",contacts
 DBsetvalue DBname,"topx",topx
 DBsetvalue DBname,"topy",topy
 DBsetvalue DBname,"topz",topz
 DBsetvalue DBname,"botx",botx
 DBsetvalue DBname,"boty",boty
 DBsetvalue DBname,"botz",botz
 DBnextline DBname1

 # read ex
 endwhile
 ##########################################################################
```

APPENDIX B

Computer code for Transformations and spatial distribution calculations

The following codes have been written in C and MS Visual Basic (5.0) languages. The C codes are so written that they are platform independent and only need an ANSI C compiler. The Visual Basic code can be only run on IBM PCs or on any machine which supports MS Excel 5.0 or higher.

B.1 Code for generation of 2D nearest neighbor distribution from data on centroid

```
/*************************************************************************/
/*   Program to calculate nearest neighbor distribution function     */
/*************************************************************************/

#include <stdio.h>
#include <math.h>
#include <stdlib.h>

/*****************************************/
/*          constant definition          */
/*****************************************/
#define PI 3.1415926

float  x[3000], y[3000], d[3000];

double distance(double x1, double y1, double x0, double y0)
{
  double dist;
  double sqrt();

  dist=sqrt((x1-x0)*(x1-x0)+(y1-y0)*(y1-y0));
  return(dist);
}


void main()
{
```

```
char InputFile[50],OutputFile[50],buffer[100];
int i, j, k;
int totalnumber;
float start, dr,buf;
double fabs(),dave[12], dmin[12];
double dist;
int num[40][50];

FILE *indata;
FILE *outdata1;

printf("\n\n\n\n\tThe Input File name is: ");
scanf("%s", &InputFile[0]);
printf("\n\tThe Output File name is: ");
scanf("%s", OutputFile);

printf("\n\n\n\tInput the number of objects:");
scanf("%d", &totalnumber);
printf("\n\tInput the minmum nearest neighbor distance and the gap:");
scanf("%f%f", &start, &dr);


for(j=0;j<11;j++)
 { dave[j]=0;
 for(i=0; i<31; i++)
  num[j][i]=0;}

if((indata=fopen(InputFile,"r"))==NULL)
  {printf("cannot open this file\n");
   exit(0); }
 if((outdata1=fopen(OutputFile, "w"))==NULL)
   {
     printf("cannot open this file\n");
     exit(0);
   }
 for(i=0; i<totalnumber; i++)
 {
  fscanf(indata,"%f%f%f%f",&buf,&x[i],&y[i],&d[i]);
  fgets(buffer,99,indata);
```

```
 }

/* begin of nearest neighbor distribution function calculation */

for(i=0; i<totalnumber;)
  {
    for(j=0; j<11;j++)
     dmin[j]=1000;
    for(j=0; j<totalnumber;)
     {
      if(fabs(x[j]-x[i])>dmin[10]||fabs(y[j]-y[i])>dmin[10])
        {
          j++;
        }
     else
       {
        dist=distance(x[j], y[j], x[i], y[i]);
         if(dist==0)
          {
            j++;
           }
         else
          if(dist<=dmin[0])
          { dmin[0]=dist;
           j++;
          }
         else
            if(dist<=dmin[1])
               { dmin[1]=dist;
                 j++;
               }
             else
               if(dist<=dmin[2])
                 {dmin[2]=dist;
                  j++;
                 }
                else
                  if(dist<=dmin[3])
                   {dmin[3]=dist;
```

```
    j++;
   }
 else
   if(dist<=dmin[4])
    {dmin[4]=dist;
     j++;
    }
   else
     if(dist<=dmin[5])
      {dmin[5]=dist;
            j++;
      }
      else
        if(dist<=dmin[6])
          {dmin[6]=dist;
           j++;
          }
        else
          if(dist<=dmin[7])
            {dmin[7]=dist;
             j++;
            }
           else
             if(dist<=dmin[8])
               {dmin[8]=dist;
                j++;
               }
              else
                if(dist<=dmin[9])
                  {dmin[9]=dist;
                   j++;
                  }
                else
                  if(dist<=dmin[10])
                  {dmin[10]=dist;
                  j++;
                  }
                  else
```

```
                    j++;
      }   /* end of else */
    } /* end of for */
for(k=0; k<11;k++)
 {
   dave[k]+=dmin[k];
   if(dmin[k]<=start)
     num[k][0]+=1;
  else if((dmin[k]>start)&&(dmin[k]<=start+dr))
   num[k][1]+=1;
  else if((dmin[k]>start+dr)&&(dmin[k]<=start+2*dr))
   num[k][2]+=1;
  else if((dmin[k]>start+2*dr)&&(dmin[k]<=start+3*dr))
   num[k][3]+=1;
  else if((dmin[k]>start+3*dr)&&(dmin[k]<=start+4*dr))
   num[k][4]+=1;
  else if((dmin[k]>start+4*dr)&&(dmin[k]<=start+5*dr))
   num[k][5]+=1;
  else if((dmin[k]>start+5*dr)&&(dmin[k]<=start+6*dr))
   num[k][6]+=1;
  else if((dmin[k]>start+6*dr)&&(dmin[k]<=start+7*dr))
   num[k][7]+=1;
  else if((dmin[k]>start+7*dr)&&(dmin[k]<=start+8*dr))
   num[k][8]+=1;
  else if((dmin[k]>start+8*dr)&&(dmin[k]<=start+9*dr))
   num[k][9]+=1;
  else if((dmin[k]>start+9*dr)&&(dmin[k]<=start+10*dr))
   num[k][10]+=1;
  else if((dmin[k]>start+10*dr)&&(dmin[k]<=start+11*dr))
   num[k][11]+=1;
  else if((dmin[k]>start+11*dr)&&(dmin[k]<=start+12*dr))
   num[k][12]+=1;
  else if((dmin[k]>start+12*dr)&&(dmin[k]<=start+13*dr))
   num[k][13]+=1;
  else if((dmin[k]>start+13*dr)&&(dmin[k]<=start+14*dr))
   num[k][14]+=1;
  else if((dmin[k]>start+14*dr)&&(dmin[k]<=start+15*dr))
   num[k][15]+=1;
  else if((dmin[k]>start+15*dr)&&(dmin[k]<=start+16*dr))
```

```
    num[k][16]+=1;
   else if((dmin[k]>start+16*dr)&&(dmin[k]<=start+17*dr))
    num[k][17]+=1;
   else if((dmin[k]>start+17*dr)&&(dmin[k]<=start+18*dr))
    num[k][18]+=1;
   else if((dmin[k]>start+18*dr)&&(dmin[k]<=start+19*dr))
    num[k][19]+=1;
   else if((dmin[k]>start+19*dr)&&(dmin[k]<=start+20*dr))
    num[k][20]+=1;
   else if((dmin[k]>start+20*dr)&&(dmin[k]<=start+21*dr))
    num[k][21]+=1;
   else if((dmin[k]>start+21*dr)&&(dmin[k]<=start+22*dr))
    num[k][22]+=1;
   else if((dmin[k]>start+22*dr)&&(dmin[k]<=start+23*dr))
    num[k][23]+=1;
   else if((dmin[k]>start+23*dr)&&(dmin[k]<=start+24*dr))
    num[k][24]+=1;
   else if((dmin[k]>start+24*dr)&&(dmin[k]<=start+25*dr))
    num[k][25]+=1;
   else if((dmin[k]>start+25*dr)&&(dmin[k]<=start+26*dr))
    num[k][26]+=1;
   else if((dmin[k]>start+26*dr)&&(dmin[k]<=start+27*dr))
    num[k][27]+=1;
   else if ((dmin[k]>start+27*dr)&&(dmin[k]<=start+28*dr))
   num[k][28]+=1;
   else if((dmin[k]>start+28*dr)&&(dmin[k]<=start+29*dr))
   num[k][29]+=1;
   else if(dmin[k]>start+29*dr)
   num[k][30]+=1;
  }
 i++;
}  /* end of loop for near neighbor distribution */

  for(k=0; k<11; k++)
  {
    dave[k]=dave[k]/totalnumber;
    fprintf(outdata1,"%dth order,%f\n",k,dave[k]);
  }
```

```
 fprintf(outdata1,
"************************************************\n");
 fprintf(outdata1, "                nearest neighbor function \n");
 fprintf(outdata1,
"************************************************\n\n");
 fprintf(outdata1, "distance num(0) num(1) num(2) numb(3) num(4)
num(5)\n");

  for(i=0; i<31; i++)
      {
     fprintf(outdata1, "%5.2f%7d%7d%7d%7d%7d%7d%7d%7d%7d%7d%7d\n",
start+i*dr,
num[0][i], num[1][i], num[2][i], num[3][i], num[4][i],
num[5][i],num[6][i],num[7][i],num[8][i],num[9][i],num[10][i]);

      }

  fclose(outdata1);
/* end of calculation of nearest neighbor distribution funciton */
}
```

B.2 Code for generation of 3D nearest neighbor distribution from data on centroid

```
#include <stdio.h>
#include<c:\My Documents\MS C++\3dnnd\asim.h>
#include <math.h>
#include <algorithm>
using namespace std ;

#define dist(x1,y1,z1,x2,y2,z2) sqrt((x1-x2)*(x1-x2)+(y1-y2)*(y1-
y2)+(z1-z2)*(z1-z2))

FILE *fin, *fout;
char dir_nm[250], file_nm[250],name[250];

class particle_cla
{
public:
      float x;
```

```
      float y; // centroid coordinates
      float z;
      float d; //size
};

void main( void )
{
   particle_cla *particle;
   float x1,y1,z1,x2,y2,z2,d,*distance;
   long total_part, i, j;
   char s[81];
   char c;

   printf("\n\n\n\t directory : ");
   scanf("%s",&dir_nm);
   printf("\n\t file : ");
   scanf("%s",&file_nm);
   sprintf(name,"%s\\%s.txt",dir_nm,file_nm);

   //fin = fopen( "c:\\nnd\\xyzs.txt", "r" );
   fin = fopen( name, "r" );
   fseek( fin, 0L, SEEK_SET );

      /* Count number of lines in the input file */
   i=0;
   while (feof(fin)==0)
   {
      fscanf( fin, "%f%f%f%f", &x1,&y1,&z1,&d );
        i++;
   }
   total_part=i;

   particle = new particle_cla[total_part];
   matrix nnd(total_part,10);
   distance = new float[total_part];


      /* Read data from the file in to the array */
    fseek( fin, 0L, SEEK_SET );
```

```
      i=0;
      while (feof(fin)==0)
      {
            fscanf( fin, "%f%f%f%f",
&particle[i].x,&particle[i].y,&particle[i].z,&particle[i].d );
            i++;
      }
    fclose(fin);

      printf( "%f %f %f %f \n", x1,y1,z1,d );


     sprintf(name,"%s\\%s.nnd",dir_nm,file_nm);
      fout = fopen( name, "w" );
      //distance calculation
    for (i=0;i<total_part;i++)
      {
            x1=particle[i].x;
            y1=particle[i].y;
            z1=particle[i].z;

            for (j=0;j<total_part;j++)
            {
                  x2=particle[j].x;
                  y2=particle[j].y;
                  z2=particle[j].z;
                  distance[j]=dist(x1,y1,z1,x2,y2,z2);
            }
     partial_sort(distance, distance+10, distance+total_part-1) ;
      for (int k=1;k<10;k++)
            fprintf(fout,"%f ",*(distance+k));
      fprintf(fout,"\n");

      }

      fclose(fout);
      delete particle;
      printf("\nTotal number of particles are %ld\n\n", total_part);
```

```
}
#########################################################################
class matrix{
      float** p;
      int s1, s2;
  public:
      matrix(int d1,int d2);
      ~matrix();
      float& operator()(int i,int j);
};

matrix::matrix(int d1,int d2)
{
      s1=d1;s2=d2;
      p = new float*[s1];
      for (int i=0;i<s1;++i)
            p[i] = new float[s2];
}

matrix::~matrix()
{
      for (int i=0;i<s1;++i)
            delete p[i];
      delete p;
}

float& matrix::operator()(int i, int j)
{
      return p[i][j];
}
#########################################################################
```

B.3 Code for generation of 2D radial distribution function from data on centroid

```
#include  <stdio.h>
#include  <stdlib.h>
#include  <time.h>
#include  <float.h>
#include  <math.h>
```

```
#define   Total 10000
#define   Nhis 40              /* number of points in histrogram*/

#define   Rstart 0.0           /* Start value of r */
#define   Rmin 0.0             /* Minimum radius which is to be ignored*/

#define   Pi 4*atan(1)

FILE  *fp,*FK,*FG,*K[3][3],*G[3][3];
char  name[10],nameo[15], mode[3],buffer[100];
double      out, Bx1,Bx2,By1,By2,ImSizex,ImSizey;
int         nx,ny;
double      Xmin,Xmax,Ymin,Ymax,PixSize,mag;
double      Xcg,Ycg,R1,R2;
double      Data[Total][3];
double      pcount[Nhis][2],kfun[Nhis],gfun[Nhis-1];
double
kall[Nhis][3][3],pcountall[3][3][Nhis],pc1[3][3][Nhis],gall[Nhis-
1][3][3],Nsize[3][3];
double      Number,f0,f1,f2,Gr,Den;
int         i,j,ibase,ih,ib;
long        Nmax,Np,Ns,Nm,Nl,Nn[3];
double      Area,Na,Af,Ang;
double      Rmean,dR,StanD,Rlow,Rhigh,norm,Rall[3];



double Num(double Xcg ,double Ycg,double R1,double R2,double ang, int
base, double nsize[3][3])

        {
      int i,ibb,ihh;
      double n,dis,x,y;
      n=0;
for (ibb=0;ibb<=2;ibb++)
for (ihh=0;ihh<=2;ihh++)
      nsize[ibb][ihh]=0;

      for ( i=0; i<Nmax-1 ; i++)
```

```
            {
            x=Data[i][0];
            y=Data[i][1];
            if ( (x>=Xcg-R2) && (x<=Xcg+R2) && (y>=Ycg-R2) &&
(y<=Ycg+R2) )
      {
            dis = sqrt( pow((Xcg - x),2.0) + pow((Ycg-y),2.0) );

            if ( (dis > R1) && ( dis <= R2) )
            {
                  n++;

                  if ( Data[i][2] <= Rlow ) nsize[base][0]++;

                  if ( (Data[i][2] > Rlow) && (Data[i][2] <= Rhigh) )
nsize[base][1]++;

                  if ( Data[i][2] > Rhigh )     nsize[base][2]++;

           }


      };
            };

      n=2*Pi*n/ang;
      nsize[base][0] = 2*Pi*nsize[base][0]/ang;
      nsize[base][1] = 2*Pi*nsize[base][1]/ang;
      nsize[base][2] = 2*Pi*nsize[base][2]/ang;


      return n;

      }
```

```
double Dev(double Rm, double XY, double XYext)
      {
      return Rm*Rm - (XY-XYext)*(XY-XYext);
      }


double Angle(double Xcg ,double Ycg,double R1,double R2)
      {
      double Rm;
                        double inter[2][2];
      double Temp1,Temp2;
                        double Q,Per,Base,ang;
      double x1,x2,y1,y2;
      int i;

      i = 0;
      Rm = (R1+R2)/2;    /** Mean value of R */

      if ( (Q = Dev(Rm,Xcg,Xmin)) >0 )
      {
      Temp1 = -sqrt(Q) + Ycg;
      Temp2 = sqrt(Q) + Ycg;

      if ( ( Temp1 <= Ymax )  && ( Temp1 >= Ymin ) )
      {
      inter[i][0] = Xmin;
      inter[i][1] = Temp1;
      i++;
      }

      if ( ( Temp2 <= Ymax ) &&  ( Temp2 >= Ymin ) )
      {
      inter[i][0] = Xmin;
      inter[i][1] = Temp2;
      i++;
      }
      }

      if ( (Q = Dev(Rm,Xcg,Xmax)) >0 )
```

```
{
Temp1 = -sqrt(Q) + Ycg;
Temp2 = sqrt(Q) + Ycg;

if ( ( Temp1 <= Ymax ) &&  ( Temp1 >= Ymin ) )
{
inter[i][0] = Xmax;
inter[i][1] = Temp1;
i++;
}

if ( ( Temp2 <= Ymax ) &&  ( Temp2 >= Ymin ) )
{
inter[i][0] = Xmax;
inter[i][1] = Temp2;
i++;
}
}



if ( (Q = Dev(Rm,Ycg,Ymax)) >0 )
{
Temp1 = -sqrt(Q) + Xcg;
Temp2 = sqrt(Q) + Xcg;

if ( ( Temp1 <= Xmax ) &&  ( Temp1 >= Xmin ) )
{
inter[i][0] = Temp1;
inter[i][1] = Ymax;
i++;
}

if ( ( Temp2 <= Xmax ) &&  ( Temp2 >= Xmin ) )
{
inter[i][0] = Temp2;
inter[i][1] = Ymax;
i++;
}
```

```
        }


        if ( (Q = Dev(Rm,Ycg,Ymin)) >0 )
        {
        Temp1 = -sqrt(Q) + Xcg;
        Temp2 = sqrt(Q) + Xcg;

        if ( ( Temp1 <= Xmax ) &&  ( Temp1 >= Xmin ) )
        {
        inter[i][0] = Temp1;
        inter[i][1] = Ymin;
        i++;
        }

        if ( ( Temp2 <= Xmax ) &&  ( Temp2 >= Xmin ) )
        {
        inter[i][0] = Temp2;

        inter[i][1] = Ymin;
        i++;
        }
        }


if ( i>0)
        {

        x1=inter[0][0];

        x2=inter[1][0];

        y1=inter[0][1];

        y2=inter[1][1];

        Per = ( sqrt ( pow((x1-x2),2.0) + pow((y1-y2) ,2.0) ))/2;

        Base = sqrt( pow( (Xcg - (x1+x2)/2 ),2.0 ) + pow( (Ycg - (y1+y2)/2
```

```
),2.0 ) );

/*    printf("x1=%f y1=%f x2=%f y2=%f",x1,y1,x2,y2);*/

      if (Base != 0.0 )
      ang = atan(Per/Base);
      else
      ang = 2*atan(1);

      if (x1==x2 | y1== y2) ang = 3.1416 - ang;
      return 2 * ang;

      }

      else
      return 8*atan(1);

      }
```

```
/*****************************  M A I N
*******************************/


void main(void)

{
ImSizex = 536;
ImSizey = 400;
Bx1 = 52;
Bx2 = 536/4;
By1 = 40;
By2 = 400/4;
```

```
printf("\n\n\t\tTHIS PROGRAM WORKS WITHOUT THE NEED OF MAGNIFICATION
ETC..\n\n");
printf( "The input data file is : ");
scanf("%s",name);

sprintf(nameo,"%s.cor",name);
fp = fopen(nameo,"r");

fscanf(fp,"%d",&nx);
//printf( "\nNumber of images in the X direction are : %d\n",nx);

fscanf(fp,"%d",&ny);
//printf( "Number of images in the Y direction are : %d\n\n",ny);

fscanf(fp,"%lf",&mag);
//printf( "The magnification is : %lf\n\n",mag);

fscanf(fp,"%lf",&Rmean);
printf( "The mean radius is : %f\n\n",Rmean);

fscanf(fp,"%lf",&StanD);
printf( "The Standard Deviation is : %f\n\n",StanD);


dR = Rmean/5.0;

Rlow = Rmean - StanD/2;
Rhigh = Rmean + StanD/2;


PixSize = 162.5/mag;

Xmin = (Bx1+Bx2)*PixSize;
Ymin = (By1+By2)*PixSize;

Xmax = (Bx1 + nx*ImSizex - Bx2)*PixSize;
Ymax = (By1 + ny*ImSizey - By2)*PixSize;

Xmax=Ymax=0;
```

```
Xmin=Ymin=1000000;


i = 0;
Af=0;

/*vvvvvvvvvvvvvvvvvvvv  DATA INPUT  vvvvvvvvvvvvvvvvvvvv*/

while ( feof(fp) == 0  )
{
      fscanf(fp,"%i%lf%lf%lf",&j,&Data[i][0],&Data[i][1],&Data[i][2]);
      fgets(buffer,99,fp);
//    printf("X = %4.2f Y = %4.2f R =
%4.2f\n",Data[i][0],Data[i][1],Data[i][2]);
if (Data[i][2] !=0)
{
      if (Data[i][0]<Xmin) Xmin=Data[i][0];
      if (Data[i][0]>Xmax) Xmax=Data[i][0];
      if (Data[i][1]<Ymin) Ymin=Data[i][1];
      if (Data[i][1]>Ymax) Ymax=Data[i][1];
}


      if (Data[i][2] >Rmin*2 )
      {
      Af=Af+Pi*Data[i][2]*Data[i][2]/4.0;
      i++;
      }
}


/*^^^^^^^^^^^^^^^^^^^ DATA INPUT COMPLETE ^^^^^^^^^^^^^^^*/


Nmax = i-1;
Area = (Xmax-Xmin)*(Ymax-Ymin);
Af=Af/Area;
Na=Nmax/Area;
printf("Xmin = %4.1f Ymin = %4.1f Xmax = %4.1f Ymax =
```

```
%4.1f\n",Xmin,Ymin,Xmax,Ymax);
printf("\n\n The Na is %lf and area is %lf\n Area fractionis
%lf",Na,Area,Af);
scanf("%c%c",&buffer[0],&buffer[1]);
Rall[0]=0.0;
Rall[1]=0.0;
Rall[2]=0.0;



/*vvvvvvvvvvvvvvvv PARTICLE COUNTING vvvvvvvvvvvvvvvvvv*/

for (i=0; i < Nmax; i++)
{
      printf("%i\n",i);

      Xcg = Data[i][0];
      Ycg = Data[i][1];

      if ( Data[i][2] <= Rlow )
      {
            ibase=0;
            Ns++;
      }
      if ( (Data[i][2] > Rlow) && (Data[i][2] <= Rhigh) )
      {
            ibase=1;
            Nm++;
      }
      if ( Data[i][2] > Rhigh )
      {
            ibase=2;
            Nl++;
      }

      Nsize[ibase][0]=0.0;
      Nsize[ibase][1]=0.0;
      Nsize[ibase][2]=0.0;
```

```
      Rall[ibase]= Rall[ibase]+Data[i][2];

      for (j=0; j<Nhis; j++)
      {
      Np =0;
      for (ih=0;ih<=2;ih++)
      for (ib=0;ib<=2;ib++)
{
      pc1[ib][ih][j]=0;
      Nsize[ib][ih]=0;
}

            R1 = Rstart + j*dR;
            R2 = R1 + dR;

            Ang= Angle(Xcg,Ycg,R1,R2);
if (Ang == 8*atan(1) )
{
            Np = Num(Xcg,Ycg,R1,R2,Ang,ibase,Nsize);

            pcount[j][0] = pcount[j][0] + Np;

      pcount[j][1]++;
      pcountall[ibase][0][j]=pcountall[ibase][0][j]+Nsize[ibase][0];
      if (Nsize[ibase][0]>0) pc1[ibase][0][j]++;
      pcountall[ibase][1][j]=pcountall[ibase][1][j]+Nsize[ibase][1];
      if (Nsize[ibase][1]>0) pc1[ibase][1][j]++;
      pcountall[ibase][2][j]=pcountall[ibase][2][j]+Nsize[ibase][2];
      if (Nsize[ibase][2]>0) pc1[ibase][2][j]++;
}
      }
}

/*^^^^^^^^^^^^^^^^^^^^^^PARTICLE COUNTING COMPLETED^^^^^^^^^^^^^^^*/

Nn[0]=Ns;
Nn[1]=Nm;
Nn[2]=Nl;
```

```
kfun[0]=0;
for (ib=0;ib<=2;ib++)
for (ih=0;ih<=2;ih++)
      kall[0][ib][ih]=0;

R2=0;

for ( i=0 ; i<Nhis;i++)
{
      Number=pcount[i][0]/pcount[i][1];

      if (i>0)
      {
            kfun[i]=kfun[i-1];
            for (ib=0;ib<=2;ib++)
            for (ih=0;ih<=2;ih++)
            kall[i][ib][ih]=kall[i-1][ib][ih];
      }

      kfun[i] = kfun[i] + Number;
      for (ib=0;ib<=2;ib++)
      for (ih=0;ih<=2;ih++)

kall[i][ib][ih]=kall[i][ib][ih]+pcountall[ib][ih][i]/pc1[ib][ih][i];

printf("%d AFDShdsgfdhgggggggggggggggggggggggggggggggg %d\n",
kall[i][ib][ih],pcountall[ib][ih][i]);

}



gfun[0]=0;
for (ib=0;ib<=2;ib++)
for (ih=0;ih<=2;ih++)
gall[0][ib][ih]=0;

for ( i=1 ;i<Nhis-1; i++)
```

```
{
      R1=Rstart + (i+1)*dR;
      norm=2*dR*2*Pi*R1;
      gfun[i] = ( (kfun[i+1]-kfun[i-1])*Area)/(norm*Nmax);

      for (ib=0;ib<=2;ib++)
      for (ih=0;ih<=2;ih++)
      gall[i][ib][ih]= ( (kall[i+1][ib][ih]-kall[i-
1][ib][ih])*Area)/(norm*Nn[ih]);
}




sprintf(mode,"sml");
/*
for (ib=0;ib<=2;ib++)
for (ih=0;ih<=2;ih++)
            {
            sprintf(nameo,"%sK%c_%c.dat",name,mode[ib],mode[ih]);
            K[ib][ih] = fopen(nameo,"w");
            sprintf(nameo,"%sG%c_%c.dat",name,mode[ib],mode[ih]);
            G[ib][ih] = fopen(nameo,"w");
            }
*/

sprintf(nameo,"%sKto.dat",name);
FK = fopen(nameo,"w");

sprintf(nameo,"%sGto.dat",name);
FG = fopen(nameo,"w");




for ( i=0 ; i<Nhis;i++)
{
Number=pcount[i][0]/Nmax;
```

```
R1=Rstart + (i+1)*dR;
printf("Radius = %3.4f  Number = %4.2f  Cumulative =
%4.2f\n",R1,Number,kfun[i]);


fprintf(FK,"%3.4f  %3.4f  %3.4f\n",R1,kfun[i],R1/Rmean);
/*
   for (ib=0;ib<=2;ib++)
   for (ih=0;ih<=2;ih++)
   fprintf(K[ib][ih],"%3.4f  %3.4f  %3.4f
%3.4f\n",R1,kall[i][ib][ih],R1/Rmean,R1/(
(Rall[ib]+Rall[ih])/(Nn[ib]+Nn[ih]) ));
*/

if (i<(Nhis-1))
{
 fprintf(FG,"%3.4f  %3.4f   %3.4f\n",R1,gfun[i],R1/Rmean);
/*
   for (ib=0;ib<=2;ib++)
   for (ih=0;ih<=2;ih++)
   fprintf(G[ib][ih],"%3.4f  %3.4f  %3.4f
%3.4f\n",R1,gall[i][ib][ih],R1/Rmean,R1/(
(Rall[ib]+Rall[ih])/(Nn[ib]+Nn[ih]) ));
*/
}


}


/*
for (ib=0;ib<=2;ib++)
for (ih=0;ih<=2;ih++)
{
fclose(K[ib][ih]);
fclose(G[ib][ih]);
}
*/
fclose(FK);
```

```
fclose(FG);
printf(" \n\n  Area fraction = %1.4f \n  Number of points per unit area
Na = %3.4e \n",Af,Na*1E+12);
printf("Ns = %5d Nm = %5d Nl = %5d  Ntotal = %5d
\n",Nn[0],Nn[1],Nn[2],Nmax);
}
```

B.4 Code for transformation of 2D particle size to 3D particle size by Saltykov's technique (written MS Visual Basic)

```
'D2_to_D3 Macro
Sub D2_to_D3()
    Range("A3:A9000").Select
    Application.CutCopyMode = False
    Selection.Copy
    Range("B3").Select
    ActiveSheet.Paste
    Application.CutCopyMode = False
    Selection.Sort Key1:=Range("B3"), Order1:=xlDescending, Header:= _
      xlGuess, OrderCustom:=1, MatchCase:=False, Orientation:= _
      xlTopToBottom
    ActiveWindow.SmallScroll Down:=-2
    Range("E3").Select
    ActiveCell.FormulaR1C1 = "=RC[-3]/R[-1]C"
    Range("G4").Select
    ActiveCell.FormulaR1C1 = "=R[-1]C[-2]"
    Range("G5").Select
    ActiveCell.FormulaR1C1 = "=R[-1]C+R3C[-2]"
    Range("G5").Select
    Selection.AutoFill Destination:=Range("G5:G11"), Type:=xlFillDefault
    Range("G5:G11").Select
    Selection.AutoFill Destination:=Range("G5:G18"), Type:=xlFillDefault
    Range("G5:G18").Select
    Range("B3:B9000").Select
```

```
Range("E3").Select
Selection.Copy
Selection.PasteSpecial Paste:=xlValues, Operation:=xlNone, _
    SkipBlanks:=False, Transpose:=False
Range("B3:B9000").Select
Application.CutCopyMode = False
Selection.ClearContents
Range("A3").Select
Application.ExecuteExcel4Macro String:= _
    "HISTOGRAM('[2_TO_3.XLS]Sheet1'!R3C1:R9000C1, '[2_TO_3.XLS]Sheet1'!R4C9,
'[2_TO_3.XLS]Sheet1'!R4C7:R18C7, FALSE, FALSE, FALSE, FALSE)"
ActiveWindow.SmallScroll ToRight:=3
ActiveCell.Offset(1, 1).Range("A1:A15").Select
Selection.Copy
Sheets("Sheet2").Select
ActiveWindow.SmallScroll ToRight:=-10
ActiveCell.Offset(-2, -15).Range("A1").Select
Selection.PasteSpecial Paste:=xlAll, Operation:=xlNone, SkipBlanks _
    :=False, Transpose:=True
ActiveWindow.SmallScroll ToRight:=10
ActiveCell.Offset(2, 15).Range("A1:A15").Select
Application.CutCopyMode = False
Selection.Copy
Sheets("Sheet1").Select
ActiveCell.Offset(0, 1).Range("A1").Select
Selection.PasteSpecial Paste:=xlValues, Operation:=xlNone, _
    SkipBlanks:=False, Transpose:=False
ActiveWindow.SmallScroll Down:=4
ActiveCell.Offset(15, 0).Range("A1").Select
Application.CutCopyMode = False
ActiveCell.FormulaR1C1 = "=SUM(R[-15]C:R[-1]C)"
ActiveCell.Select
Selection.Copy
```

```
ActiveCell.Offset(0, -1).Range("A1").Select
ActiveSheet.Paste
ActiveWindow.SmallScroll Down:=-6
ActiveWindow.SmallScroll ToRight:=-4
ActiveCell.Offset(-18, -7).Range("A1").Select
Application.CutCopyMode = False
ActiveCell.FormulaR1C1 = "2D"
ActiveCell.Offset(1, 0).Range("A1").Select
ActiveCell.FormulaR1C1 = "Bin"
ActiveCell.Offset(0, 1).Range("A1").Select
ActiveCell.FormulaR1C1 = "Range"
ActiveCell.Offset(0, 1).Range("A1").Select
ActiveCell.FormulaR1C1 = "Mean Bin"
ActiveCell.Offset(0, 1).Range("A1").Select
ActiveCell.FormulaR1C1 = "Frequency"
ActiveCell.Offset(-1, 3).Range("A1").Select
ActiveCell.FormulaR1C1 = "3D"
ActiveCell.Offset(1, 0).Range("A1").Select
ActiveCell.FormulaR1C1 = "Size"
ActiveCell.Offset(0, 1).Range("A1").Select
ActiveCell.FormulaR1C1 = "Frequency"
ActiveCell.Offset(2, 3).Range("A1").Select
ActiveCell.FormulaR1C1 = "=RC[-3]/J*20"
ActiveCell.Select
ActiveCell.FormulaR1C1 = "=RC[-3]/R20C[-3]"
ActiveCell.Select
Selection.AutoFill Destination:=ActiveCell.Range("A1:A15"), Type:= _
  xlFillDefault
ActiveCell.Range("A1:A15").Select
ActiveCell.Range("A1:A15").Select
Selection.Copy
ActiveCell.Offset(0, 1).Range("A1").Select
ActiveSheet.Paste
```

```
ActiveCell.Offset(-1, -11).Range("A1").Select
Application.CutCopyMode = False
ActiveCell.FormulaR1C1 = "0"
ActiveCell.Offset(1, 6).Range("A1:A15").Select
Selection.Copy
ActiveCell.Offset(-1, -5).Range("A1").Select
Selection.PasteSpecial Paste:=xlValues, Operation:=xlNone, _
    SkipBlanks:=False, Transpose:=False
ActiveCell.Offset(1, -1).Range("A1").Select
Application.CutCopyMode = False
ActiveCell.FormulaR1C1 = "=R[-1]C[1]"
ActiveCell.Select
Selection.AutoFill Destination:=ActiveCell.Range("A1:A14"), Type:= _
    xlFillDefault
ActiveCell.Range("A1:A14").Select
ActiveCell.Offset(-1, 2).Range("A1").Select
ActiveCell.FormulaR1C1 = "=(RC[-1]+RC[-2])/2"
ActiveCell.Select
Selection.AutoFill Destination:=ActiveCell.Range("A1:A15"), Type:= _
    xlFillDefault
ActiveCell.Range("A1:A15").Select
ActiveCell.Offset(0, 1).Range("A1").Select
ActiveWindow.SmallScroll ToRight:=5
ActiveCell.Offset(1, 7).Range("A1:A15").Select
Selection.Copy
ActiveCell.Offset(-1, -7).Range("A1").Select
Selection.PasteSpecial Paste:=xlValues, Operation:=xlNone, _
    SkipBlanks:=False, Transpose:=False
ActiveCell.Offset(0, 1).Range("A1").Select
Application.CutCopyMode = False
ActiveCell.FormulaR1C1 = "=RC[-1]*RC[-2]"
ActiveCell.Select
Selection.AutoFill Destination:=ActiveCell.Range("A1:A15"), Type:= _
```

```
    xlFillDefault
ActiveCell.Range("A1:A15").Select
ActiveCell.Offset(15, 0).Range("A1").Select
ActiveCell.FormulaR1C1 = "=SUM(R[-15]C:R[-1]C)"
ActiveCell.Select
Selection.Font.Bold = True
ActiveCell.Offset(-14, 2).Range("A1:A15").Select
Selection.Copy
ActiveWindow.SmallScroll ToRight:=3
ActiveCell.Offset(0, 4).Range("A1").Select
Selection.PasteSpecial Paste:=xlValues, Operation:=xlNone, _
    SkipBlanks:=False, Transpose:=False
ActiveCell.Offset(0, 1).Range("A1:A15").Select
Application.CutCopyMode = False
Selection.Copy
Selection.PasteSpecial Paste:=xlValues, Operation:=xlNone, _
    SkipBlanks:=False, Transpose:=False
ActiveCell.Offset(-1, -5).Range("A1:C19").Select
Application.CutCopyMode = False
Selection.Clear
ActiveCell.Offset(1, 4).Range("A1:B16").Select
ActiveWindow.SmallScroll Down:=-4
Selection.Cut Destination:=ActiveCell.Offset(-1, -4).Range("A1:B16")
ActiveCell.Offset(-1, -2).Range("A1").Select
ActiveCell.FormulaR1C1 = "=RC[-1]*RC[-2]"
ActiveCell.Select
Selection.AutoFill Destination:=ActiveCell.Range("A1:A15"), Type:= _
    xlFillDefault
ActiveCell.Range("A1:A15").Select
ActiveCell.Offset(15, 0).Range("A1").Select
ActiveCell.FormulaR1C1 = "=SUM(R[-15]C:R[-1]C)"
ActiveCell.Select
Selection.Font.Bold = True
```

```
    ActiveCell.Offset(-17, -8).Range("A1:I18").Select
    ActiveWindow.Zoom = True
    ActiveCell.Offset(17, 4).Range("A1").Select
End Sub
```

VITA

Asim Tewari was born in Jodhpur, India on September 12, 1974. He recieved his high school education from Mahesh Higher Secondary School in Jodhpur. Following his high school he joined Indian Institute of Technology, Kanpur where he received his Bachelor's degree in Materials Science & Metallurgical Engineering in May 1994. He joined the group of Professor Arun M. Gokhale as a graduate student at Georgia Institute of Technology in the fall of 1994. He received Masters degree from Georgia Institute of Technology in the fall of 1996, and continued his education at Georgia Institute of Technology to pursue a doctorate degree in Materials Science & Engineering under Professor Gokhale. His Doctorate research was on the effect of gravity on liquid phase sintering. This involved characterization of specimens liquid phase sintered in microgravity environment of space shuttle. On February 19th he defended his doctorate thesis.